

DISSERTATION

ACCELERATED ADAPTIVE NUMERICAL METHODS FOR COMPUTATIONAL  
ELECTROMAGNETICS: ENHANCING GOAL-ORIENTED APPROACHES TO ERROR  
ESTIMATION, REFINEMENT, AND UNCERTAINTY QUANTIFICATION

Submitted by

Jake J. Harmon

Department of Electrical and Computer Engineering

In partial fulfillment of the requirements

For the Degree of Doctor of Philosophy

Colorado State University

Fort Collins, Colorado

Summer 2022

Doctoral Committee:

Advisor: Branislav M. Notaroš

Don Estep

Milan Ilić

Iuliana Oprea

Copyright by Jake J. Harmon 2022

All Rights Reserved

## ABSTRACT

### ACCELERATED ADAPTIVE NUMERICAL METHODS FOR COMPUTATIONAL ELECTROMAGNETICS: ENHANCING GOAL-ORIENTED APPROACHES TO ERROR ESTIMATION, REFINEMENT, AND UNCERTAINTY QUANTIFICATION

This dissertation develops strategies to enhance adaptive numerical methods for partial differential equation (PDE) and integral equation (IE) problems in computational electromagnetics (CEM). Through a goal-oriented emphasis, with a particular focus on scattered field and radar cross-section (RCS) quantities of interest (QoIs), we study automated acceleration techniques for the analysis of scattering targets. A primary contribution of this work, we propose an error prediction refinement strategy, which, in addition to providing rigorous global error estimates (as opposed to just error indicators), promotes equilibration of local error contribution estimates, a key requirement of efficient discretizations. Furthermore, we pursue consistent exponential convergence of the QoIs with respect to the number of degrees of freedom without prior knowledge of the solution behavior (whether smooth or otherwise) or the sensitivity of the QoIs to the discretization quality. These developments, in addition to supporting significant reductions in computation time for high accuracy, offer enhanced confidence in simulation results, promoting, therefore, higher quality decision making and design.

Moreover, aside from the need for rigorous error estimation and fully automated discretization error control, practical simulations necessitate a study of uncertain effects arising, for example, from manufacturing tolerances. Therefore, by repeating the emphasis on the QoI, we leverage the computational efforts expended in error estimation and adaptive refinement to relate perturbations in the model to perturbations of the QoI in the context of applications in CEM. This combined approach permits simultaneous control of deterministic discretization error and its effect on the QoI as well as a study of the QoI behavior in a statistical sense.

A substantial implementation infrastructure undergirds the developments pursued in this dissertation. In particular, we develop an approach to conducting flexible refinements capable of tuning both local spatial resolution ( $h$ -refinements) and enriching function spaces ( $p$ -refinements) for vector finite elements. Based on a superposition of refinements (as opposed to traditional refinement-by-replacement), the presented  $hp$ -refinement paradigm drastically reduces implementation overhead, permits straightforward representation of meshes of arbitrary irregularity, and retains the potential for theoretically optimal rates of convergence even in the presence of singularities. These developments amplify the utility of high-quality error estimation and adaptive refinement mechanisms by facilitating the insertion of new degrees of freedom with surgical precision in CEM applications.

We apply the proposed methodologies to a strong set of canonical targets and benchmarks in electromagnetic scattering and the Maxwell eigenvalue problem. While directed at time-harmonic excitations, the proposed methods readily apply to other problems and applications in applied mathematics.

## ACKNOWLEDGEMENTS

I wish to acknowledge my advisor, Prof. Branislav M. Notaroš, for his support and guidance, for providing me the opportunities to pursue independent research, and helping to make my Ph.D. a success. I am grateful for the mentorship and guidance my committee members, Prof. Don Estep, Prof. Milan Ilić, and Prof. Iuliana Oprea, provided me during my graduate studies. I also wish to acknowledge the financial support of the DoD High Performance Computing and Modernization Program and the US Air Force Research Laboratory. Specifically, I thank Dr. Daniel Dault and Dr. Michael Gilbert, Program Directors, US AFRL, RAVeNS Program, for their support and guidance on the project and valuable discussions.

Further, I wish to thank Prof. Don Estep again and Prof. Troy Butler for their collaboration during my Ph.D. and the advice I will carry with me through the next stages in my career. I also thank Prof. Wolfgang Bangerth for his advice and help.

Additionally, I thank all those I had the privilege to work with during my Ph.D. It is impossible for me to mention everyone that deserves my thanks here; however, I especially thank Jeremiah Corrado for our extensive collaborations during my mentorship of his master's project and who became a great friend.

Lastly, I would like to thank my parents, Donna and Thomas Harmon, for their steadfast support.

## TABLE OF CONTENTS

ABSTRACT . . . . .	ii
ACKNOWLEDGEMENTS . . . . .	iv
LIST OF TABLES . . . . .	vii
LIST OF FIGURES . . . . .	viii
Chapter 1 Introduction . . . . .	1
Chapter 2 Accelerated Adaptive Error Control and Refinement for SIE Scattering Problems	6
2.1 Introduction . . . . .	6
2.2 The Adjoint EFIE and EFIE-MFIE (PMCHWT) Problems . . . . .	8
2.2.1 Problem Formulations . . . . .	8
2.2.2 Computing the Excitation for the Adjoint Problem . . . . .	13
2.3 Error Estimation and Adaption . . . . .	15
2.4 Numerical Results . . . . .	22
2.5 Conclusion . . . . .	39
Chapter 3 Adaptive $hp$ -Refinement for 2-D Maxwell Eigenvalue Problems: Method and Benchmarks . . . . .	40
3.1 Introduction . . . . .	40
3.2 Error Estimation and Refinement Classification . . . . .	43
3.2.1 Problem Formulation . . . . .	43
3.2.2 Error Estimation . . . . .	44
3.2.3 Refinement Classification . . . . .	47
3.3 Numerical Results . . . . .	52
3.4 Conclusion . . . . .	66
Chapter 4 Adjoint Sensitivity Analysis for Uncertain Material Parameters in Frequency Domain 3-D FEM . . . . .	68
4.1 Introduction . . . . .	68
4.2 The Adjoint: Derivations and Estimators . . . . .	71
4.2.1 The Adjoint Problem . . . . .	71
4.2.2 Handling Parameter Uncertainty with HOPS . . . . .	73
4.3 Numerical Results . . . . .	77
4.4 Conclusion . . . . .	89
Chapter 5 A Refinement-by-Superposition $hp$ -Method for $H(\text{curl})$ - and $H(\text{div})$ -Conforming Discretizations . . . . .	93
5.1 Introduction . . . . .	93
5.2 Refinement-by-Superposition: Description and Construction . . . . .	95
5.2.1 Enforcing Continuity Requirements . . . . .	96
5.2.2 Eliminating Linear Dependence of the Hierarchical Refinements . . . . .	97
5.2.3 Summary of the Overall Approach . . . . .	98
5.3 Numerical Results . . . . .	99
5.4 Conclusion . . . . .	104
Conclusion . . . . .	105
References . . . . .	109

Appendix A	Publications of the Candidate . . . . .	127
A.1	Journal Papers . . . . .	127
A.2	Peer-Reviewed Conference Papers and Abstracts . . . . .	128

## LIST OF TABLES

3.1	Benchmark Eigenvalues Computed With E-AMR. . . . .	66
4.1	Quantitative comparison of HOPS and Monte Carlo for the real and imaginary QoI probability densities in Fig. 4.2. . . . .	81
4.2	Quantitative comparison of HOPS and Monte Carlo for the real and imaginary QoI probability densities in Fig. 4.4. . . . .	83
4.3	Quantitative comparison of HOPS and Monte Carlo for the real and imaginary QoI probability densities in Fig. 4.7. . . . .	87

## LIST OF FIGURES

2.1	The starting discretization for the spherical scatterer $S1$ with 216 geometrically bicubic elements and first order basis functions. . . . .	23
2.2	Performance of the AMR algorithm for the spherical scatterer $S1$ for four tolerances. . . . .	25
2.3	Convergence of the actual and estimated relative errors for the monostatic RCS of the dielectric spherical scatterer $S1$ . . . . .	27
2.4	Illustration of the error contribution estimate distributions for the dielectric scatter $S1$ . . . . .	27
2.5	Illustration of the expansion orders for the coarsest and finest tolerances of the dielectric spherical scatterer $S1$ . . . . .	28
2.6	The distribution of expansion orders for the spherical scatterer $S1$ for the four tolerances. . . . .	29
2.7	The total cost (in terms of the number of DoFs) of solving both the forward and adjoint problems for the spherical scatterer $S1$ for the four tolerances. . . . .	29
2.8	The starting discretization for the NASA Almond scatterer $S2$ with 136 geometrically biquadratic elements and first order basis functions. . . . .	30
2.9	Performance of the AMR algorithm for the NASA almond scatterer $S2$ for four tolerances. . . . .	31
2.10	Convergence of the actual and estimated relative errors for the monostatic RCS of the dielectric NASA almond scatterer $S2$ . . . . .	32
2.11	Illustration of the expansion orders for the coarsest and finest tolerances of the dielectric NASA almond scatterer $S2$ . . . . .	32
2.12	The distribution of expansion orders for the NASA almond scatterer $S2$ for the four tolerances. . . . .	33
2.13	The total cost (in terms of the number of DoFs) of solving both the forward and adjoint problems for the NASA almond scatterer $S2$ for the four tolerances. . . . .	33
2.14	The starting discretization for the square plate scatterer of dimension $8\lambda \times 8\lambda$ with 100 geometrically bilinear elements. . . . .	34
2.15	The RCS (in dB) computed from the starting discretization and the adaptively refined discretizations compared to that of the uniformly refined reference for the square plate scatterer over a range of monostatic scattering angles. . . . .	35
2.16	Mean relative error contribution estimates (normalized according to the RCS at each scattering angle) with the dispersion illustrated by bands containing two-thirds of the data versus the scattering angle for the starting and final discretizations of the AMR procedure applied to the square plate scatterer. . . . .	35
2.17	The number of DoFs required by the AMR procedure compared to the uniformly refined reference for the square plate scatterer over a range of monostatic scattering angles. . . . .	36
2.18	The RCS (in dB) computed from the starting discretization and the adaptively refined discretizations compared to that of the uniformly refined reference for the dielectric NASA almond scatterer over a range of monostatic scattering angles. . . . .	37
2.19	Mean relative error contribution estimates (normalized according to the RCS at each scattering angle) with the dispersion illustrated by bands containing two-thirds of the data versus the scattering angle for the starting and final discretizations of the AMR procedure applied to the NASA almond scatterer. . . . .	38

2.20	The number of DoFs required by the AMR procedure compared to the uniformly refined reference for the NASA almond scatterer over a range of monostatic scattering angles. . . . .	38
3.1	The starting discretization for the L-shaped waveguide. . . . .	53
3.2	Field magnitudes for the singular eigenfunctions. (a) The 1st eigenfunction. . . . .	55
3.3	Field magnitudes for the non-smooth eigenfunctions. . . . .	56
3.4	Field magnitudes for the globally smooth eigenfunctions. (a) The 3rd eigenfunction. . . . .	57
3.5	Convergence of the eigenvalues of the singular eigenfunctions with respect to the number of degrees of freedom. . . . .	59
3.6	The first converged discretizations for the singular eigenpairs. . . . .	61
3.7	Convergence of the eigenvalues of the non-smooth eigenfunctions with respect to the number of degrees of freedom. . . . .	62
3.8	The first converged discretizations for the non-smooth eigenpairs. . . . .	63
3.9	Convergence of the eigenvalues of the smooth eigenfunctions with respect to the number of degrees of freedom. . . . .	64
4.1	Sampled real and imaginary monostatic scattering QoI responses for random variation in the imaginary component of the relative permittivity of the dielectric sphere. . . . .	79
4.2	Approximate real and imaginary monostatic scattering QoI probability densities due to random variation in the imaginary component of the relative permittivity of the dielectric sphere. . . . .	80
4.3	Sampled real and imaginary monostatic scattering QoI responses for random variation in the real component of the relative permittivity of the dielectric sphere. . . . .	82
4.4	Approximate real and imaginary QoI probability densities due to random variation in the real component of the relative permittivity. . . . .	84
4.5	Approximate real and imaginary monostatic scattering QoI responses due to simultaneous random variation in the real and imaginary components of the relative permittivity of the dielectric sphere for a HOPS simulation with ten reference points. . . . .	86
4.6	Illustration of the clustering of the HOPS points based on $k$ -means probabilistic tuning. . . . .	87
4.7	Approximate real and imaginary monostatic scattering QoI probability densities due to simultaneous random variation in the real and imaginary components of the relative permittivity of the dielectric sphere. . . . .	88
4.8	Approximate real and imaginary monostatic scattering QoI probability densities due to random variation in the relative permittivity of each element of the dielectric sphere. . . . .	90
5.1	The RBS $hp$ -refinement activation and deactivation procedure. . . . .	100
5.2	The model and problem under study. . . . .	101
5.3	Example discretizations for the RBS $hp$ -method and the selectively $h$ -refined comparison method with uniform $p$ . . . . .	102
5.4	Convergence of the first eigenvalue for the RBS $hp$ -method and the comparison approach with $h$ -refinement levels from $L = 0$ to $L = 8$ and increasing uniform expansion orders. . . . .	103

# Chapter 1

## Introduction

In the solution of practical problems in applied mathematics, a lack of analytical solutions necessitates numerical schemes to produce approximate solutions, which, though including discretization error, accurately model real behavior. For example, the finite element method (FEM) and the boundary element method (BEM)—also referred to by the method of moments (MoM) in computational electromagnetics literature—leverage a weak formulation of a given partial differential equation (PDE) or integral equation (IE) problem to yield accurate approximate solutions composed of a linear combination of trial functions with respect to a space of test functions. In this dissertation, we restrict our analysis to Galerkin-type methods, in which the trial and test functions belong to the same spaces. These simulations, while not *replications* of reality, should yield adequate data to inform decision making, whether in the analysis of existing structures or in the design of new ones.

However, rather than being arbitrary spaces, the physics of the problem dictate where we seek approximate solutions. In the case of computational electromagnetics, to ensure convergence of the discrete problem, this often requires seeking solutions in  $H(\text{curl})$  or  $H(\text{div})$ , as opposed to the more typical Sobolev space  $H^1$ . These changes drive substantial distinction both in theory and implementation.

To control the discretization error introduced by these schemes, adaptive refinement permits targeting insufficient regions. However, Galerkin projection is not interpolation; it is not necessarily sufficient to introduce new degrees of freedom (DoFs) precisely where the solution error is high as error *pollution* may dictate to a significant degree the approximation quality throughout the discretization. Secondly, we are often interested in functionals of the solution, as opposed to the solution itself. Rather than settle for the accuracy of the solution as a proxy for the accuracy of a computable (or collection of computables), we prefer to combat solution error only where it poses the most significant trouble for the quality of this quantity of interest (QoI). Furthermore, in practical problems, various terms may only be known inexactly. Before introducing deterministic

error from the approximate solution of a given problem, constituent parameters (boundary or initial conditions, material properties, etc.) introduce statistical uncertainty. For example, the position of a satellite at a point in time may be known only within some quantity of meters, or as studied in this dissertation, the material parameters of a scattering target may exhibit a degree of uncertainty due, perhaps, to variations from manufacturing. As a result, a neglect to study perturbations or quantify uncertainty can incur significant, unexpected failure. In other words, we should have an expectation for what will occur that includes our uncertainty in the model. Finally, the accuracy in either case must not be considered in isolation; rather, any procedure must drive a balance between the accuracy and the efficiency of the refinement directives (including the algorithms to compute such directives) and uncertainty quantification.

To address these challenges and objectives, this dissertation presents a collection of developments related to adaptive error control and uncertainty quantification, from adaptive algorithms and procedures targeting discretization error to approaches that enhance the refinement infrastructure itself, that exert high-fidelity control over the interactions between numerical methods and simulation objectives.

The rest of this thesis is organized as follows:

In Chapter 2, we investigate a comprehensive methodology to estimating error, conducting effective refinements via error prediction, and tailoring discretizations. This work was prepublished by the author in [1], which is based on the earlier work by the author in [2]. Specifically, we present an application of adjoint-based adaptive error control and refinement for scattering problems solved using the MoM in the Electric Field Integral Equation (EFIE) and the coupled EFIE and Magnetic Field Integral Equation (MFIE) formulations. We examine the Poggio-Miller-Chang-Harrington-Wu-Tsai (PMCHWT) formulation of the EFIE-MFIE. We first construct the adjoint problems of the EFIE and the EFIE-MFIE for estimating the error of radar cross-section (RCS) QoIs directly. We then introduce an effective adaptive refinement algorithm, based on an error prediction heuristic and *a posteriori* error estimation, which enables rapid and consistent convergence regardless of a chosen tolerance and the coarseness of the starting discretization. The approach, moreover, inherently

promotes equilibration of the QoI error contributions and produces, therefore, consistently balanced meshes. Numerical examples with canonical scattering targets and adaptive  $p$ -refinement confirm the strength of the proposed refinement method, demonstrating the ability to generate high quality discretizations, both in terms of accuracy and efficiency, without expert user-intervention.

Chapter 3 is driven by motivations to reinforce existing numerical benchmarks in CEM and generate new ones for current and future work in adaptive finite element research. We present an application of goal-oriented adaptive isotropic  $hp$ -refinement for the 2-D Maxwell eigenvalue problem. This work was prepublished by the author in [3]. The underlying error estimation procedure follows the approach in Chapter 2, with a focus on eigenvalue quantities of interest. We apply a simplified goal-oriented error expression for improving the accuracy of the eigenvalues, which, when combined with indicators derived from the solution, enables highly targeted discretization tuning. Furthermore, we introduce an  $hp$ -refinement/coarsening optimizer coupled with smoothness estimation for refinement classification and execution. These enhancements yield cost-effective resource allocations that reach extremely high accuracy rapidly even for eigenvalues of singular eigenfunctions. Finally, we provide numerical benchmarks more accurate than existing numerical reference values, along with new benchmarks for higher-order modes that will facilitate the comparison and development of new approaches to adaptivity and  $hp$  finite elements in computational electromagnetics (CEM). The benchmark eigenpairs tested include eigenvalues with globally smooth and nonsmooth or singular eigenfunctions, providing a comprehensive set of solution behavior that may be encountered in numerical simulations across applications in applied mathematics. Our implementation is based on the open-source finite element library deal.II [4].

In Chapter 4, we explore the quantification of irreducible uncertainty, namely the effect other uncertainties (aside from numerical error which we *can* exert control over, as discussed in Chapter 2 and 3) have on output functionals. This work was prepublished by the author in [5]. These uncertainties may arise from realistic boundary or initial conditions or random variation due to manufacturing tolerances (e.g., material properties, surface roughness, etc.). Specifically, we present an application of adjoint analysis for efficient sensitivity analysis and estimation of quantities of

interest in the presence of uncertain model parameters in 3-D finite element method scattering problems. By leveraging local sensitivities (gradients of the QoI with respect to the random parameters) computed rapidly via the adjoint solution, quantification of uncertainty in the scattering model may be performed with extremely high accuracy and vast efficiency improvements in comparison to classic gradient approximation techniques, which require an additional forward solve for each random parameter, and Monte Carlo methods. Replacing full model solves with a surrogate constructed from the adjoint sensitivities avoids the computational expense of propagating samples, translating a problem of statistical error to one of deterministic error (namely, the quality of the surrogate). The method is demonstrated for low- and high-dimensional parameter spaces for scattered electric field quantities of interest. The results indicate strong agreement with equivalent Monte Carlo simulations for quantity of interest responses and probability densities.

Given the reliance of the methods and algorithms presented in the preceding chapters of this thesis on high implementation complexity, Chapter 5 develops an alternative framework for supporting adaptive  $hp$ -refinements, both anisotropic and isotropic, with a relatively lightweight implementation overhead compared to existing approaches. Based on refinement-by-superposition (RBS), the proposed approach for supporting  $hp$ -refinements for problems in CEM retains the potential for exponential rates of convergence (the theoretical optimum) even in the presence of singular solutions. The work was republished by the author in [6]. Subsequent papers and developments were co-authored by the author of this work in [7–9]. In contrast to dominant approaches to  $hp$ -refinement for continuous Galerkin methods, which rely on constrained-nodes or refinement-by-replacement (RBR), the multi-level strategy presented drastically reduces the implementation complexity. Through the RBS methodology, enforcement of continuity occurs by construction, enabling arbitrary levels of refinement with ease and without the practical (but not theoretical) limitations of constrained-node refinement. We outline the construction of this RBS  $hp$ -method for refinement with  $H(\text{curl})$ - and  $H(\text{div})$ -conforming finite cells. Numerical simulations for the 2-D finite element method (FEM) solution of the Maxwell eigenvalue problem demonstrate

the effectiveness of RBS  $hp$ -refinement. An additional goal of this work, we aim to promote the use of mixed-order (low- and high-order) elements in practical CEM applications.

## Chapter 2

# Accelerated Adaptive Error Control and Refinement for SIE Scattering Problems

### 2.1 Introduction

In the analysis of dielectric and metallic structures, whether for the design and simulation of antennas, aircraft, and other objects, the surface integral equation (SIE) approach provides a highly effective tool. By introducing electric and magnetic surface currents over the boundaries of homogeneous structures and discretizing the SIE problem by the method of moments (MoM), the unknown current densities may be found [10–12]. However, the choice of the approximation (e.g., the resolution of the surface or the number of degrees of freedom to model the currents) presents significant challenge in conducting accurate *and* efficient simulations for practical applications.

Electromagnetic modeling through the finite element method (FEM) has seen a significant research investment in error estimation and adaptive refinement to reduce the need for expert users in generating quality discretizations. Early approaches estimated the error of the solution or some property of the solution as an error indicator for refinement, see, for example, [13–19]. Further approaches to adaptive FEM have explored goal-oriented error estimation and adaptive refinement [2, 20–27].

Goal-oriented adaptivity, as opposed to standard residual or other less computationally expensive smoothness estimators and indicators (e.g., gradient jump methods), permits a significant enhancement of the refinement process [28]. Rather than address the accuracy of the solution as a whole, resources are allocated (or deallocated) to enhance the accuracy and efficiency of computing a quantity of interest (QoI). The use of adjoint-based methods facilitates the enhancement of numerical simulations for a variety of applications including goal-oriented error estimation through the dual-weighted residual (DWR) by delivering error *estimates* as opposed to just error *indica-*

tors [28–30], though at the expense of solving an additional global problem. In addition to error estimation, in CEM, similar adjoint techniques have been applied to sensitivity analysis [31–34], and optimization [35, 36].

An efficient refinement procedure, while beneficial for FEM approaches, is of particular importance when applying the MoM for solving SIE problems. Each iteration, therefore, should refine (or coarsen) to the full extent of profitability, rather than some arbitrary fraction of the estimated discretization error as commonly performed. Moreover, in order to reduce the number of iterations required for highly accurate simulations (e.g., to reduce the number of matrix solves required), the adaptive procedure should dictate not only the *scope*, but also the *depth* of refinement, rather than fixed increments (or decrements) in resolution.

Aside from [37, 38], which focused specifically on geometrical-based refinement for scatterers with sharp edges, the limited existing literature on refinement (and error estimation in general) for SIE methods has largely focused on examining various residuals or some property of the solution as a surrogate for the quality of discretization, as in early approaches in FEM. For example, [39] proposed computing a residual through an overdetermined system for  $h$ -refinement in the EFIE problem. Similarly, a gradient jump error indicator and residual indicators obtained from an overdetermined system and from the boundary conditions on the tangential and normal electric fields were applied for the EFIE and  $p$ -refinement in [40]. Furthermore, a pair of discontinuity error indicators in the form of the jump of the charge and current at cell boundaries was introduced in [41] and applied in [42, 43] with comparison to a standard residual estimator for  $h$ -refinement in the EFIE problem. For the CFIE solved with the discontinuous Galerkin method, [44] applied a residual-based error estimator for non-conformal  $h$ -refinements when a cell exceeded an arbitrary threshold.

Notably, in [45], goal-oriented error estimation using similar duality arguments as in this paper was leveraged for the computation of multi-port impedance parameters in the EFIE problem. In this manuscript, however, we study the EFIE and the Poggio-Miller-Chang-Harrington-Wu-Tsai (PMCHWT) formulation ([46–48]) of the coupled EFIE-MFIE problem for accelerating the adaptive

mesh refinement procedure to accurately compute the radar cross-section (RCS) of scattering targets. Moreover, we demonstrate that, through proper error estimation and refinement categorization, the dependence of the accuracy on the number of iterations may be heavily reduced. In particular, we extend the approach originally proposed in [2] for 3-D FEM to accelerate the refinement procedure for the SIE problem and metallic and composite scatterers. In contrast to existing approaches in SIE adaptivity, our approach attains an user desired accuracy rapidly and with a near-independence of the tolerance and number of iterations. Furthermore, our approach results in significantly improved mesh efficiency and error contribution equilibration through intelligent automatic resource allocation driven by a combination of an *a priori* error behavior heuristic and *a posteriori* error estimation.

The rest of the paper is organized as follows. Section II outlines the adjoint problem of the PMCHWT formulation of the coupled EFIE-MFIE, starting with the EFIE, and introduces a customizable scattering QoI as well as an RCS QoI to drive the adaptivity procedure. Section III describes the DWR expression of the error, where the solution of the global adjoint problem in an enriched space coupled with a combined *a priori-a posteriori* heuristic permits accelerating the refinement procedure through error prediction. Section IV includes numerical examples, indicating the ability of the proposed refinement procedure to produce highly accurate discretizations rapidly. The examples illustrate the inherent acceleration of refinement provided by the approach. Finally, the results indicate that the method successfully improves mesh equilibration, indicating the efficiency of the resultant discretizations.

## 2.2 The Adjoint EFIE and EFIE-MFIE (PMCHWT) Problems

### 2.2.1 Problem Formulations

We first outline the general procedure for deriving the dual (or adjoint) problem for a given forward problem,

$$\mathcal{L}\mathbf{u} = \mathbf{f} \tag{2.1}$$

involving the forward solution  $\mathbf{u}$  and an excitation  $\mathbf{f}$ , which is described either by a differential or integral equation, with an associated variational formulation: Find  $\mathbf{u} \in B$  such that

$$a(\mathbf{u}, \phi) = \langle \mathbf{f}, \phi \rangle \quad \forall \phi \in B, \quad (2.2)$$

where  $B$  denotes the trial and test space,  $\langle \cdot, \cdot \rangle$  denotes the standard  $L^2$  inner-product (linear in the first argument and antilinear in the second), and  $a$  denotes the sesquilinear form generated by  $\mathcal{L}$ .

From the Lagrange identity [29],

$$\langle \mathcal{L}\mathbf{u}, \mathbf{v} \rangle = \langle \mathbf{u}, \mathcal{L}^*\mathbf{v} \rangle, \quad (2.3)$$

we find the defining equality for constructing the adjoint operator  $\mathcal{L}^*$  associated with the adjoint problem

$$\mathcal{L}^*\mathbf{v} = \mathbf{p} \quad (2.4)$$

for an excitation  $\mathbf{p}$ , along with its own variational formulation involving the adjoint sesquilinear form  $a^*$ , analogous to that of (2.2).

Starting from the left-hand-side of the Lagrange identity, we manipulate the inner-product, mainly through integration by parts, to transform the operations on the forward solution  $\mathbf{u}$  onto the adjoint solution  $\mathbf{v}$ . In the process of performing these operations, the requirements of  $\mathbf{v}$ , which we assume at first to be an arbitrary function, unfold, namely the differentiability, integrability (including in the sense of the Cauchy principal value, as is necessary in the case of the EFIE and the coupled EFIE-MFIE), etc., and the boundary conditions. These operations typically result in terms on the boundary (e.g., line integrals) which, in total, must be equal to zero [29].

Let us first study the EFIE separately, assuming PEC structures.

We have the boundary condition on the electric field

$$[\mathbf{E}(\mathbf{J}_S, \varepsilon_1, \mu_1)]_{\text{tang}} + (\mathbf{E}_i)_{\text{tang}} = 0, \quad (2.5)$$

for complex permittivity  $\varepsilon_1$  and complex permeability  $\mu_1$ .

The scattered field in the region of complex permittivity  $\varepsilon$  and complex permeability  $\mu$  is

$$\mathbf{E} = \mathbf{E}_J(\mathbf{J}_S) = \mathcal{L}_{EE}\mathbf{J}_S, \quad (2.6)$$

where

$$\begin{aligned} \mathcal{L}_{EE}\mathbf{J}_S &= -j\omega\mathbf{A} - \nabla V, \\ \mathbf{A} &= \mu \int_{S'} \mathbf{J}_S g dS', \quad V = \frac{j}{\omega\varepsilon} \int_{S'} \nabla'_S \cdot \mathbf{J}_S g dS', \\ g &= \frac{e^{-\gamma R}}{4\pi R} = \frac{e^{-\gamma|\mathbf{r}-\mathbf{r}'|}}{4\pi|\mathbf{r}-\mathbf{r}'|} \end{aligned} \quad (2.7)$$

where  $\omega$  denotes the angular frequency and  $\gamma$  denotes the complex-valued propagation coefficient in the medium [10–12]. Furthermore, in line with (2.2), we let  $a_{EE}$  denote the sesquilinear form generated by  $\mathcal{L}_{EE}$  with  $B \subset H(\text{div}; \Omega)$ , where  $\Omega$  denotes a 2-D manifold embedded in 3-D space, as derived in [10]. A detailed description of the EFIE, as well as the PMCHWT formulation of the EFIE-MFIE may be found in [11], along with comparisons to the other formulations of the SIE problem (e.g., the combined field integral equation).

Starting from the Lagrange identity (2.3) and with the adjoint solution  $\mathbf{v}_E$ , the goal is to identify the adjoint operator  $\mathcal{L}_{EE}^*$  such that

$$\langle \mathcal{L}_{EE}\mathbf{J}_S, \mathbf{v}_E \rangle = \langle \mathbf{J}_S, \mathcal{L}_{EE}^*\mathbf{v}_E \rangle, \quad (2.8)$$

Performing integration by parts on the left-hand side of (2.8) and taking that  $\mathbf{v}_E \in B \subset H(\text{div}; \Omega)$ , as for the forward solution, satisfies each condition (such as the required integrability), and due to the normal continuity, the resulting line boundary terms vanish. In other words, the line boundary terms vanish in the same way as for the weak form of the forward problem, e.g., as in [10–12].

Hence, we have the final form for the adjoint operator,

$$\mathcal{L}_{\text{EE}}^* \mathbf{v}_E = j\omega\mu^* \int_S \mathbf{v}_E g^* dS + \frac{j}{\omega\varepsilon^*} \int_S \nabla' (g^* \nabla_S \cdot \mathbf{v}_E) dS, \quad (2.9)$$

of the EFIE problem.

Most importantly, however, for finding the Galerkin approximate solution (i.e., when  $B$  is finite dimensional), the formation of the Galerkin system matrix for the adjoint problem amounts to exchanging the roles of the trial and test functions (i.e., taking the transpose) and, due to the definition of the inner-product, taking the complex conjugate relative to the Galerkin system matrix of the associated forward problem.

That is, rather than considering an adjoint variational formulation of (2.6) explicitly, we need only find  $\mathbf{v}_E \in B$  such that

$$a_{\text{EE}}(\phi, \mathbf{v}_E) = \langle \phi, \mathbf{p} \rangle \quad \forall \phi \in B, \quad (2.10)$$

where the ordering of the trial function  $\mathbf{v}_E$  and test function  $\phi$  in relation to the pattern of the sesquilinear form for the forward problem (2.2) is of critical importance. Note, however, that as the EFIE is symmetric, the solution of the adjoint problem is simplified as in the case of the forward problem, which provides an efficiency enhancement to the analysis of PEC targets.

Now that we formed the adjoint problem associated with the EFIE (for PEC materials), let us consider the procedure applied to the coupled EFIE-MFIE problem for composite structures.

In the EFIE-MFIE case, we have the following set of boundary conditions:

$$[\mathbf{E}(\mathbf{J}_S, \mathbf{M}_S, \varepsilon_1, \mu_1)]_{\text{tang}} + (\mathbf{E}_i)_{\text{tang}} = [\mathbf{E}(-\mathbf{J}_S, -\mathbf{M}_S, \varepsilon_2, \mu_2)]_{\text{tang}}, \quad (2.11)$$

$$[\mathbf{H}(\mathbf{J}_S, \mathbf{M}_S, \varepsilon_1, \mu_1)]_{\text{tang}} + (\mathbf{H}_i)_{\text{tang}} = [\mathbf{H}(-\mathbf{J}_S, -\mathbf{M}_S, \varepsilon_2, \mu_2)]_{\text{tang}}, \quad (2.12)$$

with  $\varepsilon_1, \mu_1, \varepsilon_2, \mu_2$  representing the complex valued material parameters outside and inside the scatterer, respectively. Considering the PMCHWT formulation of the EFIE-MFIE exclusively, the

scattered field in the region of complex permittivity  $\varepsilon$  and complex permeability  $\mu$  is

$$\mathbf{E} = \mathbf{E}_J(\mathbf{J}_S) + \mathbf{E}_M(\mathbf{M}_S) = \mathcal{L}_{EE}\mathbf{J}_S + \mathcal{L}_{EM}\mathbf{M}_S, \quad (2.13)$$

and, likewise, the scattered magnetic field in the region of complex permittivity  $\varepsilon$  and complex permeability  $\mu$  is

$$\mathbf{H} = \mathbf{H}_M(\mathbf{M}_S) + \mathbf{H}_J(\mathbf{J}_S) = \mathcal{L}_{MM}\mathbf{M}_S + \mathcal{L}_{ME}\mathbf{J}_S, \quad (2.14)$$

where

$$\begin{aligned} \mathcal{L}_{EM}\mathbf{M}_S &= -\frac{1}{\varepsilon}\nabla \times \mathbf{F}, \\ \mathbf{F} &= \varepsilon \int_{S'} \mathbf{M}_{Sg} dS', \quad \mathcal{L}_{MM}\mathbf{M}_S = -j\omega\mathbf{F} - \nabla U, \\ \mathcal{L}_{ME}\mathbf{J}_S &= \frac{1}{\mu}\nabla \times \mathbf{A}, \quad U = \frac{j}{\omega\mu} \int_{S'} \nabla'_S \cdot \mathbf{M}_{Sg} dS', \end{aligned} \quad (2.15)$$

and with  $\mathbf{E}_J$  as in the EFIE expression, see [10]. For this coupled problem, we then have the variational formulation: Find  $\mathbf{u} = \{\mathbf{J}_S, \mathbf{M}_S\} \in B \subset H(\text{div}; \Omega) \times H(\text{div}; \Omega)$  such that

$$a_{E-M}(\mathbf{u}, \phi) = \langle \mathbf{f}, \phi \rangle \quad \forall \phi \in B, \quad (2.16)$$

where  $a_{E-M}$  represents the sesquilinear form generated by (2.13) and (2.14) [10], and  $\mathbf{f}$  is the excitation formed by the incident electric and magnetic fields as in (2.11) and (2.12).

The form of the adjoint problem may be found by first considering a single region (e.g., the exterior region) separately in (2.13) and (2.14) due to the operational symmetry. Furthermore, in the same manner as for the EFIE, from the Lagrange identity (2.3), constructing the Galerkin system matrix for the dual EFIE-MFIE mechanically only requires exchanging the roles of the trial and test functions (i.e., the transpose of the system matrix) and taking the complex-conjugate (due to the definition of inner-product) of the Galerkin system matrix of the associated forward problem. Explicitly, for the adjoint solution of the coupled EFIE-MFIE, we seek  $\mathbf{v} = \{\mathbf{v}_E, \mathbf{v}_M\} \in B$  such that

$$a_{E-M}(\phi, \mathbf{v}) = \langle \phi, \mathbf{p} \rangle \quad \forall \phi \in B, \quad (2.17)$$

(once again noting the position of the trial and test functions) where, in this case, as both the electric and magnetic current densities in the forward belong to  $H(\text{div}; \Omega)$  as noted above,  $B \subset H(\text{div}; \Omega) \times H(\text{div}; \Omega)$ .

## 2.2.2 Computing the Excitation for the Adjoint Problem

To build an excitation for the specified adjoint problems, as in [2], we consider a linear functional  $J$  of the forward solution  $\mathbf{u}$ , where, according to Riesz representation theorem, there exists  $\mathbf{p}$ , known as the Riesz representation of  $J$ , such that for all  $\mathbf{u}$

$$J[\mathbf{u}] = \langle \mathbf{u}, \mathbf{p} \rangle, \quad (2.18)$$

and where  $\mathbf{p}$  represents the same quantity in the definition of the adjoint problem (2.4). We note that solving the dual problem, either for the dual EFIE or the coupled dual EFIE-MFIE, does not require an explicit form for  $\mathbf{p}$  as only the ability to evaluate the QoI itself is necessary; i.e., as depicted in (2.17), we need only compute

$$\langle \phi, \mathbf{p} \rangle = J[\phi], \quad (2.19)$$

for all the test functions  $\phi$ .

In the following examples, we study the radar cross-section (RCS) of the scattering target. While scalar, the RCS is not inherently a linear functional of the scattered field  $E^{\text{sc}}[\mathbf{u}]$ ,

$$\mathbf{E}^{\text{sc}}[\mathbf{u}] = \left( -j\omega\mu \int_S \mathbf{J}_S g + k^{-2} \nabla_S \cdot \mathbf{J}_S \nabla g dS + \int_S \mathbf{M}_S \times \nabla g dS \right), \quad (2.20)$$

which *is* a linear functional of  $\mathbf{u}$ , and therefore must first be linearized. Examining the RCS, which we denote by  $\sigma$ , we have that

$$\sigma = \lim_{r \rightarrow \infty} \left( 4\pi r^2 \frac{|\mathbf{E}^{\text{sc}}|^2}{|\mathbf{E}^{\text{inc}}|^2} \right), \quad (2.21)$$

where, for simplicity, instead of treating (2.21) in the limit, let us assume that  $r$  is fixed sufficiently far away (i.e.,  $r \gg \lambda$ , where  $\lambda$  denotes the wavelength). Note, of course, that the RCS in (2.21) implicitly depends on the scattering angle. Naturally, the scattered field (2.20) may be employed as a proxy for the RCS, albeit with a detriment to the efficiency of the refinement for the overall

objective as only the magnitude of the scattered field is relevant (as opposed to the full complex valued quantity) and, since the right-hand side of the adjoint problem demands a scalar QoI, one adjoint excitation would be required for each component of the scattered electric field for full reconstruction.

Now, as  $|\mathbf{E}^{sc}|^2 = (\mathbf{E}^{sc})^H \mathbf{E}^{sc}$  is not analytic, the linearization of the RCS must be performed by considering the Wirtinger derivatives. Hence, we have that the first order expansion of the RCS about a reference point  $\mathbf{E}_0$  is

$$\sigma(\mathbf{E}^{sc}) \approx \sigma(\mathbf{E}_0) + 2\text{Re} \left\{ \frac{\partial \sigma}{\partial \mathbf{E}^{sc}} (\mathbf{E}^{sc} - \mathbf{E}_0) \right\}, \quad (2.22)$$

where

$$\frac{\partial \sigma}{\partial \mathbf{E}^{sc}} = \frac{1}{2} \left( \frac{\partial \sigma}{\partial \text{Re}(\mathbf{E}^{sc})} - j \frac{\partial \sigma}{\partial \text{Im}(\mathbf{E}^{sc})} \right) \quad (2.23)$$

denotes the first Wirtinger derivative.

Expanding (2.22) by the evaluation of (2.23), we have that

$$\sigma(\mathbf{E}^{sc}) \approx \sigma(\mathbf{E}_0) + 8\pi r^2 \text{Re} \left\{ \mathbf{E}_0^H (\mathbf{E}^{sc} - \mathbf{E}_0) \right\}, \quad (2.24)$$

which completes the first order approximation of the RCS.

Now, as for the application of this quantity to form the excitation of the adjoint problem, two additional changes must be made. Firstly, taking the real part is not a linear operation in  $\mathbb{C}$  and therefore violates the requirements of the QoI. Secondly, (2.24) is otherwise an affine function. These two obstacles motivate the construction of the following QoI, which satisfies the requirements for the DWR error estimation,

$$J[\mathbf{u}; \mathbf{E}_0] = 8\pi r^2 \mathbf{E}_0^H \mathbf{E}^{sc}[\mathbf{u}], \quad (2.25)$$

where, as noted above,  $r \gg \lambda$ .

To evaluate the effectiveness of this QoI for estimating the error of the RCS, let us take two approximations of the solution  $\mathbf{u}$ ,  $\mathbf{u}_1$  and  $\mathbf{u}_2$ , and the corresponding approximations of the scattered

field  $\mathbf{E}_1^{sc}$  and  $\mathbf{E}_2^{sc}$  for  $r \gg \lambda$ . From (2.24), we have that

$$\sigma(\mathbf{E}_1^{sc}) - \sigma(\mathbf{E}_2^{sc}) \approx 8\pi r^2 \text{Re} \{ \mathbf{E}_0^H (\mathbf{E}_1^{sc} - \mathbf{E}_2^{sc}) \}, \quad (2.26)$$

which, from (2.25), is equivalent to  $\text{Re} \{ J[\mathbf{u}_1 - \mathbf{u}_2; \mathbf{E}_0] \}$ . In other words, computing the error for the QoI (2.25) produces the same error (after extracting just the real component) as for the first order expansion (2.24).

As for the reference point  $\mathbf{E}_0$ , we note that the adjoint problem, when solved after the forward problem, has access to the approximate solution to the forward problem (and therefore its own estimate of the RCS and the scattered field). Hence,  $\mathbf{E}_0$  is taken as this estimate of the scattered field. As the adaption method (described in Section III) proceeds iteration by iteration and the quality of the discretization improves,  $\mathbf{E}_0$  is similarly enhanced, resulting in improved agreement between the linearized RCS (2.24) and the actual RCS. Moreover, as a consequence of this improved agreement, the quality of (2.25) for estimating the error in RCS for refinement increases.

Finally, just as in the forward problem, where multiple excitations may be solved for limited cost (when using a direct solver), multiple QoIs (e.g., multiple scattering angles) may be solved for efficiently through simple substitution of multiple right-hand sides. Of course, in the adaptive refinement process handling multiple QoIs in this manner requires accumulating the refinement directives such that a single discretization yields the desired accuracy for the entire QoI collection.

## 2.3 Error Estimation and Adaption

With the adjoint solution computed (either for a single QoI or multiple), the estimation of the QoI error contributions proceeds in an identical fashion to [2]. The error induced by solving the integro-differential equation approximately,

$$\mathbf{e} = \mathbf{u} - \mathbf{u}_p, \quad (2.27)$$

where  $\mathbf{u}_p \in B_p$  represents the Galerkin approximate solution for a finite dimensional subspace  $B_p \subset H(\text{div}; \Omega)$  (for the EFIE) or  $B_p \subset H(\text{div}; \Omega) \times H(\text{div}; \Omega)$  (for the coupled EFIE-MFIE), translates to an error in the functional

$$J[\mathbf{e}] = J[\mathbf{u}] - J[\mathbf{u}_p] \quad (2.28)$$

by linearity of  $J$ . From (2.18) and the Lagrange identity (2.3), this error may be further expressed as

$$\begin{aligned} J[\mathbf{e}] &= \langle \mathbf{e}, \mathbf{p} \rangle \\ &= \langle \mathcal{L}\mathbf{e}, \mathbf{v} - \psi_p \rangle \\ &= \langle \mathbf{f}, \mathbf{v} - \psi_p \rangle - a(\mathbf{u}_p, \mathbf{v} - \psi_p), \end{aligned} \quad (2.29)$$

for arbitrary  $\psi_p \in B_p$  (due to Galerkin orthogonality) and where  $a$  denotes the sesquilinear form, either for the EFIE or the EFIE-MFIE, with  $\mathbf{v}$  representing the respective solution to the adjoint problems defined in (2.10) or (2.17) for the choice of the QoI. While the choice of  $\psi_p$  does not affect the evaluation of  $J[\mathbf{e}]$ , the choice of  $\psi_p = \mathbf{\Pi}_p \mathbf{v}$ , the projection of the adjoint solution  $\mathbf{v} \in B$  onto the solution space of the forward problem  $B_p$ , tunes the resulting cellwise error contribution estimates by eliminating irrelevant contributions for the purposes of addressing the insufficient and inefficient regions of the discretization. If only an error estimate is required rather than adaptive refinement indicators,  $\psi_p = 0$  may be chosen to eliminate the subtraction in (2.29). The evaluation of (2.29) quantifies the contributions of the approximation error of the electric current densities and magnetic current densities (for the coupled EFIE-MFIE) to the error in the functional  $J$ , with the computations required (i.e., for evaluating the inner-product and sesquilinear form in (2.29)) of the same manner as required for the filling of the Galerkin system matrix.

The previous expressions assume access to the exact adjoint solution  $\mathbf{v}$ ; however, in general we must substitute a numerical approximation. To produce a usable (i.e., non-zero) estimate, we opt to solve the adjoint problem for  $\mathbf{v}_{p+} \in B_{p+}$ , where  $B_{p+} \supset B_p$  denotes the enriched space produced by increasing the expansion orders of every cell in the discretization of the forward problem by one, as seeking the approximate solution to the adjoint problem in the same space as the forward solution results in an estimate of zero error due to Galerkin orthogonality. While increasing the polynomial

order provides excellent error estimation information, cheaper alternatives, such as those discussed in [28], may be more suitable for certain applications. Given that we have substituted a second approximation into the error expression, we briefly examine the effect on the error estimate similarly to the demonstrations in [49]. Expanding the difference between the exact error  $J[\mathbf{e}]$  and the error estimate, which we denote by  $\tilde{J}[\mathbf{e}]$ , we have that

$$\begin{aligned} J[\mathbf{e}] - \tilde{J}[\mathbf{e}] &= \langle \mathbf{f}, \mathbf{v} \rangle - a(\mathbf{u}_p, \mathbf{v}) - \langle \mathbf{f}, \mathbf{v}_{p+} \rangle + a(\mathbf{u}_p, \mathbf{v}_{p+}) \\ &= a(\mathbf{u} - \mathbf{u}_p, \mathbf{v} - \mathbf{v}_{p+}), \end{aligned} \quad (2.30)$$

i.e., the quality of the error estimate depends simultaneously on the approximation error of the forward solution and the adjoint solution.

Of course, in contrast to the FEM case with contributions automatically localized to an individual cell, the proper accumulation of contributions in the case of the SIE problem is potentially ambiguous given the global interactions resulting from the Green's function. However, note that the assembly of (2.29) divides in a piecewise fashion according to interactions between pairs of cells and—within each pair of cells—a shape function for the forward solution and a shape function for the adjoint solution. Explicitly, for the error contribution estimate  $\tilde{e}_i$  of cell  $i$ ,  $i = 1, \dots, K$ , we compute

$$\tilde{e}_i = \langle \mathbf{f}, \mathbf{v}_{p+} - \mathbf{\Pi}_p \mathbf{v}_{p+} \rangle_i - a_i(\mathbf{u}_p, \mathbf{v}_{p+} - \mathbf{\Pi}_p \mathbf{v}_{p+}), \quad (2.31)$$

where the subscript  $i$  denotes the restriction of the inner-products over cell  $i$ , where, crucially, the portion of the adjoint solution under consideration is associated. Note that internally, the evaluation of the sesquilinear form in the error estimate traverses every cell in the discretization for the integration of the components related to the forward problem and its solution.

However, we note an exception to the contribution accumulation rule established in (2.31): when a contribution from a boundary DoF in the discretization of the adjoint problem (i.e., the normal component is non-zero on an edge for that DoF) arises due to the insufficient expansion order of a neighboring cell, the contribution is assigned entirely to that lower order neighbor to ensure that when treated as refinement indicators, the error contributions correctly identify the regions of the

discretization that require improvement. Even so, this approach preserves the expression of the total QoI error so that

$$J[\mathbf{e}] \approx \sum_{i=1}^K \tilde{e}_i. \quad (2.32)$$

The contributions, additionally, when accumulated per direction within each cell or individually for the electric and magnetic current densities, permits additional refinement classification information.

With adequate error estimates and refinement indicators, any successful adaptive error control strategy must drive two simultaneous developments in the discretization. Naturally, the primary goal of mesh adaption is to reach a termination condition in the overall error. However, the adaption must also encourage error homogenization. As shown in [50], the ideal discretization (i.e., the discretization which achieves both accuracy and efficiency) requires homogenization of error contribution estimates. Regions of a discretization with excessively large error contribution estimates, for example, indicate mesh insufficiency, while regions with null error contribution estimates indicates inefficiency and the profitability of coarsening.

In response to these complementary goals and to guide the adaptive refinement process, similarly to [2], we impose the following *a priori* local (i.e., interpolatory)  $p$ -refinement error convergence heuristic based on the theoretical solution error bounds derived in [51], which, while not strictly satisfied, facilitates both the determination of effective refinement gradation to reduce the number of iterations required in the refinement procedure (i.e., to reduce the number of linear systems that must be solved to reach a desired accuracy) and the improvement of mesh equilibration:

$$|\tilde{e}_i| \approx C p_i^{-(r+1/2)}, \quad (2.33)$$

where  $p_i$  denotes the degree of the polynomial basis on the cell,  $r$  denotes the Sobolev regularity of the solution,  $C$  is an unknown coefficient, and  $\tilde{e}_i$  represents the known error contribution estimate computed in (2.31). While we exclusively study  $p$ -refinement in this manner, the same process may be repeated for guiding  $h$ -refinements. Note that this condition is based on derivations for the

approximation error from [51], rather than the error in some functional or the contributions to the error in the functional as we are studying here. However, only a rough form relating the behavior of the local contributions to the error and discretization choices (namely, the size of the cell or its expansion order) is sufficient for acceleration, given the necessarily iterative refinement procedure.

By predicting refinements from the error contribution estimates computed in (2.31) via a suitable adjoint solution combined with the imposed convergence condition (2.33), we can map the existing properties of the discretization (e.g., the expansion orders and error contribution estimates on each cell) to update parameters that target the aforementioned adaptive refinement goals, namely to reach a desired accuracy with an awareness and promotion of equilibration.

As to the termination of the refinement procedure, we require that the absolute value of the error contribution estimate  $\tilde{e}_i$  for each cell  $i$  falls below an absolute threshold  $T_{\text{local}}$  such that

$$|\tilde{e}_i| \leq T_{\text{local}}. \quad (2.34)$$

Then, for an update equation of the expansion order on cell  $i$ , according to the termination condition (2.34), we would like to find  $p' > p$  (in the case of refinement when  $|\tilde{e}_i| > T_{\text{local}}$ ) such that

$$|\tilde{e}'_i| \approx C(p'_i)^{-(r+1/2)} \approx T_{\text{local}}, \quad (2.35)$$

where  $\tilde{e}'_i$  denotes the predicted error contribution after increasing  $p$  to  $p'$ .

Now, while estimating the Sobolev regularity is possible (e.g., as in [52]), let us instead follow an alternative condition, namely that if we were to conduct  $p$ -refinement, then we should assume the solution is sufficiently regular such that  $p$ -refinement is profitable (otherwise, an  $h$ -refinement should be executed to "isolate" non-smooth behavior [53, 54]). In other words, for an as-of-yet unknown expansion order  $p'$ , we assume that  $r \geq p'$ , and, in particular, for the purposes of leveraging (2.33) for an easily computable update equation, we take  $r = p' + 1$ .

Then, using the *a posteriori* error estimate to approximate  $C$  (i.e.,  $C \approx |\tilde{e}_i| p_i^{(r+1/2)}$ ), the predicted value of  $p'$  may be found by solving

$$\frac{p^{(p'+3/2)}}{p'^{(p'+3/2)}} - \frac{T_{\text{local}}}{|e_i|} = 0, \quad (2.36)$$

for  $p'$  by, e.g., Newton's method. Furthermore, since an integer is needed, the ceiling of the value obtained from (2.36) is taken.

For coarsening when  $|\tilde{e}_i| \ll T_{\text{local}}$ , a similar approach can be taken. In this case, from (2.35) we seek  $p' < p$  such that

$$p' = \left\lceil p \left( \frac{T_{\text{local}}}{|e_i|} \right)^{-1/(p+3/2)} \right\rceil, \quad (2.37)$$

where the same regularity assumption as before was applied with the known value  $p$  as opposed to  $p'$ .

Note that especially in the case of  $h$ -refinements, the execution of the adaptivity directives is constrained by practical limitations, e.g., how a cell may be subdivided or combined with its neighbors (in the case of coarsening).

Of course, in practice we must also consider that a discretization may start in the preasymptotic region, in which case the degree of refinement in a single iteration should be truncated. Moreover, in such cases, the estimate of the absolute error might increase (temporarily) as the discretization improves. For pure  $p$ -refinement, the limiting case is simply increasing (or decreasing) the expansion order by 1, but often increases by 2 or 3 may be made with confidence. For automatic control of this limit, restrictions may be imposed on the max increase if the estimated relative error in the QoI,

$$\frac{|\sum_{i=1}^K \tilde{e}_i|}{|J[\mathbf{u}_p] + \sum_{i=1}^K \tilde{e}_i|}, \quad (2.38)$$

exceeds some threshold. Furthermore, the coarsening facilitated by (2.37) permits correcting mistaken over-refinement.

We emphasize that the tolerance  $T_{\text{local}}$  is not a normalized quantity. Nevertheless, an automatic selection of  $T_{\text{local}}$  from a desired relative tolerance can be achieved even without prior knowledge of the magnitude of the QoI. From the initial discretization, a coarse computation of the QoI, while inaccurate, typically yields a result within an order of magnitude of the actual QoI, from which the necessary value for  $T_{\text{local}}$  may be found for a given desired overall relative error. As the discretization quality increases as well, updating the tolerance  $T_{\text{local}}$  each iteration based on the enhanced QoI data enables improved selection of the refinement criterion. In the numerical results section, from a desired relative global tolerance  $T_{\text{rel}}$ , we estimate the necessary local absolute tolerance  $T_{\text{local}}$  by selecting

$$T_{\text{local}} = \alpha \frac{T_{\text{rel}} \left| J[\mathbf{u}_p] + \sum_{i=1}^K \tilde{e}_i \right|}{K} \quad (2.39)$$

where, since the tolerances cannot be satisfied exactly and given the effects of error cancellation,  $\alpha > 1$  to provide a closer estimate of the necessary tolerance. In the numerical results section, we take  $\alpha = 20$  as a reasonable amplification, which results in relative errors typically within an order of magnitude of the desired without further adaptivity. While the refinement procedure is not extremely sensitive to this choice, precise satisfaction of the desired relative error may require additional adaptivity.

Finally, we reiterate that given the practical limitations of how cells may be refined, i.e., how a cell is subdivided or that the expansion order must be a strictly positive integer, as well as the necessarily iterative nature of any refinement procedure, more sophisticated marking for acceleration is typically not necessary. The computed error contribution estimates may also be applied in more traditional ways, though perhaps with reduced mesh equilibration tendencies, such as with Dörfler marking [55], the dominant approach to marking cells for refinement, or hybridized with such approaches.

## 2.4 Numerical Results

We now present a series of numerical examples that deploy the proposed SIE adaptive mesh refinement (AMR) technique for  $p$ -refinement. A similar procedure may be applied in the case of  $h$ -refinement; however, effective  $h$ -refinement—particularly when working with quadrilateral patches as in this work—in practice relies heavily on proper remeshing or the handling of non-conformal cells, e.g., 1-irregular meshes, both of which are beyond the scope of this manuscript. In each case we start with an extremely coarse discretization (in terms of the accuracy) and we truncate the maximum increase of a given cell’s expansion order in a single iteration by three, and, as a second restriction, we limit the maximum increase to one if the estimated global QoI relative error exceeds 10 (1000% error) to penalize the most significant over-refinements.

Finally, we emphasize that the computation of the error estimates as presented relies on solving the adjoint problem for the  $p$ -enriched space (by increasing the expansion orders by one relative to the discretization of the forward problem). The increase in the number of DoFs required for solving the higher-order adjoint problem is dependent on the size of problem and may therefore be substantial. As a mitigating factor in the expense of this approach, the computations for assembling the Galerkin system matrix for the adjoint problem may be reused for the forward problem (i.e., by extracting a subset of the system matrix) by employing hierarchical basis functions. Furthermore, the most expensive computations may be reused between iterations such that a small change in the discretization requires a small increase in computation time associated with the new entries in the Galerkin system matrix that must be filled, in addition to solving the linear systems. In order to examine the quality of the discretizations produced according to this approach specifically, rather than the quality of the adjoint solution, in the following examples we report the QoI without the enhancement provided by the sum of the error contribution estimates that are otherwise employed to dictate refinements as described in Section III; i.e., where applicable, we depict  $J[\mathbf{u}_p]$  as opposed to  $J[\mathbf{u}_p] + \sum_{i=1}^K \tilde{e}_i$ . A future work will explore enhancing the efficiency of the error estimation for SIE problems.

For the first example, we investigate application to a spherical scatterer for adaptive error control of the monostatic RCS. As outlined in Section II, we first compute the error contribution estimates according to the complex-valued QoI (2.25) and then discard the imaginary component to produce the error estimate for the real-valued linearized RCS (2.24) and the associated refinement indicators. We refine the scattering target to achieve an estimated relative QoI error of approximately  $T_{\text{rel}} \in \{1 \times 10^{-1}, 1 \times 10^{-2}, 4 \times 10^{-3}, 1 \times 10^{-3}\}$  by computing appropriate absolute local tolerances as provided by (2.39). The desired relative QoI error is used only to compute appropriate absolute local tolerances (updating each iteration); the termination of the refinement is provided exclusively by satisfaction of the local tolerances.

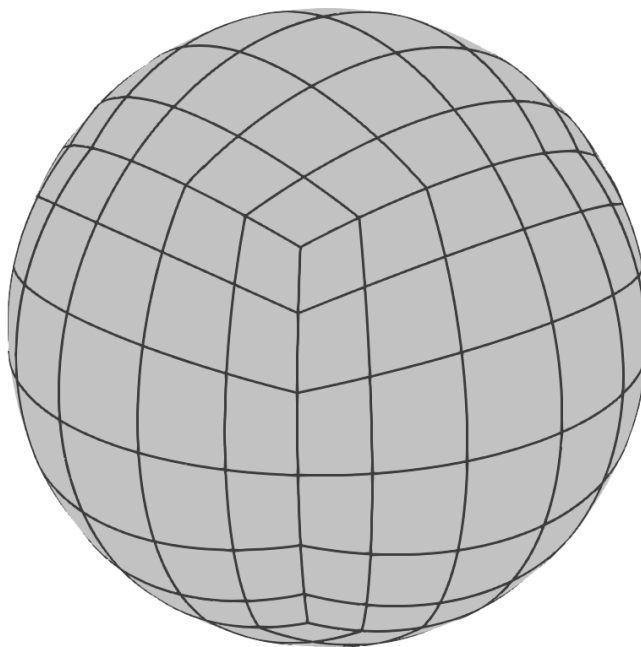


**Figure 2.1:** The starting discretization for the spherical scatterer  $S1$  with 216 geometrically bicubic elements and first order basis functions.

The first sphere has a complex relative permittivity of  $\varepsilon_r = 2.56 - j0.05$ , and the diameter is  $3\lambda_0$  (where  $\lambda_0$  denotes the wavelength in vacuum), which is analyzed with the coupled EFIE-MFIE in the PMCHWT formulation. We refer to this first scatterer by  $S1$ . The starting discretization, which consists of 216 geometrically bicubic elements with first order basis functions, is shown

in Fig. 2.1. Geometrically, the relative error of the surface area compared to a perfect sphere is  $1 \times 10^{-5}$ . In terms of the accuracy of the solution, the discretization is very coarse as the percent error (with respect to the analytical value computed from Mie scattering) of the RCS computed from the starting discretization is 97% for  $S1$ . Note that unless otherwise specified, the RCS is not expressed in decibels to facilitate direct comparison of the actual relative error with the estimated relative error produced internally by the adaptive refinement procedure as in (2.38). Finally, in the illustrations of the following results, we normalize the error contribution estimates at each iteration by the estimated magnitude of the QoI at that iteration to produce relative local error contribution estimates. Conveniently, for the procedure applied to  $S1$  as described above, this permits illustrating unified local (i.e., per-cell) relative tolerance refinement termination thresholds  $T_{S1L_i}$  from (2.39) such that

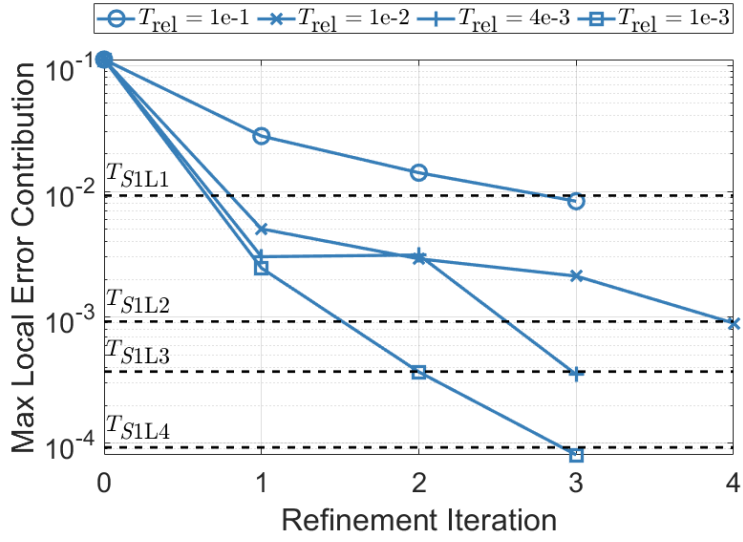
$$T_{S1L_j} = \alpha \frac{T_{relj}}{216}, \quad (2.40)$$

with  $j$  indexing the set of four relative tolerances above, as the absolute tolerances vary each iteration according to (2.39).

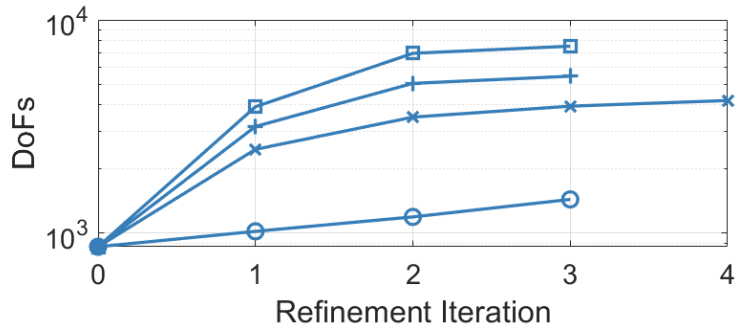
We now conduct the AMR procedure as outlined in Section III. As shown in Fig. 2.2(a), all examples attain the desired relative local tolerances rapidly. Except for the second coarsest tolerance, which required four iterations, the refinement procedure attained the desired local error contribution tolerance in three iterations. Furthermore, as seen in Fig. 2.2(b), for each example, only the first iteration drives a large change in the discretization, introducing many new DoFs, while the remaining iterations tune the allocation of unknowns with small adjustments. As a result, storing (and reusing) the Galerkin integrals between iterations results in vast reductions in computation time.

Illustrated in Fig. 2.2(c) and Fig. 2.2(d), the proposed approach rapidly improves the mean and standard deviation of the cellwise relative error contribution estimates corresponding to the various tolerances used, with finer tolerances permitting greater enhancement of both quantities.

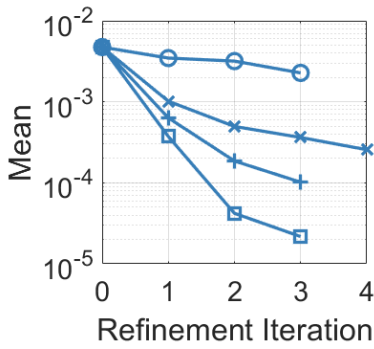
To examine the effect of the refinement on the exact and estimated relative error of the RCS, Fig. 2.3 illustrates the convergence of the computed RCS for the final discretizations produced



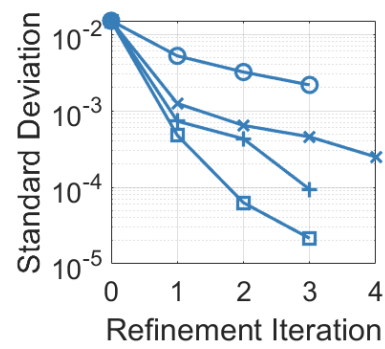
(a)



(b)



(c)



(d)

**Figure 2.2:** Performance of the AMR algorithm for the spherical scatterer  $S1$  for four tolerances. (a) Convergence of the relative maximum error contribution estimate versus the number of refinement iterations. (b) DoFs allocated by the AMR procedure at each iteration. (c) Mean of the relative error contribution estimates. (d) Standard deviation of the relative error contribution estimates. (a), (c), and (d) are normalized with respect to the magnitude of the QoI at each iteration to produce the relative quantities.

with increasingly fine tolerances for  $S1$ . Note that as the estimated relative error is computed for the linearized QoI, the difference between the actual relative error and the estimated is due both to the inexactness of the error estimation *and* the linearization (as well as other deterministic sources of error, e.g., from numerical integration or the geometrical discretization itself). Each data point is associated with one of the four tolerances tested, with the finest tolerance requiring the most DoFs and likewise for the other tolerances. The estimated relative error is reported as part of the AMR process using (2.38), whereas the exact relative error is computed by comparing the approximate RCS to that computed through the Mie series solution. Despite that the refinement procedure of one tolerance is entirely independent of the other tolerances, the proposed approach yields consistent and rapid convergence with finer tolerances and, correspondingly, more DoFs. For the finest tolerance, the procedure results in a relative error of the RCS of under  $1 \times 10^{-3}$  for  $S1$ , a significant improvement (by several orders of magnitude) over the starting discretization. In terms of the estimated relative error, the AMR procedure provides very close agreement to the exact values for the four tolerances, with the coarsest tolerance slightly underestimating the relative error and the finest tolerance slightly overestimating the error.

Solving the same problem with a uniformly refined (i.e., non-adaptive) discretization, a relative error of just over  $3 \times 10^{-3}$  for the RCS is achieved by 7776 DoFs. In other words, for fewer DoFs, the adaptive refinement procedure produces a discretization that is more than three times as accurate for computing the RCS.

As an illustration of the inherent mesh equilibration driven by the proposed method, Fig. 2.4 depicts the normalized cellwise error contributions for the starting discretization and the final discretization for the finest tolerance ( $T_{\text{rel}} = 1 \times 10^{-3}$ ) for the spherical scatterer  $S1$ . The starting discretization, shown in Fig. 2.4(a), exhibits extremely high error contribution concentration, indicating low efficiency and the overall low quality of the discretization. On the other hand, the discretization produced by the proposed AMR algorithm, Fig. 2.4(b), yields a significant reduction in error contribution concentration, with the estimates distributed about the discretization much more evenly, mirroring the results indicated by the significant improvement to the standard

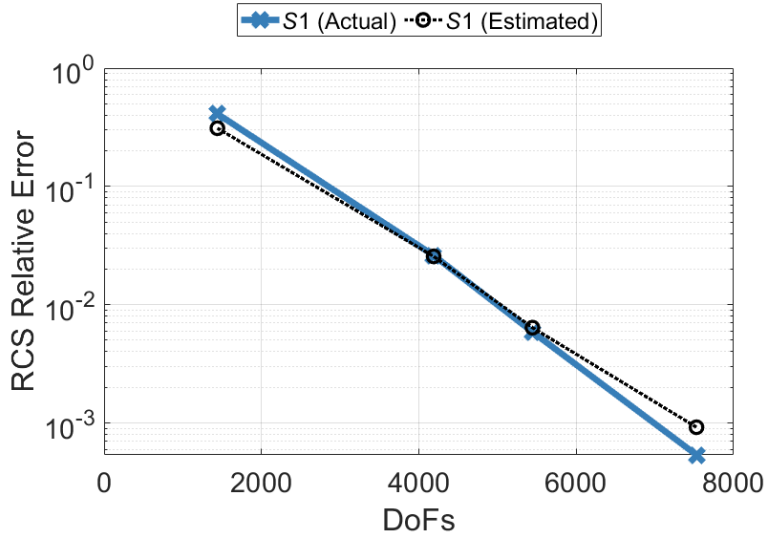


**Figure 2.3:** Convergence of the actual and estimated relative errors for the monostatic RCS of the dielectric spherical scatterer  $S1$ .

deviation of the error contributions in Fig. 2.2(d). Next, in Fig. 2.5(a) and Fig. 2.5(b), we examine

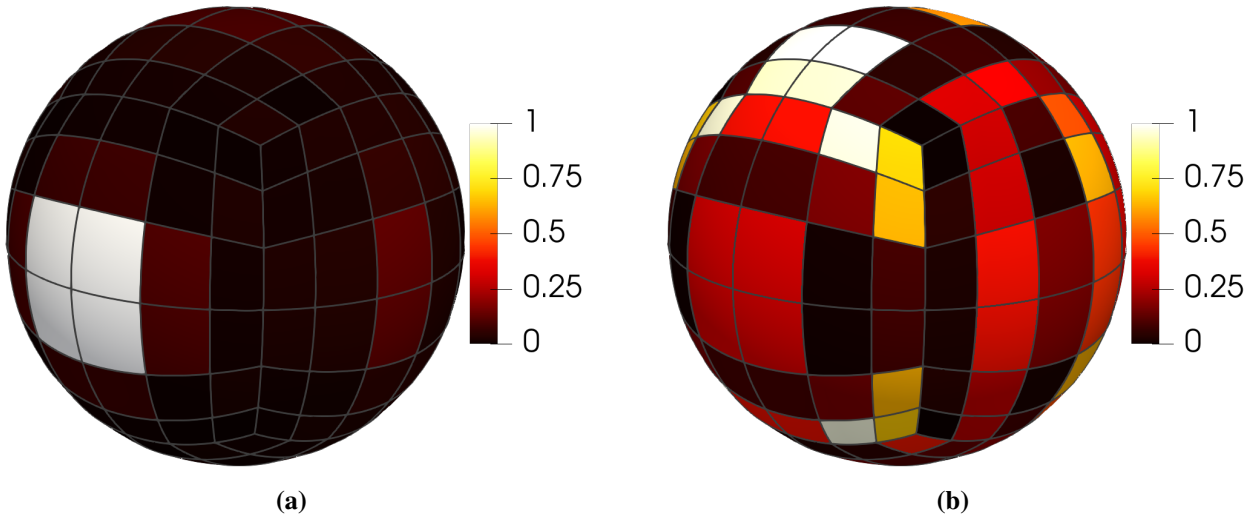


**Figure 2.4:** Illustration of the error contribution estimate distributions for the dielectric scatter  $S1$ . (a) Normalized error contribution estimates for the starting discretization of  $S1$ . (b) Normalized error contribution estimates for the final discretization of  $S1$  with  $T_{\text{rel}} = 1 \times 10^{-3}$ . For the purposes of illustration, in (a) and (b) the error contribution estimates on each cell are normalized such that the smallest has a value of zero, and the largest a value of one.

the final discretizations for  $S1$  for the coarsest tolerance and finest tolerance, respectively. Both

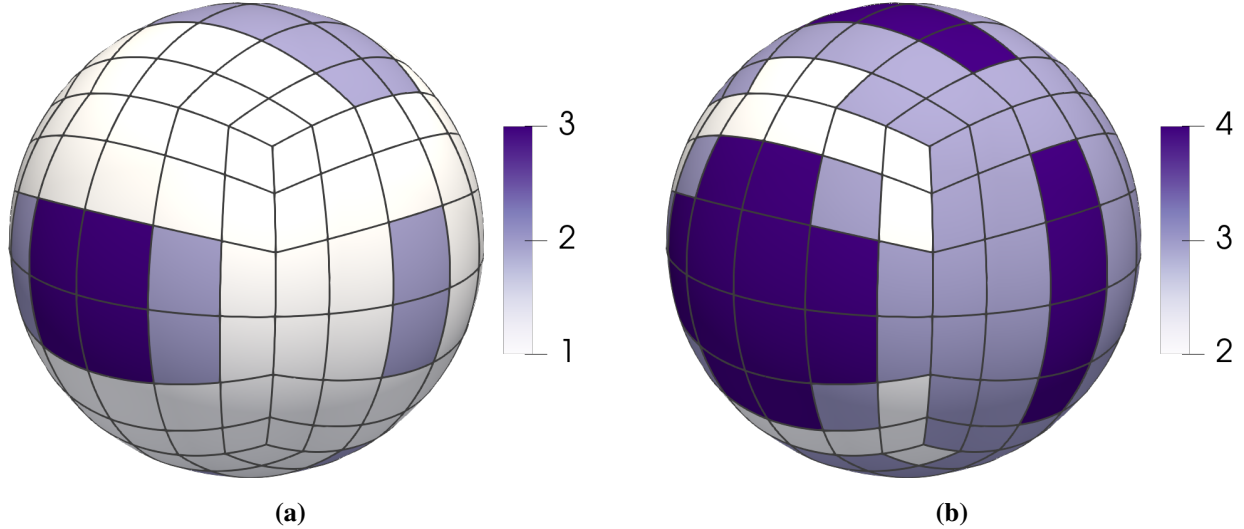


**Figure 2.5:** Illustration of the expansion orders for the coarsest and finest tolerances of the dielectric spherical scatterer  $S1$ . (a) The final discretization for the coarsest tolerance  $T_{S1L1}$  of  $S1$ . (b) The final discretization for the finest tolerance  $T_{S1L4}$  of  $S1$ .

discretizations exhibit significant overlap in terms of the general refinement pattern. However, the finest tolerance demands a much greater degree of refinement globally.

Fig. 2.6 depicts the distribution of expansion orders for the final discretizations of each model and each tolerance. The coarse tolerances tested retain even first order basis functions, while, as expected, the finer tolerances require increasingly higher expansion orders. The finest tolerance of  $S1$ , for example, requires up to fourth-order basis functions. Overall, however, third-order basis functions are required most frequently. These results confirm those found in [2], which indicated that high accuracy computations typically require at least cubic or quartic polynomial bases.

Finally, Fig. 2.7 documents the total cost (in terms of the number of DoFs) of solving both the forward and adjoint problems as outlined in Section II and Section III for the four tolerances tested. While the adjoint solution dominates the cost of the coarsest tolerance, the forward solution comprises more than half cost for the finer tolerances, lessening the relative computational cost even with the rudimentary approach to discretizing the adjoint problem.

While the first example illustrates the capability of the approach to attain high accuracy for spherical scatterers, we now study its application to another canonical scattering target in the form of the so-called NASA almond, introduced in [56]. In this case, the starting discretization—

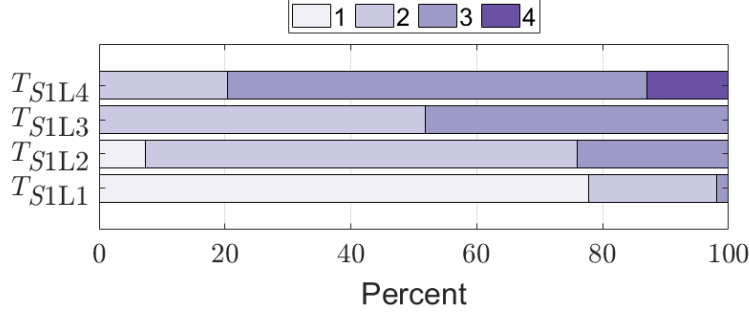


**Figure 2.6:** The distribution of expansion orders for the spherical scatterer  $S1$  for the four tolerances.

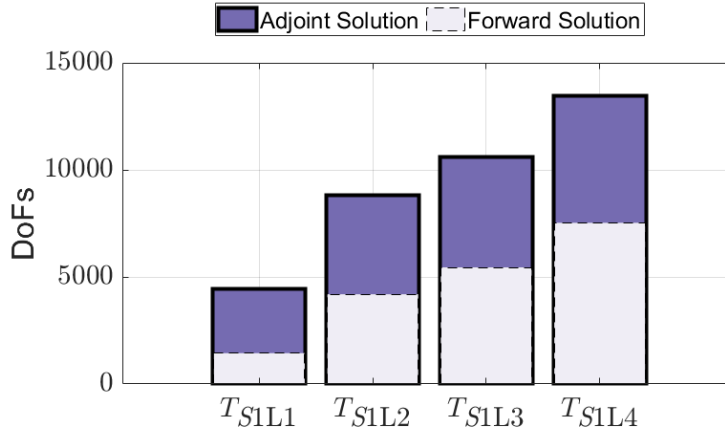


**Figure 2.7:** The total cost (in terms of the number of DoFs) of solving both the forward and adjoint problems for the spherical scatterer  $S1$  for the four tolerances.

illustrated in Fig. 2.8—consists of 136 geometrically biquadratic cells with first order basis functions. Proceeding in an identical fashion to the spherical scatterer, we refer to this scatterer by  $S2$ . We test the scatterer for  $\varepsilon_r = 4.5 - j0.05$ , where the longest dimension of the almond is  $3\lambda_0$  and we once again examine the monostatic RCS QoI through (2.25) with a planewave (polarized in the  $\theta$ -direction as in Fig. 2.8) incident at the nose of the almond ( $\theta = \pi/2, \phi = 0$ ).

In contrast to the previous example, the reference RCS is now computed from a significantly uniformly refined mesh, both in  $h$  (twice as many elements) and  $p$ , and features 17408 DoFs. Geometrically, the relative error of the surface area of  $S2$  compared to the reference model is  $4.6 \times 10^{-5}$ . However; in terms of the QoI, the RCS computed from the starting discretization yields a large percent error of 81% compared to this reference.

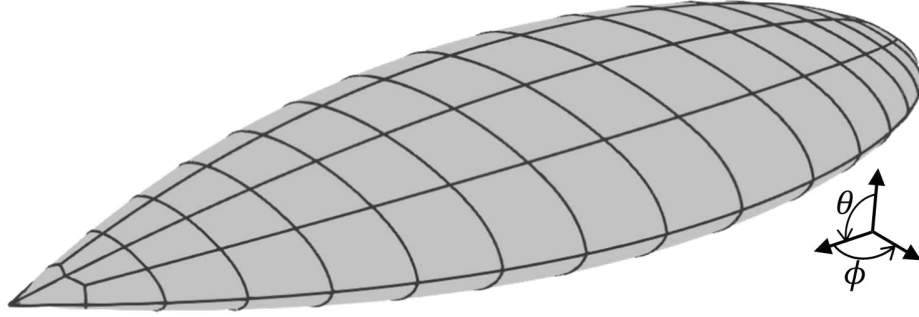


**Figure 2.8:** The starting discretization for the NASA Almond scatterer  $S2$  with 136 geometrically biquadratic elements and first order basis functions.

Once again, we define the relative local tolerance thresholds to be

$$T_{S2Lj} = \alpha \frac{T_{relj}}{136}, \quad (2.41)$$

where  $j$  indexes the set of four previously chosen relative tolerances.

Illustrated in Fig. 2.9, the performance with the NASA almond is nearly identical to the example with the sphere. The proposed approach rapidly refines the discretization for all the tolerances. Of the four tolerances, the coarsest tolerance requires four iterations (making very small changes), whereas the remaining tolerances each require three iterations. Likewise, we see again that the first iteration contributes the most to the change in the discretization with the subsequent iterations offering much smaller adjustments. Lastly, as in spherical case, the mesh equilibration is greatly improved with enhancements to the mean and standard deviation of the relative error contribution estimates as seen in Fig. 2.9(c) and (d).

Next, in Fig. 2.10, we again see very similar performance in terms of the computation of the RCS. The estimated error in the RCS, which we again note is for the linearized quantity as discussed in Section II, closely matches that of the actual, with the second to last iteration slightly underestimating the error in the QoI, with an estimated relative error of  $1.1 \times 10^{-3}$  compared to the actual relative error of  $1.9 \times 10^{-3}$ . Moreover, for computing the RCS with non-adaptive, uniform refinements, a relative error of  $2.3 \times 10^{-4}$  requires 8704 DoFs, indicating that the proposed adaptivity, which achieves a relative error of  $2.1 \times 10^{-4}$  by 4448 DoFs, drives significantly improved

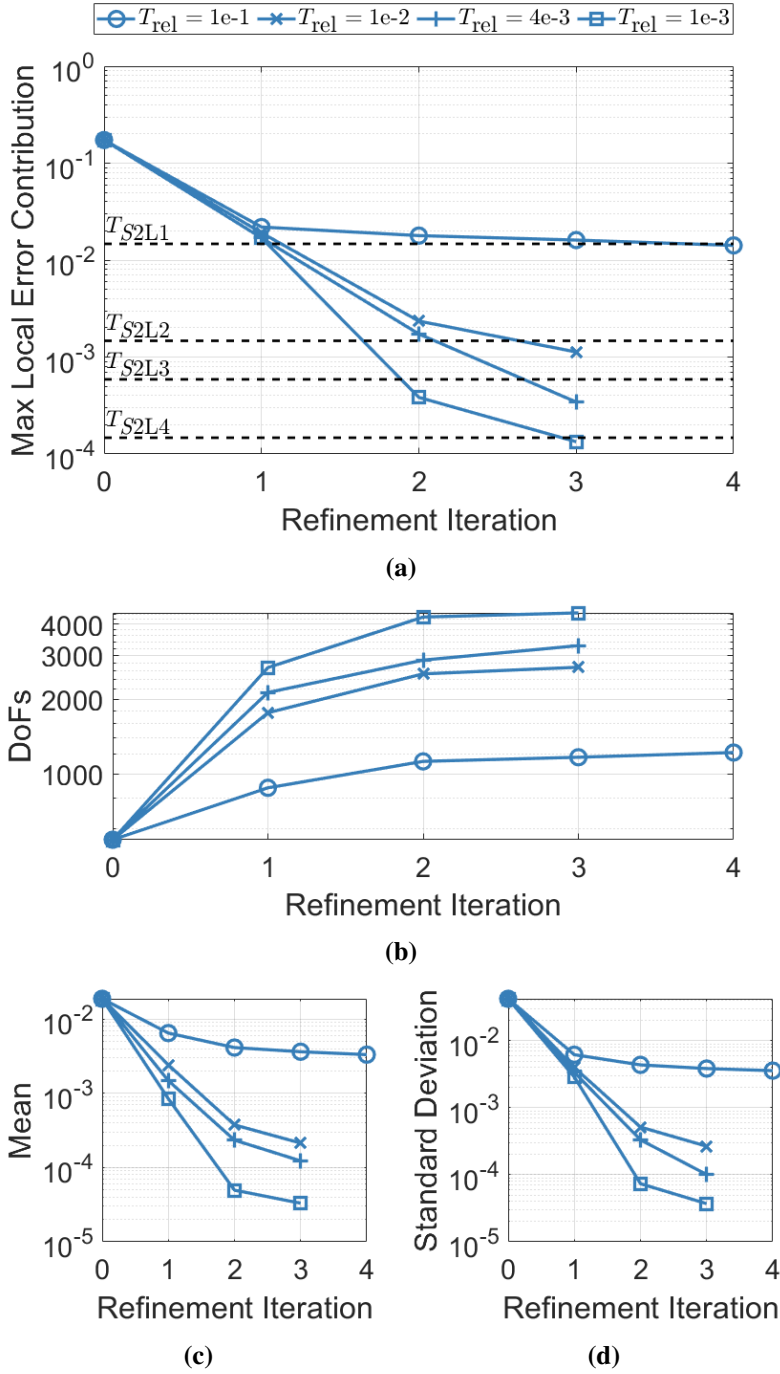


**Figure 2.9:** Performance of the AMR algorithm for the NASA almond scatterer  $S_2$  for four tolerances. (a) Convergence of the relative maximum error contribution estimate versus the number of refinement iterations. (b) DoFs allocated by the AMR procedure at each iteration. (c) Mean of the relative error contribution estimates. (d) Standard deviation of the relative error contribution estimates. (a), (c), and (d) are normalized with respect to the magnitude of the QoI at each iteration to produce the relative quantities.

error reduction efficiency. Even when compared to the coarser tolerances, uniform refinement requires 2176 DoFs to achieve a relative error of  $2.9 \times 10^{-2}$ .

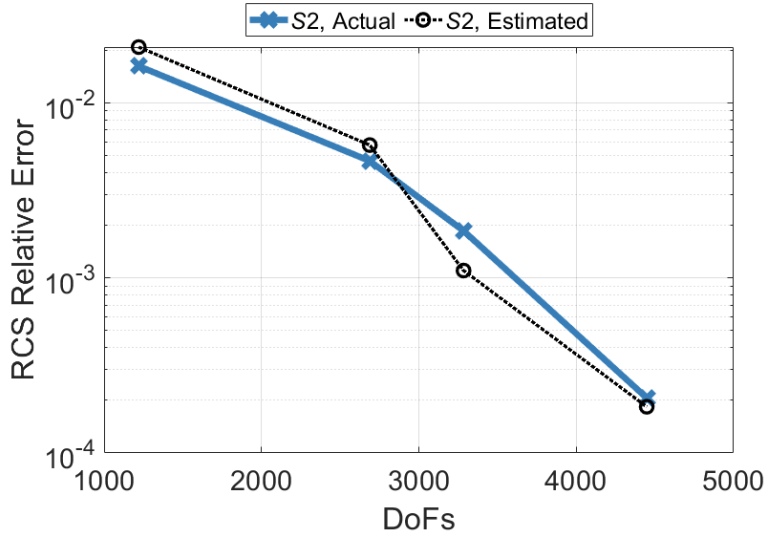


**Figure 2.10:** Convergence of the actual and estimated relative errors for the monostatic RCS of the dielectric NASA almond scatterer  $S2$ .

In Fig. 2.11(a) and Fig. 2.11(b) we depict the distribution of the expansion orders for the final discretizations for the coarsest and finest tolerances, respectively, and Fig. 2.12 similarly depicts the distribution of the expansion orders for the final discretizations of the four tolerances tested for  $S2$ . Summarizing the total cost of solving the forward and adjoint problems for each of the tolerances,

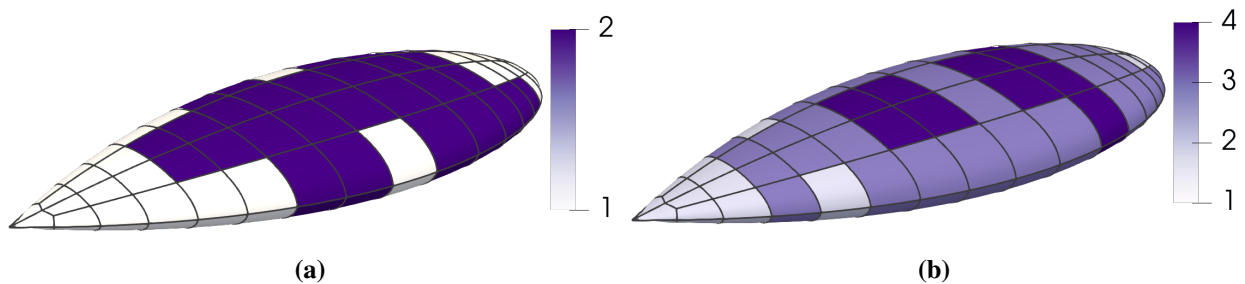


**Figure 2.11:** Illustration of the expansion orders for the coarsest and finest tolerances of the dielectric NASA almond scatterer  $S2$ . (a) The final discretization for the coarsest tolerance  $T_{S2L1}$  of  $S2$ . (b) The final discretization for the finest tolerance  $T_{S2L4}$  of  $S2$ .

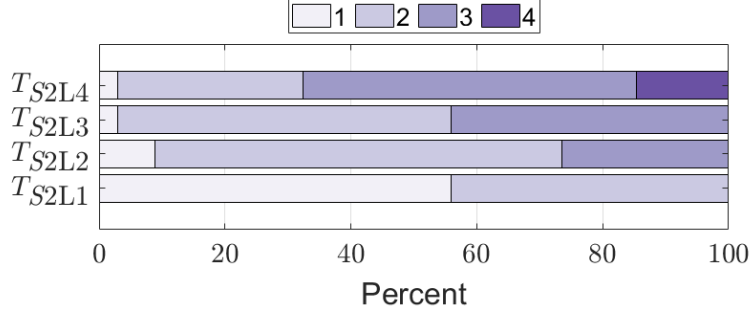


**Figure 2.12:** The distribution of expansion orders for the NASA almond scatterer  $S2$  for the four tolerances.

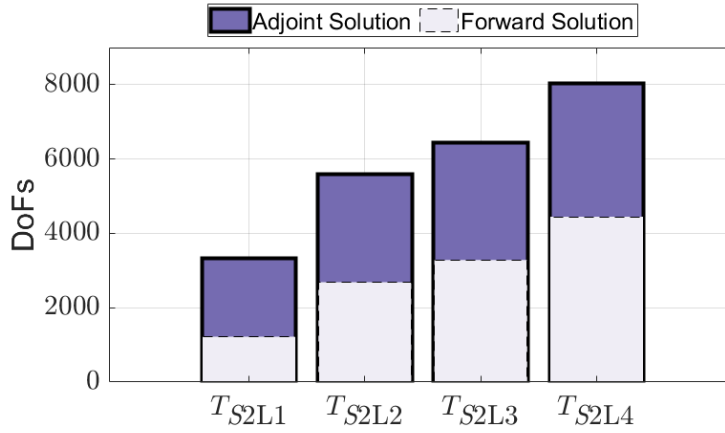


**Figure 2.13:** The total cost (in terms of the number of DoFs) of solving both the forward and adjoint problems for the NASA almond scatterer  $S2$  for the four tolerances.

Fig. 2.13 reports the number of DoFs required for the solution of the two problems by the end of the refinement procedure, exhibiting a similar trend as seen for the spherical scatterer.

For the next two examples, we explore further the capability of the proposed approach to equilibrate error contributions within a discretization and across multiple problems, such as a range of scattering angles. Specifically, we first investigate a challenging example of monostatic scattering from a square PEC plate with side lengths of  $8\lambda$ , as seen in Fig. 2.14. The discretization consists of 100 bilinear elements with first order basis functions. The monostatic scattering angle is swept from  $\theta = 0$  to  $\theta = \pi/2$  and the incident wave is polarized in the  $\theta$ -direction. For this example, the RCS changes drastically, from very large at  $\theta = 0$  to zero by  $\theta = \pi/2$ . We apply the same refinement process as before for each monostatic scattering angle separately and with a single desired relative tolerance of  $T_{\text{rel}} = 1 \times 10^{-2}$  used with (2.39) and the linearized RCS QoI by means

of (2.25) for all scattering angles. In practical applications, rather than treat each scattering direction separately, the QoIs could be clustered and combined, e.g., in the manner discussed in [24] for computing  $S$ -parameters. However, in order to specifically study the consistency and effectiveness of the refinement approach itself—in particular, the consistency of mesh equilibration—as opposed to that of the QoI clustering strategy, we consider the AMR procedure of each scattering angle independently.

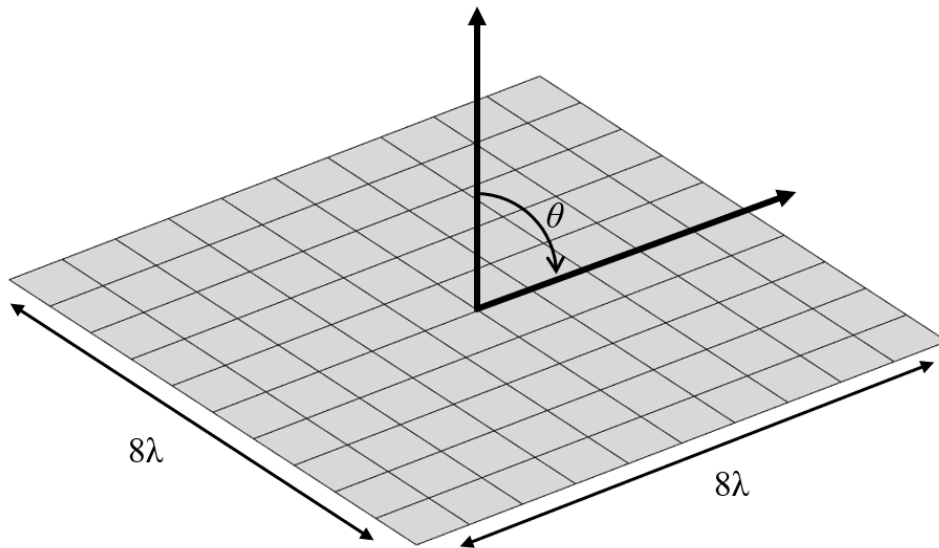


**Figure 2.14:** The starting discretization for the square plate scatterer of dimension  $8\lambda \times 8\lambda$  with 100 geometrically bilinear elements.

The monostatic RCS computations from the uniformly refined reference discretization, the very coarse starting discretization, and the adaptively refined models are depicted in Fig. 2.15. The reference data was computed using a significantly refined discretization with 18240 DoFs. The starting discretization, with a median relative error of 1.0 for the RCS QoIs, yields extremely poor accuracy, particularly for the narrow scattering angles as the QoI approaches zero, while the AMR enables high accuracy across all scattering angles, with actual and estimated median relative errors of  $1.5 \times 10^{-2}$  and  $9.8 \times 10^{-3}$ , respectively, for the RCS QoIs, further indicating the ability of (2.39)

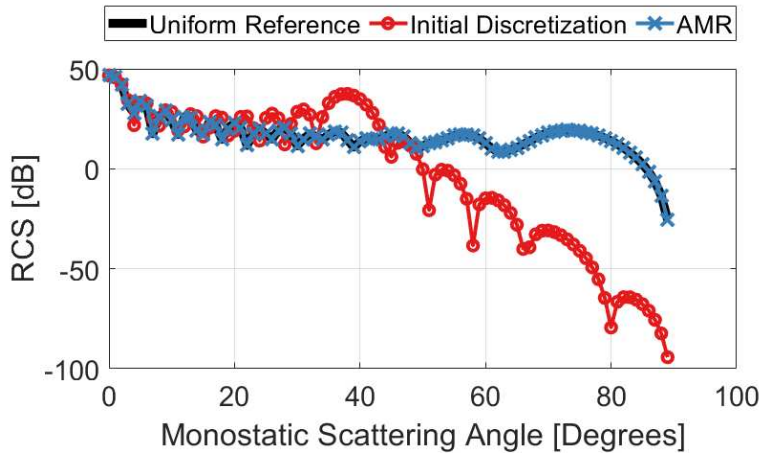


**Figure 2.15:** The RCS (in dB) computed from the starting discretization and the adaptively refined discretizations compared to that of the uniformly refined reference for the square plate scatterer over a range of monostatic scattering angles.

to determine reasonable local tolerances without additional analysis, especially given the extreme coarseness of the discretization. Note that  $\theta = 90$  is excluded, as the RCS is exactly 0.

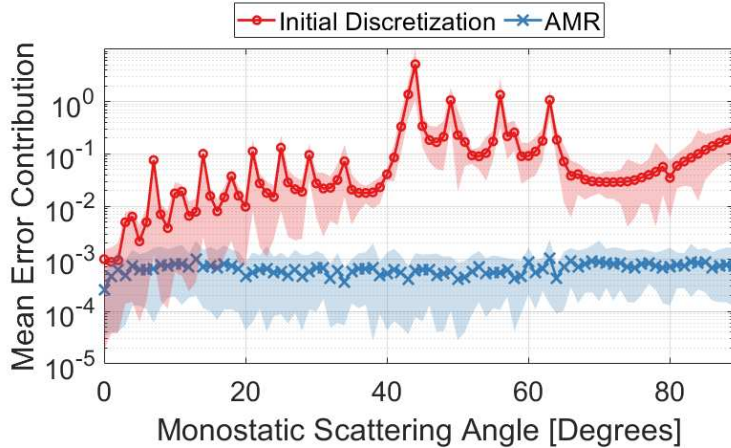


**Figure 2.16:** Mean relative error contribution estimates (normalized according to the RCS at each scattering angle) with the dispersion illustrated by bands containing two-thirds of the data versus the scattering angle for the starting and final discretizations of the AMR procedure applied to the square plate scatterer.

Now, while the RCS differs substantially across the scattering angles, the equilibration properties of the proposed approach should yield discretizations of similar characteristics given the fixed desired relative error. To evaluate this capability, we measure the sample mean and dispersion of the

relative cellwise error contribution estimates, both of which are sensitive to outliers in the data, to examine the consistency of the proposed approach over a wide-range of problems and QoIs in terms of mesh equilibration. The relative error contribution estimates are produced as in the previous examples by normalization according to the estimate of the monostatic RCS QoI, as the absolute tolerances, given the vastly different QoI magnitudes, differ substantially in value. Shown in Fig. 2.16, where the shaded bands contain two-thirds of the data and indicate the dispersion of the error contributions, the initial discretization features significant fluctuation in the mean and the dispersion of the relative error contribution estimates as the scattering angle is swept from 0 to 90 degrees. However, after AMR, the discretizations yield near constant means and standard deviations for the relative error contribution estimates. The consistency of the AMR performance to successfully match the desired accuracy and, moreover, balance the discretization even when applied to a wide range of QoIs further indicates the efficiency of the proposed approach.

Lastly, as shown in Fig. 2.17, the modeling requirements to maintain the desired estimated relative error increase substantially until  $\theta = 60$  degrees, at which point the required number of DoFs plateaus.

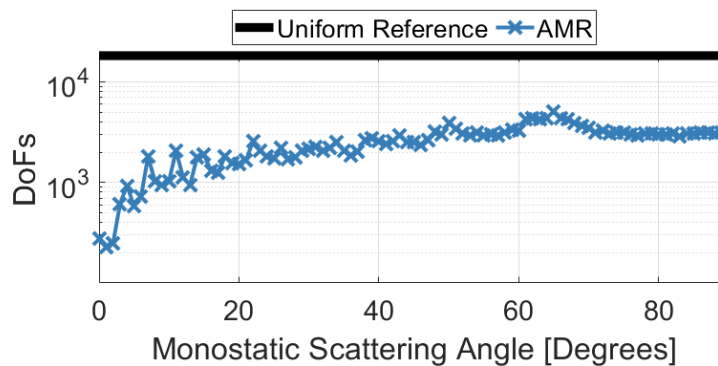


**Figure 2.17:** The number of DoFs required by the AMR procedure compared to the uniformly refined reference for the square plate scatterer over a range of monostatic scattering angles.

For the final example, we revisit the same NASA almond scatterer from before with 136 geometrically biquadratic cells for the same relative permittivity and frequency. Here, we repeat the same analysis conducted for the square plate target, now with a fixed desired relative tolerance of

$T_{\text{rel}} = 4 \times 10^{-3}$ . Once again, we estimate the error in the monostatic RCS by means of the linearized quantity (2.25). The monostatic scattering angle is swept from the back of the almond ( $\theta = -\pi/2$ ), over the top (with respect to the orientation in Fig. 2.8), to the nose of the almond ( $\theta = \pi/2$ ).

In Fig. 2.18, we again examine the monostatic RCS for the reference model, the starting discretization, and the adaptively refined discretization. The reference model is uniformly refined both in  $h$  and  $p$ , featuring 17408 DoFs. Except for  $\theta = 0$ , which is incidence on the top of the almond, the starting discretization is very poor, with extreme spikes in the computed RCS (for example, around  $\theta = -20$ ). On the other hand, the adaptively refined models closely match the reference RCS values over the entire range of scattering angles. Specifically, for the adaptively refined models, the median relative error in the RCS is  $1.9 \times 10^{-3}$  and the median estimated relative error is  $1.7 \times 10^{-3}$ .

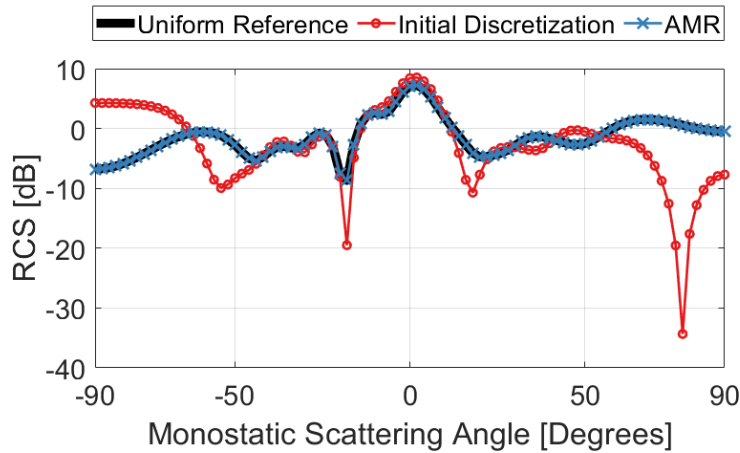


**Figure 2.18:** The RCS (in dB) computed from the starting discretization and the adaptively refined discretizations compared to that of the uniformly refined reference for the dielectric NASA almond scatterer over a range of monostatic scattering angles.

Examining the mean and dispersion of the relative error contribution estimates as in Fig. 2.19, we see substantial variation in addition to large magnitudes. Conversely, the adaptively refined discretizations are nearly uniform throughout the entire range of scattering angles once again. For the large dip in the monostatic RCS for the starting discretization around  $\theta = -20$ , the estimated

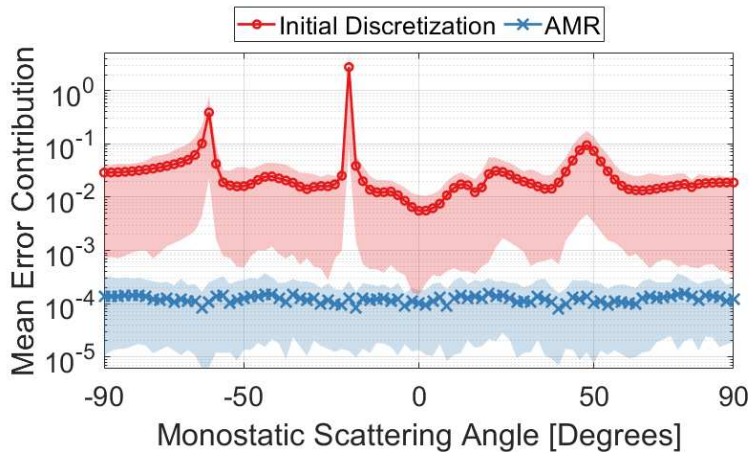


**Figure 2.19:** Mean relative error contribution estimates (normalized according to the RCS at each scattering angle) with the dispersion illustrated by bands containing two-thirds of the data versus the scattering angle for the starting and final discretizations of the AMR procedure applied to the NASA almond scatterer.

relative error approaches 100, and therefore the maximum degree of refinement, as noted in Section III, is limited to one; without this condition, a substantial degree of over-refinement would occur.

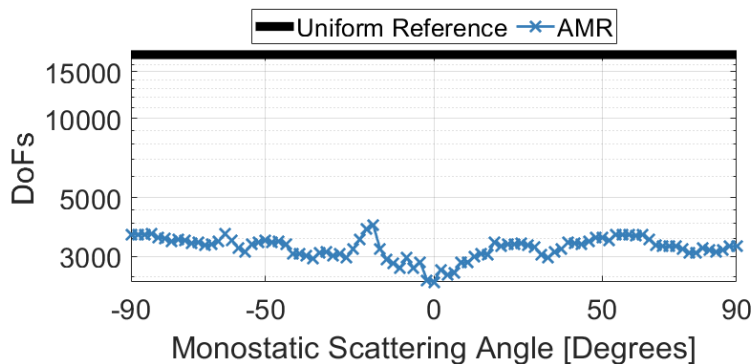


**Figure 2.20:** The number of DoFs required by the AMR procedure compared to the uniformly refined reference for the NASA almond scatterer over a range of monostatic scattering angles.

Finally, in terms of the modeling requirements, Fig. 2.20 illustrates the number of DoFs allocated by the proposed refinement procedure for each scattering angle. The requirements are approximately symmetric with scattering from the nose and back of the almond posing the most challenge overall, whereas the large spike in error that occurs near the vicinity of  $\theta = -20$  (seen in

Figs. 2.18 and 2.19 for the initial discretization) requires a substantial boost in DoFs to alleviate to satisfaction of the QoI error tolerance.

As a result, for both the square plate and the NASA almond scatterer, the proposed method is effective at equilibrating the error contribution estimates, in addition to enhancing the quality of the discretizations for computing the RCS rapidly and providing accurate error estimates.

## 2.5 Conclusion

We have demonstrated an effective approach to mesh adaption and error control for general SIE problems in the EFIE and coupled EFIE-MFIE (PMCHWT) formulations. From a given tolerance, the proposed AMR procedure rapidly refines the discretization, producing accurate and efficient resource allocations even from extremely poor quality starting discretizations.

Along with studying the dual problems for the EFIE and the EFIE-MFIE (in the PMCHWT formulation), we provide a customizable and practical scattering QoI as well as a customizable linearized RCS QoI for directly tailoring discretizations through an explicit refinement algorithm. In concert with an effective methodology for producing high quality discretizations for the MoM-SIE, the provision of error estimates (as opposed to simply error indicators) greatly increases the confidence in the accuracy of simulation results.

Furthermore, by leveraging an *a priori* error behavior heuristic and goal-oriented *a posteriori* error estimation, our approach accelerates the refinement process, disconnecting the desired accuracy from the number of refinement iterations required and, as a result, permits practical refinement to high accuracy. Moreover, in producing simulations of customizable accuracy through adjustment of a single refinement tolerance, the approach significantly reduces the need for expert-user intervention.

Finally, the proposed approach encourages equilibrated error contribution estimates, indicating the high efficiency and quality of the discretizations produced. Even when analyzing QoIs of varying magnitudes, the approach yields consistently balanced meshes. A future work will study reducing the computational expense of generating the error estimates through cost-aware approximations of the adjoint solution.

# Chapter 3

## Adaptive $hp$ -Refinement for 2-D Maxwell Eigenvalue Problems: Method and Benchmarks

### 3.1 Introduction

In the presence of singular—or generally non-smooth behavior— $p$ -refinement, the process of increasing the polynomial order of the discretization, yields only algebraic convergence; yet with a sufficiently smooth solution,  $p$ -refinement provides exponential convergence. Combined  $hp$ -refinement, however, which controls the resolution of the domain subdivision and the expansion orders, enables exponential convergence even for non-smooth solutions, unlocking significant potential for accuracy and efficiency for general problems in computational electromagnetics (CEM) and electromagnetic modeling.

The development and application of  $hp$  capable methods is of increasing interest in CEM and the broader applied mathematics community. As the demands for accuracy increase, the need for enhanced convergence, and therefore the substitution of low-order methods with higher-order alternatives, has driven significant development for practical applications in  $hp$ -refinement.

Constructing the most accurate and efficient discretization demands versatility in the model, such as non-uniform cell sizes and non-uniform expansion orders. Such versatility, however, requires adequate adaption and refinement instruction for practical and effective applications. To ensure a rapidly convergent adaptive mesh refinement (AMR) procedure, we target the discretization with goal-oriented error estimation. As opposed to standard strategies, which either specifically examine the accuracy of the solution or some property of the solution as a surrogate for the accuracy, the dual weighted residual (DWR) expression of the error enables rigorous error estimation related to quantities of interest (QoIs) computed from the solution. Furthermore, we augment the utility of the dual weighted residual by extracting the solution to an enriched solution for smoothness estimation,

which facilitates significantly improved convergence and consistency in comparison to smoothness estimation of the original forward solution itself.

Goal-oriented error estimation and adaptive refinement remains a key focus of research in the applied mathematics community. For a comprehensive overview, with a particular emphasis on duality-based approaches, see [28, 30, 57].

Mixed-order and  $hp$ -methods were introduced in [58–61], demonstrating that under proper conditions, exponential convergence with respect to the number of degrees of freedom may be achieved through a combination of  $h$ - and  $p$ -refinements. Since then, many practical studies of  $hp$  capable methods have followed, e.g., [62, 63]. Furthermore, open-source libraries such as deal.II [4, 64] have alleviated many of the practical hurdles of implementing  $hp$ -methods, yet challenges remain for effective application.

Considering the Maxwell eigenvalue problem, which is the focus of this manuscript, the success of adaptive error control approaches naturally relies on the convergence of the discrete problem to the continuous problem; rigorous analyses of this convergence through proofs of the discrete compactness property have shown the viability of  $H(\text{curl})$ -conforming Galerkin discretizations for solving the Maxwell eigenvalue problem with  $h$ -refinement procedures in [65],  $p$ -refinement procedures in [66], and combined  $hp$ -refinement procedures in [67]. Previously, [68] studied the application of  $p$ -refinement for a variety of waveguide models. For adaptive  $hp$ -refinement, an analysis of a standard residual-based error indicator and convergence was conducted in [69]. Similarly, [70, 71] studied exponential rates of convergence for cavity resonators and manual discretization refinements for smooth and singular eigenfunctions.

The predominate approach for  $hp$ -refinement of Maxwell equation problems in CEM, however, has relied mostly on multi-grid techniques, with iterative construction and comparison of a starting discretization and a globally refined (simultaneously in  $h$  and in  $p$ ) reference, such as in [13, 14, 22]. Additionally, in [23]  $hp$ -refinement was applied according to this approach for accurate S-parameter computation of waveguide discontinuities with energy-norm minimization refinement and, as an extension of the energy-norm approach, goal-oriented strategies. A similar study of goal-oriented

adaptivity for S-parameter computation was conducted in [24]. Notably, [72] proved convergence in the energy norm for a residual-based  $hp$ -refinement algorithm while also avoiding the high computational cost of the above multi-grid techniques, with applications to a variety of Maxwell equation problems in the 3-D finite element method (FEM).

Other approaches in applied mathematics have leveraged, in addition to various types of error estimation or indication, estimation of several characteristics of the discretization to determine the choice between  $h$ - and  $p$ -refinement. In [61], local error indicators were computed for a base mesh and its globally  $p$ -refined realization, with the ratio of these error indicators deciding whether to  $h$ - or  $p$ -refine. On the other hand, in [73] the smoothness of the solution was estimated from the Legendre expansion. Similarly, [74] studied the decay rate of the Fourier and Legendre series expansions to guide  $hp$ -refinement. Additionally, in [52], the Sobolev regularity of the solution was estimated from the Legendre expansion coefficients. We pursue the approach of estimating the decay rate of Legendre coefficients to generate a smoothness indicator; however, we study the smoothness of an enriched solution, rather than the original solution itself, to better target the discretization error and insufficient local smoothness.

Similar error estimates through the DWR were also applied to 1-D dielectric slab problems [27], and to accelerated  $p$ -refinement for electromagnetic scattering problems in 3-D FEM [2]. Instead, we provide a simplified form for the DWR of the Maxwell eigenvalue problem for eigenvalue QoIs and combined  $hp$ -refinement. Moreover, in this paper we explore attaining maximal accuracy through  $hp$ -refinement optimization, which, in addition to ease of use, results in exponential convergence with respect to the number of degrees of freedom.

The rest of this paper is organized as follows. Section II outlines the construction of the simplified error estimate and the  $hp$ -refinement classification procedures. Section III provides numerical examples, illustrating the strong performance of the proposed refinement procedure for the Maxwell eigenvalue problem in 2-D FEM. The examples indicate attainment of exponential rates of convergence even for eigenvalues of singular eigenfunctions. Lastly, we provide improved numerical benchmarks for a challenging waveguide model.

## 3.2 Error Estimation and Refinement Classification

### 3.2.1 Problem Formulation

We first outline the Maxwell eigenvalue problem. From the source-free Maxwell equations (in differential form), we have the following problem involving the electric field  $\mathbf{E}$ ,

$$\nabla \times (\mu_r^{-1} \nabla \times \mathbf{E}) - k_0^2 \varepsilon_r \mathbf{E} = 0 \text{ in } \Omega, \quad (3.1)$$

where  $\mu_r$  and  $\varepsilon_r$  denote the relative permeability and permittivity of the medium, respectively, and  $k_0$  denotes the free space wavenumber.

We now impose several practical constraints on the types of problems we will study. First, let us assume  $\Omega$  describes a very long, uniform perfect electrical conductor (PEC) waveguide filled with air (i.e.,  $\mu_r = 1$  and  $\varepsilon_r = 1$ ), resulting in the Dirichlet boundary condition

$$\hat{\mathbf{n}} \times \mathbf{E} = 0 \text{ on } \partial\Omega, \quad (3.2)$$

where  $\hat{\mathbf{n}}$  denotes the direction normal to the boundary.

The electric field in the waveguide varies spatially according to

$$\mathbf{E} = \mathbf{E}(x, y)e^{-\gamma z}, \quad (3.3)$$

where  $\gamma$  denotes the propagation constant, which is, in general, complex valued. Lastly, for the purposes of establishing benchmarks, we investigate only the transverse electric (TE) modes (i.e., the electric field in the axial direction is zero). The procedure can be repeated identically for transverse magnetic (TM) modes by isolating the magnetic field intensity  $\mathbf{H}$  instead. As the objective of the numerical method (and therefore the adaptivity) is the accurate and efficient computation of the cutoff-frequencies, we let  $\gamma = 0$ .

Naturally, physical eigenpairs of (3.1) correspond to those with eigenvalues greater than zero. Moreover, the eigenfunctions of positive eigenvalues automatically satisfy the divergence condition

$\nabla \cdot \mathbf{E} = 0$ . Spurious modes, which cluster exclusively around zero, may be eliminated trivially in post-processing, or the outlined approach may be augmented to a mixed finite element method to enforce the divergence condition [75].

The aforementioned problem—when reduced to a 2-D cross-section—admits the following variational form after Galerkin testing: Find  $U_{hp} = \{\mathbf{u}_{hp}, \lambda_{hp}\} \in B_{hp} \times \mathbb{R}_{>0}$  such that

$$a(\mathbf{u}_{hp}, \phi_{hp}) = \lambda_{hp} m(\mathbf{u}_{hp}, \phi_{hp}) \quad \forall \phi_{hp} \in B_{hp}, \quad (3.4)$$

with  $a(\mathbf{u}_{hp}, \phi_{hp}) = \langle \nabla_t \times \mathbf{u}_{hp}, \nabla_t \times \phi_{hp} \rangle$  (where  $\nabla_t$  represents the transversal gradient operator and  $\langle \cdot, \cdot \rangle$  denotes the standard  $L^2$  inner-product), and  $m(\mathbf{u}_{hp}, \phi_{hp}) = \langle \mathbf{u}_{hp}, \phi_{hp} \rangle$ , for a finite dimensional subspace  $B_{hp} \subset H_0(\text{curl}; \Omega)$ , where  $H_0(\text{curl}; \Omega) = \{\mathbf{u} \in H(\text{curl}; \Omega) \mid \hat{\mathbf{n}} \times \mathbf{u} = 0 \text{ on } \partial\Omega\}$  and  $\Omega \subset \mathbb{R}^2$ .

With the preceding problem constraints, we restrict our analysis to the 2-D Maxwell eigenvalue problem; nevertheless, the same approach could be applied to the 3-D Maxwell eigenvalue problem directly (assuming access to the prerequisite 3-D  $hp$ -refinement infrastructure). We note, however, that the general waveguide problem requires a more complicated variational formulation than (3.4), as described in, e.g., [68, 76].

Finally, letting  $U = \{\mathbf{u}, \lambda\} \in H_0(\text{curl}; \Omega) \times \mathbb{R}_{>0}$  denote the exact solution to the generalized eigenvalue problem, we are interested in the approximation error of the eigenvalue  $\lambda_{hp}$ , i.e., the difference

$$e_{\lambda_{hp}} := \lambda - \lambda_{hp}. \quad (3.5)$$

In the remainder of this paper, we study the adaptive control of this error through automated refinements of the underlying discretization of the forward problem.

### 3.2.2 Error Estimation

To apply the DWR procedure for the generalized eigenvalue problem in order to compute (3.5) in such a way as to guide adaptive error control, we first require an appropriate functional of the

solution that, in this case specifically, permits relating the properties of the discretization and the accuracy of an eigenvalue. However, as any scalar multiple of an eigenvector is also an eigenvector, we first assert a convenient normalization condition for the eigenfunction. Specifically, as in [77], we choose  $\mathbf{u}$  such that

$$\langle \mathbf{u}, \mathbf{u} \rangle = 1, \quad (3.6)$$

and likewise for the approximate solution  $\mathbf{u}_{hp}$ , which amounts to normalizing the eigenfunctions according to the  $L^2$ -norm.

We then take the functional

$$J[U] = \lambda \langle \mathbf{u}, \mathbf{u} \rangle = \lambda, \quad (3.7)$$

which, in concert with the normalization condition (3.6), produces the desired QoI and, as a result, we have that

$$J[U] - J[U_{hp}] = e_{\lambda_{hp}}. \quad (3.8)$$

To derive explicit expressions for the QoI error and refinement indicators, we follow the procedure in [77]. Given the above formulation and constraints, the associated dual eigenvalue problem for considering an eigenvalue QoI is identical to the forward problem, i.e., (3.4) is self-adjoint. Based on [77], we can construct a simplified form of the QoI error, namely

$$e_{\lambda_{hp}}(1 - \sigma_{hp}) = a(\mathbf{u}_{hp}, \mathbf{u} - \boldsymbol{\psi}_{hp}) - \lambda_{hp}m(\mathbf{u}_{hp}, \mathbf{u} - \boldsymbol{\psi}_{hp}), \quad (3.9)$$

for arbitrary  $\boldsymbol{\psi}_{hp} \in B_{hp}$ , with  $\sigma_{hp} = \frac{1}{2}m(\mathbf{u} - \mathbf{u}_{hp}, \mathbf{u} - \mathbf{u}_{hp})$ . While any choice of  $\boldsymbol{\psi}_{hp}$  preserves the identity (3.9) (due to Galerkin orthogonality), we choose  $\boldsymbol{\psi}_{hp} = \mathbf{\Pi}_{hp}^{\text{curl}} \mathbf{u}$ , the curl-conforming projection-based interpolation (see [78] and the references therein for a detailed description of this operator) of  $\mathbf{u}$  into the original primal finite element space, to excise the unimportant information in accumulating the error estimate, which, as opposed to other choices (e.g.,  $\boldsymbol{\psi}_{hp} = 0$ ), enhances the utility of the error indicators for refinement.

The contributions in (3.9) are accumulated separately for each cell  $K$  such that the total error is equivalent to

$$e_{\lambda_{hp}}(1 - \sigma_{hp}) = \sum_K a_K(\mathbf{u}_{hp}, \mathbf{u} - \boldsymbol{\psi}_{hp}) - \lambda_{hp} m_K(\mathbf{u}_{hp}, \mathbf{u} - \boldsymbol{\psi}_{hp}), \quad (3.10)$$

where the subscript  $K$  indicates that the integral terms  $a$  and  $m$  are evaluated just over the cell  $K$ .

To enhance the control of discretization error (particularly related to that of the approximation at the boundaries of the cells), the contributions are then separated into a cell residual and boundary residual. Integration by parts reveals that

$$a_K(\mathbf{u}, \mathbf{v}) = \int_{\Omega_K} (\nabla \times \nabla \times \mathbf{u}) \cdot \mathbf{v} \, d\Omega_K - \int_{\partial\Omega_K} (\nabla \times \mathbf{u}) \times \mathbf{v} \cdot \hat{\mathbf{n}} \, dS_K, \quad (3.11)$$

with  $\hat{\mathbf{n}}$  denoting the direction normal to the boundary as in (3.2). Note that the second integral in (3.11) is performed over the boundary of the cell (i.e., along the edges in 2-D and over the faces in 3-D).

In the case of the boundary term for a given cell, we average its contribution with the boundary terms from the neighboring cells to instead measure the jump of the tangentially directed curl  $\nabla \times \mathbf{u}_{hp}$  (which is, in general, discontinuous) weighted by  $\mathbf{u} - \boldsymbol{\psi}_{hp}$ , i.e.,

$$\begin{aligned} e_{\lambda_{hp}}(1 - \sigma_{hp}) &= \sum_K \langle \nabla \times \nabla \times \mathbf{u}_{hp}, \mathbf{u} - \boldsymbol{\psi}_{hp} \rangle_K \\ &\quad - \frac{1}{2} \left[ \langle \hat{\mathbf{n}} \times (\nabla \times \mathbf{u}_{hp}), \mathbf{u} - \boldsymbol{\psi}_{hp} \rangle_{\partial K} - \langle \hat{\mathbf{n}} \times (\nabla \times \mathbf{u}_{hp}), \mathbf{u} - \boldsymbol{\psi}_{hp} \rangle_{\partial K'} \right] \\ &\quad - \lambda_{hp} m_K(\mathbf{u}_{hp}, \mathbf{u} - \boldsymbol{\psi}_{hp}) \\ &= \sum_K \tilde{\eta}_K, \end{aligned} \quad (3.12)$$

where  $K'$  indicates the collection of cells that share an edge (in 2-D) or a face (in 3-D) with cell  $K$ , and  $\tilde{\eta}_K$  denotes the final error contribution estimate associated with cell  $K$ . In implementation, this procedure amounts to traversing each cell to compute the volume terms and a separate traversal of every face/edge, accumulating the contributions from the cells on either side as described in (3.12). Furthermore, note that for the combination of two boundary terms as in (3.12), the curl of the forward solution must be evaluated on both sides of an edge (or a face in 3-D); however, given its tangential continuity,  $\mathbf{u} - \boldsymbol{\psi}_{hp}$  may be evaluated just once for each edge/face.

Finally, in addition to error indicators for refinement, the summation of the signed contributions  $\tilde{\eta}_K$  from each cell  $K$  provides a correction term—by means of (9)—to improve the accuracy of the approximate QoI computed from the forward problem. For the purposes of refinement in the remainder of the paper, we define the refinement *indicator*  $\eta_K$  to be the absolute value of the error contribution estimate  $\tilde{\eta}_K$ , i.e.,

$$\eta_K := |\tilde{\eta}_K|, \quad (3.13)$$

for each cell  $K$ .

In the above expressions, we assume access to the exact solution  $\mathbf{u}$ . In general, however, we must substitute an approximation of  $\mathbf{u}$ . Galerkin orthogonality precludes taking  $\mathbf{u}_{hp}$  as the approximation for  $\mathbf{u}$ , as it would imply an estimate of zero error. Instead, we replace  $\mathbf{u}$  with a finite dimensional approximation  $\mathbf{u}_{hp^+} \in B_{hp^+}$ , where  $B_{hp^+}$  denotes the enriched finite element space generated by increasing the expansion orders of each cell by one in the discretization of the forward problem (3.4). While very effective for error estimation, alternative approaches, such as those discussed in [28], can provide improvements in efficiency.

### 3.2.3 Refinement Classification

Following the above error estimation procedure yields a collection of cells cataloged according to their estimated contributions to the QoI error. To approach optimally equilibrated discretizations during the convergence procedure, we develop a variant of the selection scheme introduced in [79]. Since the primary concern is that the local regularity of the solution prevents accelerated convergence, for the purposes of designing the marking scheme, let us temporarily assume we  $h$ -refine only. Furthermore, in this manuscript we consider only isotropic refinements in  $h$  and  $p$ , while additional efficiency and versatility may be unlocked through anisotropic refinements (though with greater requirements of the underlying refinement and coarsening infrastructure) [80].

We consider the marking procedure as a two-step process, with an independent refinement step, followed by a coarsening step. We have, therefore, in concert with the trinary marking decision, three groups of cells to treat: the  $m$  cells to refine, the  $l$  cells to coarsen, and the remaining cells

which are left unchanged. Under one  $h$ -refinement step, the number of new cells introduced when refining the  $m$  cells with the largest error contribution estimates is

$$(2^d - 1) m, \quad (3.14)$$

where  $d$  denotes the geometric dimension of the discretization. Grouping cells into the set of refined cells,  $R$ , and unrefined cells,  $\tilde{R}$ , the total predicted error  $\eta$  after an  $h$ -refinement step is

$$\eta = \sum_{K \in R} 2^{-\alpha(K)} \eta_K + \sum_{K \in \tilde{R}} \eta_K, \quad (3.15)$$

where  $\alpha(K)$  denotes the predicted rate of convergence on cell  $K$ , which we take as the degree of the polynomial basis on the cell (i.e., ignoring the regularity in the convergence condition), with an associated refinement indicator  $\eta_K$  produced from (3.12) by means of (3.13). From [79], the refinement procedure must weight not just the error reduction, but also the increased cost and, as a result, should minimize the following objective function

$$\begin{aligned} J_{refine}(m) = & N_{\alpha_1}^{\alpha_1/d} \left( \sum_{\substack{K \in R(m) \\ \alpha(K)=\alpha_1}} 2^{-\alpha_1} \eta_K + \sum_{\substack{K \in \tilde{R}(m) \\ \alpha(K)=\alpha_1}} \eta_K \right) + \cdots \\ & + N_{\alpha_j}^{\alpha_j/d} \left( \sum_{\substack{K \in R(m) \\ \alpha(K)=\alpha_j}} 2^{-\alpha_j} \eta_K + \sum_{\substack{K \in \tilde{R}(m) \\ \alpha(K)=\alpha_j}} \eta_K \right), \end{aligned} \quad (3.16)$$

where, to track the increased cost of refining higher-order cells,  $N_{\alpha_i}$  counts the number of cells (after refinement) that have a polynomial basis of degree  $\alpha_i$ , for  $i = 1, \dots, j$ , where  $j$  denotes the number of different expansion orders in the discretization. The optimal  $m$  cells with the largest error contributions may be found through simple enumeration. Hence, for marking cells for refinement, the approach ensures the best choice—according to the objective function (3.16)—for the worst-case scenario ( $h$ -refinement only).

In the interest of practicality, we enforce the coarsening as a succession to refinement (rather than a parallel operation). Analogous to the case of refinement, the coarsening procedure should seek to minimize the predicted error increase while maximizing the computational savings. In tandem with this goal, any coarsening procedure should accelerate error homogenization to improve discretization quality and efficiency. With the set  $R$  (the refined cells) fixed, we consider reclassifying the unrefined cells for coarsening by determining the  $l$  cells with the smallest error contribution estimates that minimize

$$\begin{aligned}
J_{coarsen}(l) = & N_{\alpha_1}^{\alpha_1/d} \left( \sum_{\substack{K \in \hat{R}(l) \\ \alpha(K)=\alpha_1}} \eta_K + \sum_{\substack{K \in \hat{R}(l) \\ \alpha(K)=\alpha_1}} 2^{\alpha_1} \eta_K \right) + \dots \\
& + N_{\alpha_j}^{\alpha_j/d} \left( \sum_{\substack{K \in \hat{R}(l) \\ \alpha(K)=\alpha_j}} \eta_K + \sum_{\substack{K \in \hat{R}(l) \\ \alpha(K)=\alpha_j}} 2^{\alpha_j} \eta_K \right),
\end{aligned} \tag{3.17}$$

where  $\hat{R}$  indicates the set of cells marked for coarsening.

However, independent of the underlying marking strategy, we have a collection of cells marked for refinement or coarsening. In the case of pure  $h$ - or pure  $p$ -refinement, the error indicators provide sufficient refinement information. In the case of combined  $hp$ -refinement, however, we must decide *what* to refine and *how* to refine, namely to decide whether to apply  $h$ - or  $p$ -adaptivity.

Since the theoretical conditions for exponential convergence require a sufficient degree of local regularity [53, 54], we estimate the local smoothness on marked cells to decide  $h$ - over  $p$ -refinement and isolate non-smooth behavior. We estimate the smoothness both from the enriched and standard forward solutions, which we extract from the DWR error estimation process; i.e., we leverage the two finite dimensional Galerkin approximate solutions (where one belongs to an enriched space) computed as part of evaluating the eigenvalue QoI error estimate in (3.12). While estimating directly from the standard forward solution provides effective refinement classification information, estimating the smoothness of the enriched solution better targets our principal objective: eliminating discretization error where the solution yields inadequate accuracy. We adopt the approach demonstrated in [74] for estimating the decay of the Legendre expansion. The enriched

field, keeping in mind the necessity of approximating the exact solution, is simply  $\mathbf{u}_{hp^+} \in B_{hp^+}$ . Hence, for each shape function  $\hat{\varphi}_j$  on every cell  $K$ , we have an associated coefficient  $e_{j,K}$ . The Legendre coefficients of the  $w$ -component (e.g., the  $x$ - or  $y$ -components) of this local field are then computed from

$$c_{\xi,K,w} = \sum_j \hat{L}_{i(\xi)j,w} a_{j,K} \quad (3.18)$$

$$\hat{L}_{i(\xi)j,w} = \left( \prod_{n \in \xi} \frac{2n+1}{2} \right) \int_{\hat{K}} \hat{\varphi}_{j,w}(\hat{\mathbf{x}}) P_{\xi}(\hat{\mathbf{x}}) J_K d\hat{\mathbf{x}}, \quad (3.19)$$

where  $\hat{\varphi}_{j,w}$  indicates that the  $w$ -component of the vectorial shape function  $\hat{\varphi}_j$  is taken,  $J_K$  denotes the Jacobian determinant of the mapping between the reference cell and its image  $K$ , and the integrals in the transformation matrix  $\hat{L}_{ij,w}$  are computed over the reference cell  $\hat{K}$ , where  $P_{\xi}$  denotes the tensor-product Legendre polynomial of the multi-index  $\xi \in \mathbb{N}_0^d$ . The decay rate of each field component is estimated independently through linear regression of the logarithm of the coefficients, with the smallest predicted decay rate (which suggests lower regularity) propagated forward for refinement classification as we consider only isotropic refinements in this work. With support for anisotropic  $hp$ -refinements, the individual decay rates may be applied to instruct directional refinements instead. Of course, the expansion must be truncated to a finite number of terms. Hence, from [74, 81], we perform linear regression on the set of (modified) coefficients

$$C_{K,w} = \left\{ \log \left( \max_{\substack{\xi \\ \|\hat{\xi}\|_1 = \|\xi\|_1}} |c_{\xi,K,w}| \right) : \|\xi\|_1 \leq p_K \right\}, \quad (3.20)$$

where  $p_K$  denotes the degree of the polynomial basis on cell  $K$  of the enriched discretization.

As in error estimation and marking cells for refinement or coarsening, each cell must be classified for  $h$ - or  $p$ -refinement. Analogously to the relative marking of cells, typical strategies employed rely on a relative threshold for determination, i.e., taking a threshold  $T$  such that

$$T(\kappa) = \kappa \eta_{max} + (1 - \kappa) \eta_{min}, \quad (3.21)$$

where  $\kappa \in [0, 1]$  and  $\eta_{max}$  and  $\eta_{min}$  denote, respectively, the maximum and minimum decay rates. This form of the refinement classifier indicates a strong dependence on  $\kappa$ , with  $\kappa = 0$  implying  $p$ -refinement only and  $\kappa = 1$  implying  $h$ -refinement only, and therefore the need for a judicious choice. Typically, in the absence of prior information,  $\kappa = 1/2$  is chosen; however, depending on the problem, we might expect additional value for  $p$ -refinement as opposed to  $h$ , and vice versa, motivating the need for an alternative classifier.

Instead, we take the approach as in [73], with a fixed threshold, such as  $T = 1.0$ . We find that when applying the Legendre smoothness indicator,  $T = 1.0$  underestimates the smoothness, driving, therefore, less  $p$ -refinement than would be profitable. As a result, in the numerical results section, we take  $T = 0.85$  as a more aggressive (in terms of  $p$ -refinement) yet still widely applicable tolerance. Naturally, a threshold too strongly weighted towards  $p$ -refinement or towards  $h$ -refinement will, in either case, inhibit the ability of the adaption algorithm to yield exponential convergence.

We summarize the adaptive error control procedure as follows:

1. For each cell, compute error contribution estimates and refinement indicators by means of (3.12) and (3.13)
2. Of the  $N$  total cells in the discretization, identify the  $m$  cells that should be refined, the  $l$  cells to coarsen, and the  $N - m - l$  cells that are left unchanged
  - (a) Set  $m$  to be the minimizer of the objective function (3.16)
  - (b) With  $m$  now fixed, set  $l$  to be the minimizer of the objective function (3.17)
3. With the cells classified for refinement and coarsening, for each cell  $K$ , estimate the smoothness of the field to determine whether the cell should be  $h$ - or  $p$ -refined/reduced
  - (a) For  $\mathbf{u}_{hp+}$  on cell  $K$ , associate the coefficients  $e_{j,K}$  with each shape function  $\hat{\varphi}_j$  on cell  $K$  in the enriched finite element space
  - (b) Estimate the decay rate  $C_{K,w}$  of the coefficients of the Legendre expansion using (3.20) for each component  $w$  of the field (i.e., the vectorial directions)

- i. For isotropic refinements, take the only the minimum decay rate over the individual vectorial components of the field
- (c) If cell  $K$  is marked for refinement, then  $p$ -refine for a decay rate above some threshold  $T$  (e.g.,  $T = 1.0$  or  $T = 0.85$ ); otherwise,  $h$ -refine
- (d) If cell  $K$  is marked for coarsening, then coarsen in  $p$  for a decay rate below  $T$ ; otherwise, coarsen in  $h$

Note that for the actual execution of refinement or coarsening of the discretization, additional requirements that depend on the underlying  $hp$ -refinement implementation—such as maintenance of a 1-irregularity rule (i.e., only one hanging node per edge after an  $h$ -refinement)—require additional care, for example, as discussed in [82].

Finally, to analyze the effectiveness of proposed refinement, specifically for 2-D problems, we note that the relative error of the approximate eigenvalue is bounded by

$$C e^{-b(\text{NDoFs})^\kappa}, \quad (3.22)$$

where NDoFs signifies the number of degrees of freedom,  $C$ ,  $b$ ,  $\kappa > 0$  are constants independent of the NDoFs [70]. In 2-D, when the solution is smooth,  $\kappa = 1/2$ , otherwise  $\kappa = 1/3$ . A linear trend of the relative error (in log-scale) with respect to  $(\text{NDoFs})^\kappa$  indicates exponential convergence, permitting a convenient method to visualize the performance of an adaptive strategy.

### 3.3 Numerical Results

We now apply the proposed adaptive mesh refinement procedure to a challenging model problem in the form of an L-shaped waveguide originally proposed by [83]. The implementation is based on the finite element library deal.II [4,64], leveraging a continuous Galerkin approach with higher order Nédélec cells of the first kind [84] with support for non-uniform expansion orders and hanging-nodes (1-irregular) [63]. Visualization of the discretizations and the eigenfunctions was performed using VisIt [85].

From [83, 86] we have a collection of numerical reference eigenvalues to compare the accuracy and effectiveness of the proposed approach to adaptive  $hp$ -refinement in CEM.

In all examples, the starting geometric discretization is that of Fig. 3.1. The error in a given eigenvalue is computed from (3.12), and the cells to refine and coarsen are chosen through successive minimization of the objective functions (3.16) and (3.17) under the assumption of the need to  $h$ -refine only. The marking strategy is then followed by recategorization of the refinement and coarsening to the isotropic  $h$  and  $p$  decisions according to the smoothness estimation outlined in Section II.

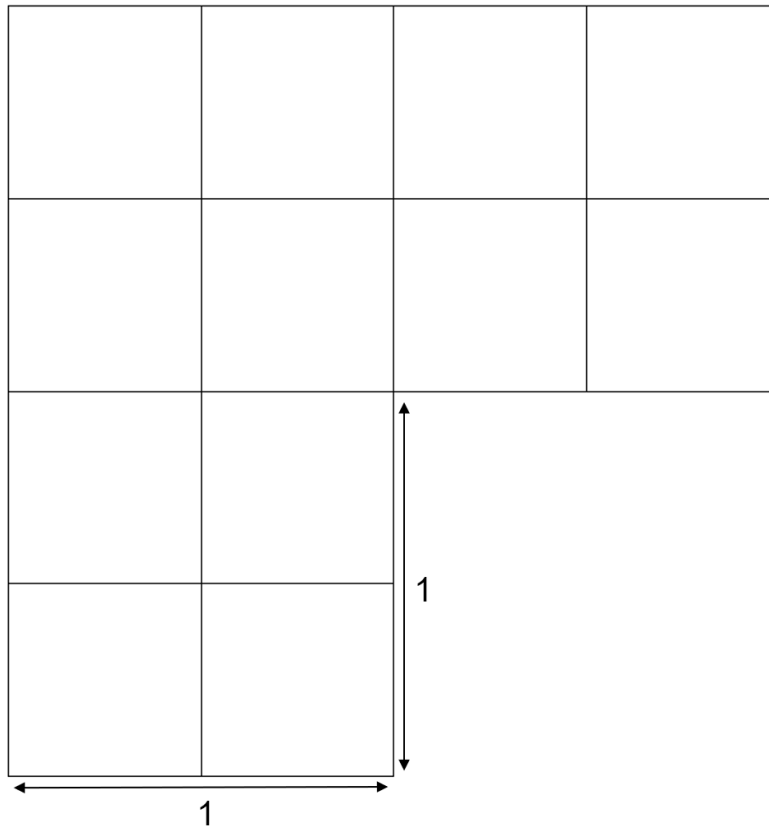


**Figure 3.1:** The starting discretization for the L-shaped waveguide.

We focus our study on the smallest nine eigenvalues, the first five of which have been examined previously in [83, 86].

The first nine eigenpairs separate equally into three classes: those with strongly singular eigenfunctions, seen in Fig. 3.2; non-smooth eigenfunctions, seen in Fig. 3.3; and globally smooth eigenfunctions, seen in Fig. 3.4. The 1st, 6th, and 8th eigenpairs have highly singular eigenfunctions; the 2nd, 5th, and 9th eigenfunctions, while not unbounded, exhibit non-smooth behavior near the re-entrant corner of the domain; and the 3rd, 4th, and 7th eigenfunctions are globally smooth. Furthermore, note that in each case, the curl of the eigenfunction, which is purely in the axial direction, is non-zero. For the non-smooth and singular eigenfunctions, the curl is highly sensitive in a neighborhood about the re-entrant corner (i.e., small perturbations in position result in relatively large changes in the magnitude of the curl), though approximately zero at the re-entrant corner itself. The L-shaped waveguide, therefore, provides an excellent test case for the analysis of  $hp$ -refinement methods in CEM, providing a range of solution types to evaluate efficacy and efficiency.

For each class of eigenpair, we demonstrate the effectiveness of the proposed approach for  $hp$ -refinement. Based on the numerical experiments in [2], which indicated that accurate results typically require at least cubic or quartic polynomial bases, we initialize the primal discretization with uniformly cubic basis functions for the singular class and quartic for the non-smooth and smooth classes; however, the polynomial order may be reduced to unity through coarsening (i.e., the degree of coarsening in  $p$  is unrestricted), and the maximal expansion order for the primal discretization is limited to twelve. Note that initialization with linear basis functions is undesirable due to inadequate information for smoothness estimation [74]. For illustration of the advantage of estimation of the enriched solution smoothness over the standard forward solution smoothness, we include results from both strategies. We denote the enriched solution smoothness and the standard forward solution smoothness AMR strategies by E-AMR and S-AMR, respectively. The values of the eigenvalues include the correction term provided by solving the discrete problem with the enriched discretization as required in the DWR and the increased cost (in terms of the number of degrees of freedom) to compute this quantity.

Starting with the singular class of eigenfunctions, the field magnitude is characterized by a singularity at the re-entrant corner and, depending on the mode, variation elsewhere in the domain.

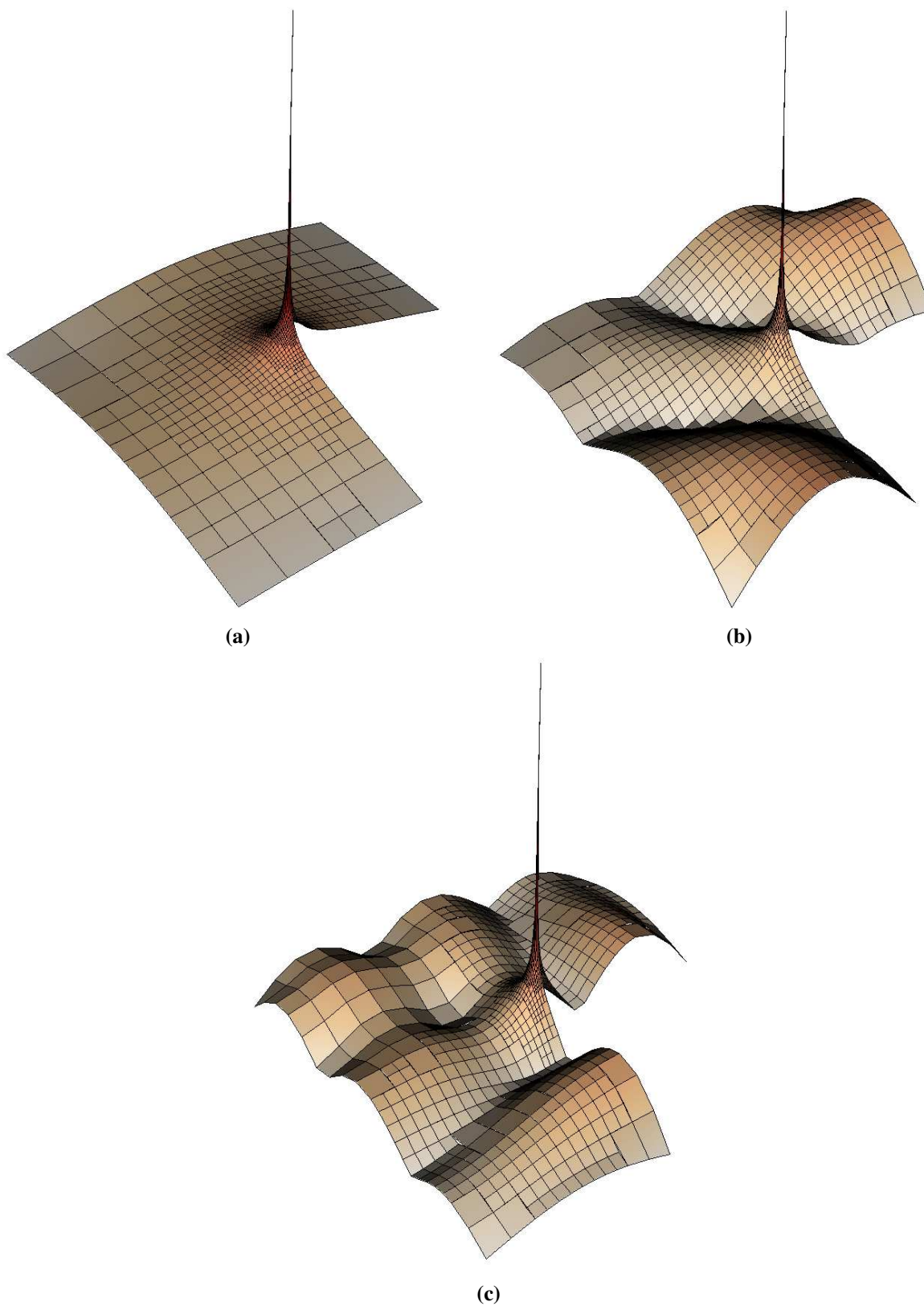


**Figure 3.2:** Field magnitudes for the singular eigenfunctions. (a) The 1st eigenfunction. (b) The 6th eigenfunction. (c) The 8th eigenfunction.

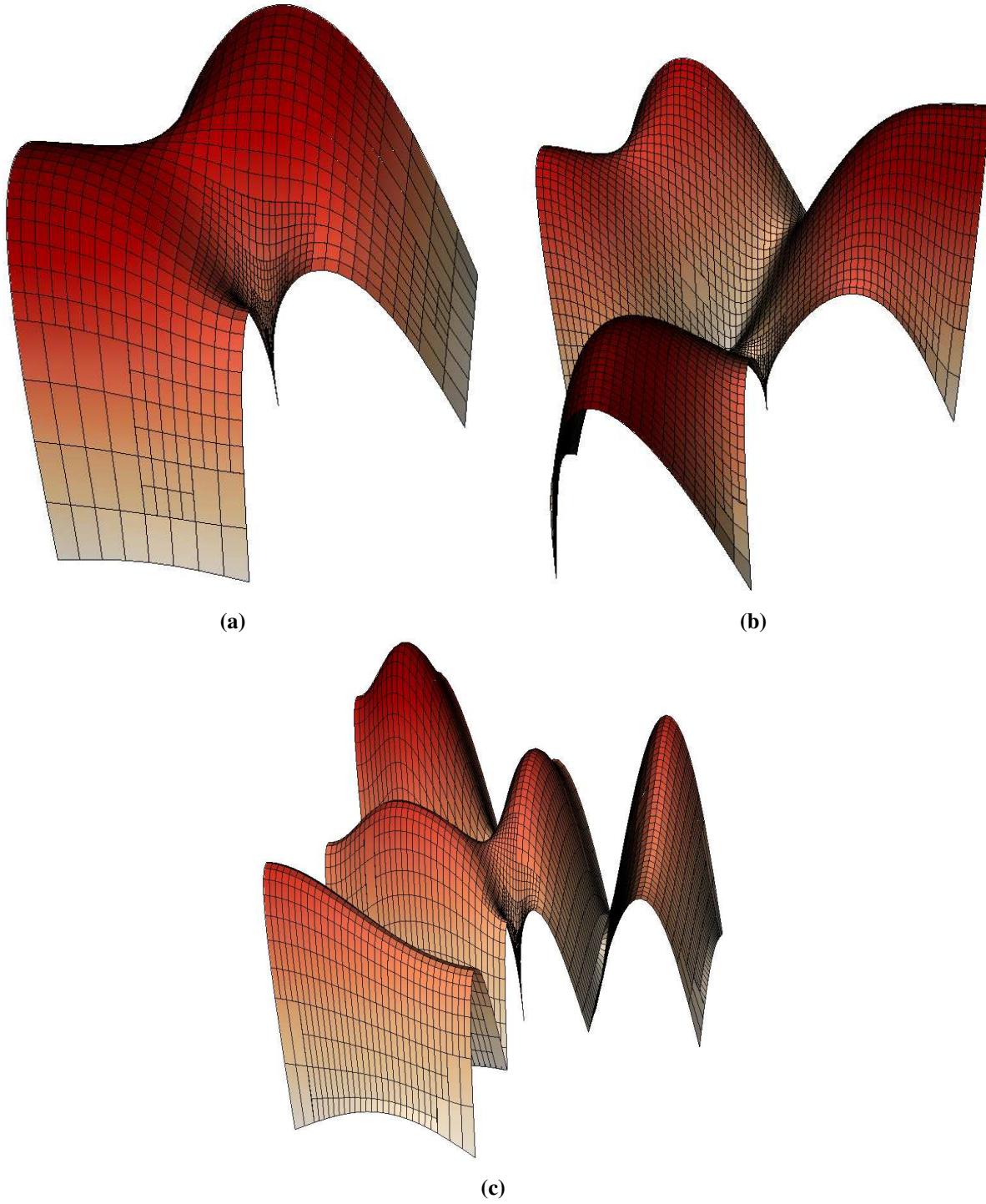


**Figure 3.3:** Field magnitudes for the non-smooth eigenfunctions. (a) The 2nd eigenfunction. (b) The 5th eigenfunction. (c) The 9th eigenfunction.

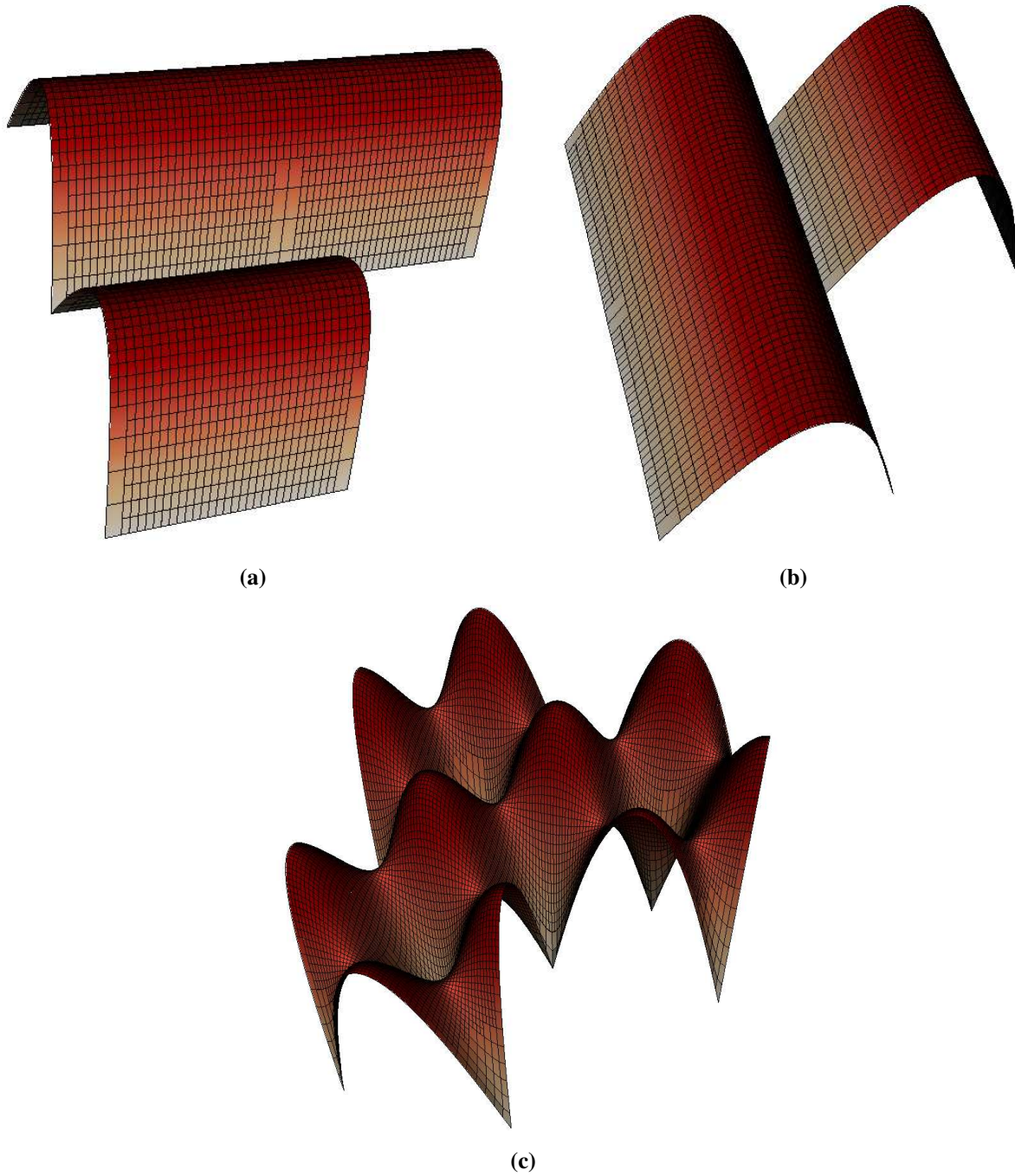


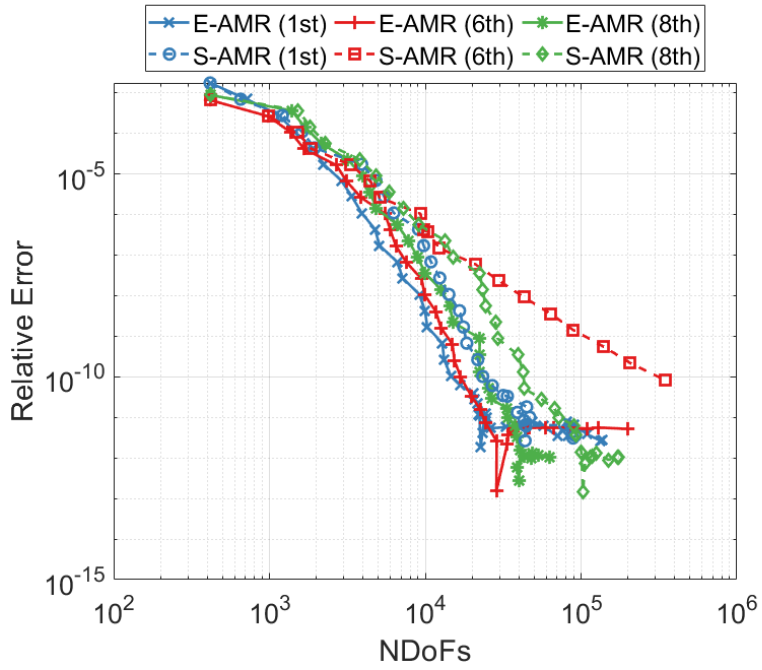
**Figure 3.4:** Field magnitudes for the globally smooth eigenfunctions. (a) The 3rd eigenfunction. (b) The 4th eigenfunction. (c) The 7th eigenfunction.

While the neighborhood around the re-entrant corner significantly influences the accuracy of the eigenvalues, it is not solely responsible; this presents tremendous challenge in highly accurate computations, and, in particular, prevents standard error indication strategies (e.g., the gradient-jump methods) from attaining maximum accuracy as the adaptivity will over-emphasize the re-entrant corner (to the neglect of the remainder of the discretization).

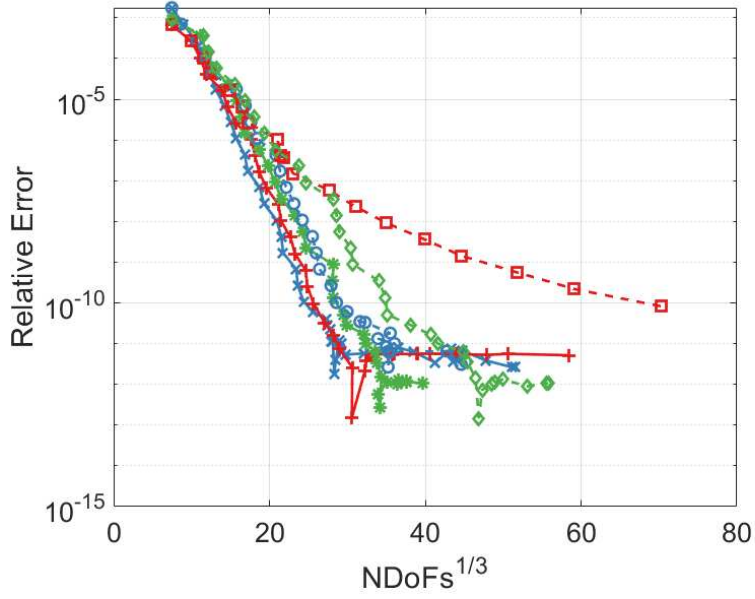
Fig. 3.5 depicts the results of the E-AMR and S-AMR procedures applied to the eigenpairs with singular eigenfunctions. For the convergence of the 1st eigenvalue, the presented E-AMR scheme provides significant improvements in efficiency, providing a 10 to 100 times improvement in the accuracy for the same number of DoFs compared to S-AMR. With the horizontal axis in Fig. 3.5(b) scaled with respect to  $(N\text{DoFs})^{1/3}$ , we see that E-AMR and S-AMR yield exponential convergence. Both approaches match the accuracy (12 digits) of the most accurate benchmark available [86], which required 59459 degrees of freedom. The E-AMR approach, however, required only 20364 DoFs to attain the same accuracy.

Moving on to the 6th eigenpair, we again see in Fig. 3.5 the advantage of the E-AMR approach. As no previous benchmark exists for this eigenpair, the reference value is taken from the invariant digits of the refinement process. With E-AMR, the convergence of the eigenvalue is nearly identical to the 1st eigenvalue, even with the increased fluctuation throughout the domain. S-AMR, however, is severely limited by estimating the smoothness from the standard forward solution, achieving only algebraic convergence with respect to the number of degrees of freedom for this eigenvalue, as seen in Fig. 3.5(b). Fully leveraging the information provided by the DWR process, as in the E-AMR strategy, produces exponential convergence without difficulty. Moreover, estimating the smoothness from the enriched solution produces discretizations several orders of magnitude more efficient. The E-AMR strategy reaches 12 digits of accuracy for this eigenvalue.

The 8th eigenpair produces similar results as to the 1st eigenpair; however, as the eigenpair itself is much more demanding in terms of computational resources, 38966 DoFs are required for 12 digits of precision using the proposed E-AMR strategy, whereas S-AMR requires nearly three times



(a)



(b)

**Figure 3.5:** Convergence of the eigenvalues of the singular eigenfunctions with respect to the number of degrees of freedom. (a) Double logarithmic representation. (b) log-cube-root representation.

as many degrees of freedom for the same accuracy at 105840 DoFs. Furthermore, while E-AMR yields consistent exponential convergence, S-AMR performs less consistently.

The first converged discretizations produced by E-AMR for the eigenvalues belonging to the singular class are shown in Fig. 3.6. For the 1st eigenvalue, shown in Fig. 3.6(a), the minimum and maximum expansion orders attained were three and nine, respectively. For the 6th eigenvalue, shown in Fig. 3.6(b), the minimum and maximum expansion orders were four and twelve, while the minimum and maximum for the 8th eigenpair, from Fig. 3.6(c), was two and twelve. All three problems resulted in a significant increase in cell density in the neighborhood of the singularity and large expansion orders where the eigenfunctions vary smoothly.

Repeating the same process but for the class of non-smooth eigenfunctions, we see similar performance. In each case the reference value for computing the relative error is taken from the invariant digits of the refinement process. As seen in Fig. 3.7, the E-AMR procedure achieves exponential convergence for each of the eigenvalues. S-AMR, while also yielding exponential convergence (apart from the early iterations for the 9th eigenvalue), is once again 10 to 100 times less efficient than the proposed E-AMR approach. Each approach, however, can provide 14 digits of accuracy. When examining the convergence of the 9th eigenvalue with S-AMR, estimating the smoothness of the standard forward solution results in substantially more  $h$ -refinement than necessary, reducing the efficiency in comparison to E-AMR.

Illustrated in Fig. 3.8, the first converged discretizations convey the increased rate of  $p$ -refinement possible for the non-smooth eigenfunctions in comparison to the singular eigenfunctions. The discretizations, however, still exhibit increased cell density at the re-entrant corner, given the sharp field behavior as seen in Fig. 3.3. The 9th eigenvalue requires a high level of refinement globally, while the 2nd and 5th eigenvalues converge much earlier in terms of the number of degrees of freedom.

Finally, in the case of the three globally smooth eigenpairs, the eigenvalues converge to multiples of  $\pi^2$ . The 3rd and 4th eigenpairs, as identified by [83], share an eigenvalue of  $\pi^2$  and the proposed E-AMR procedure indicates that the 7th eigenpair has an eigenvalue of  $2\pi^2$ .

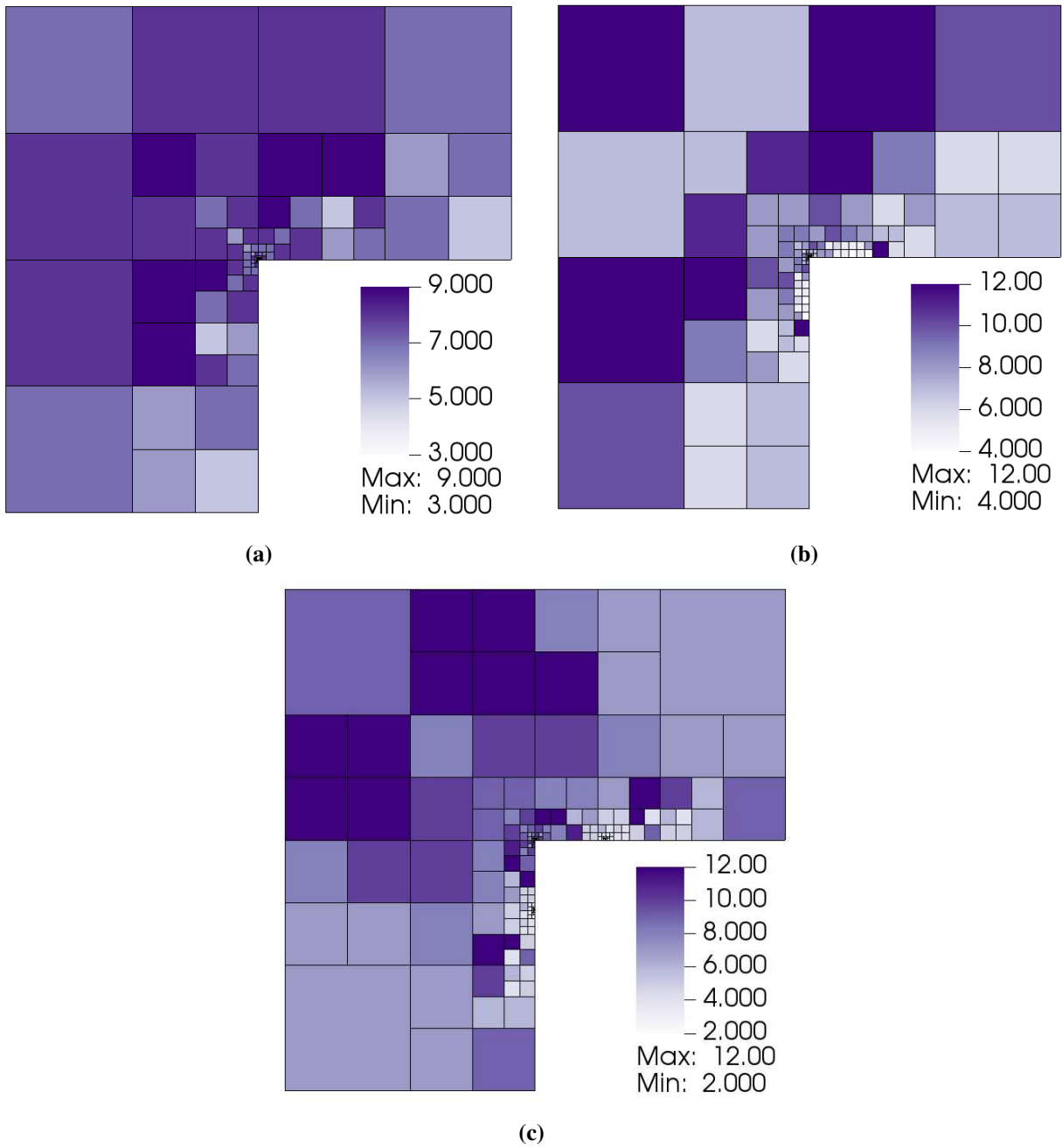


**Figure 3.6:** The first converged discretizations for the singular eigenpairs. (a) The 1st eigenpair. (b) The 6th eigenpair. (c) The 8th eigenpair.

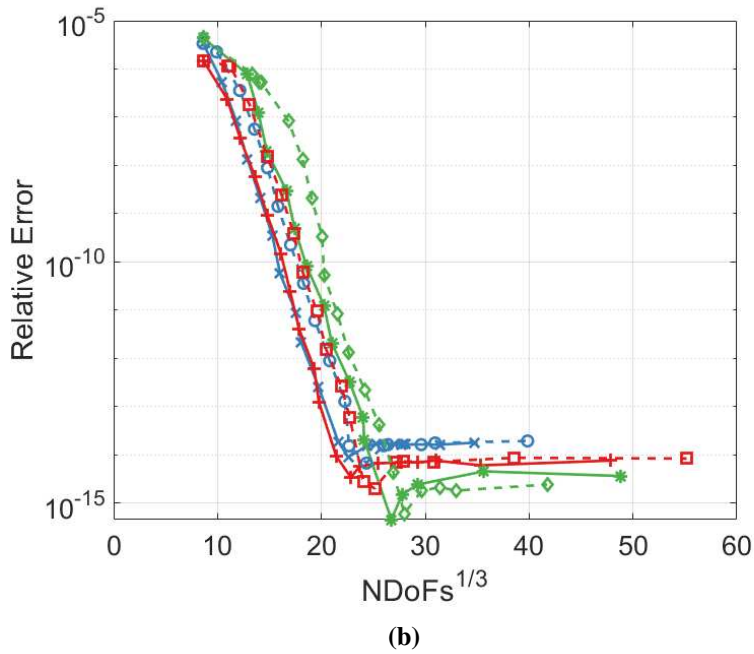
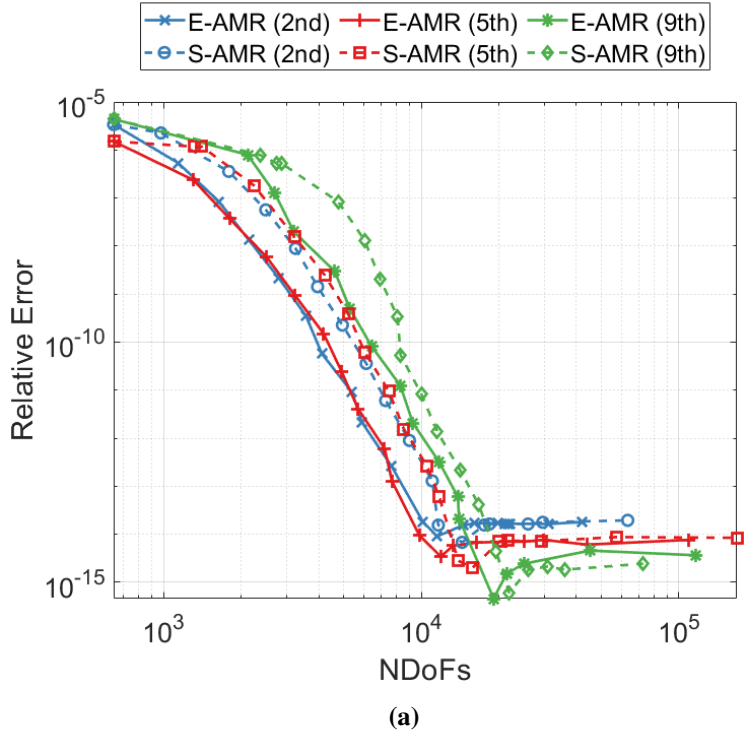


**Figure 3.7:** Convergence of the eigenvalues of the non-smooth eigenfunctions with respect to the number of degrees of freedom. (a) Double logarithmic representation. (b) log-cube-root representation.

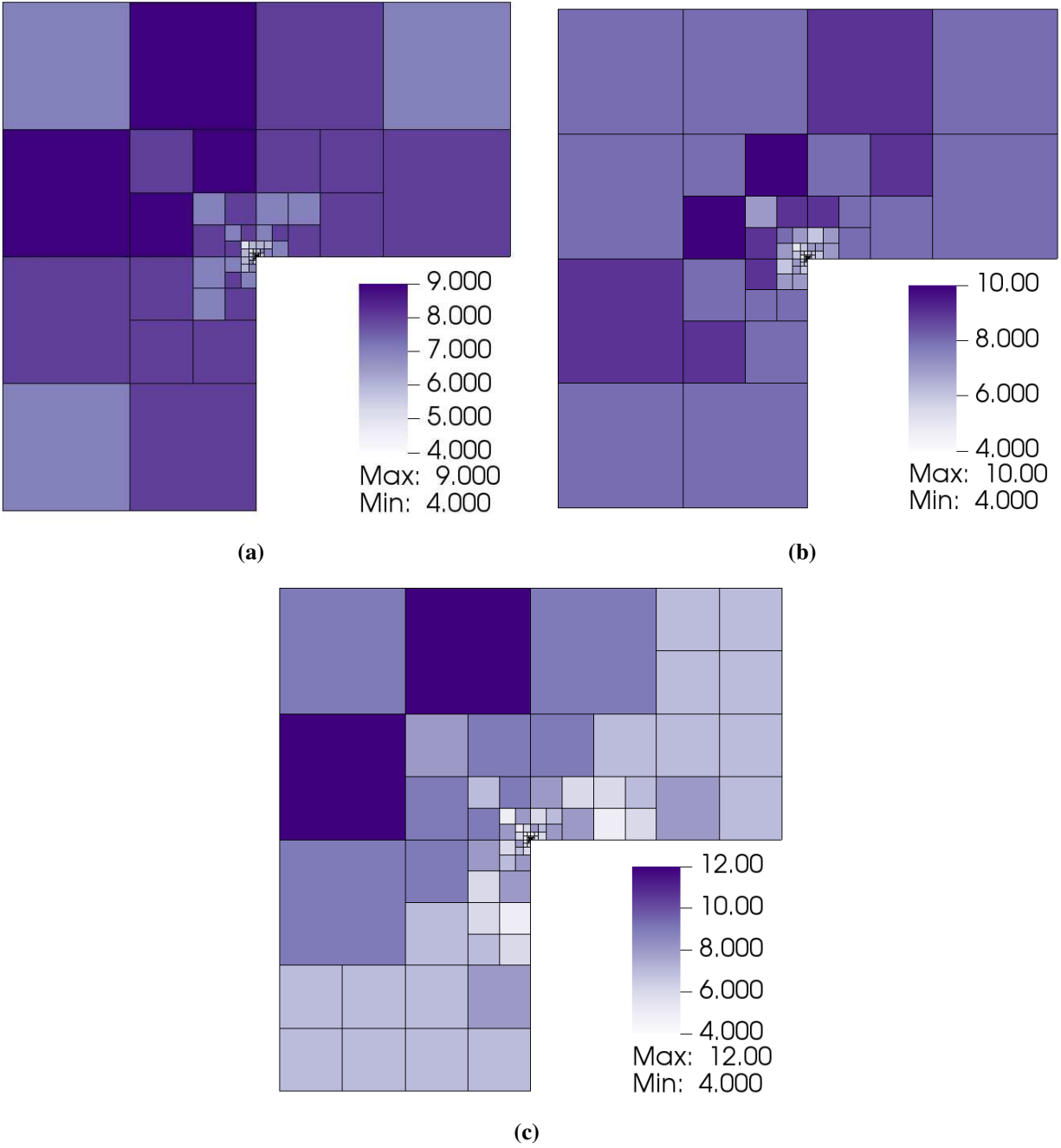
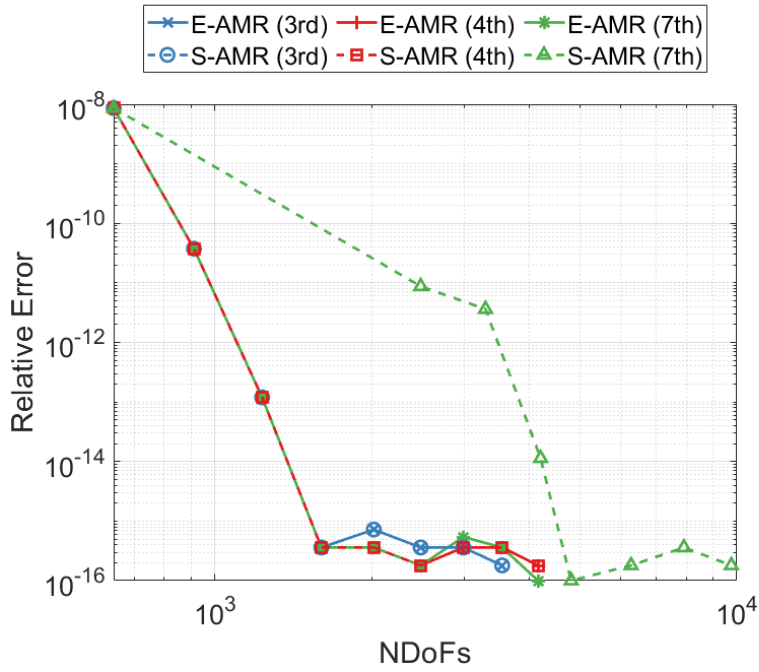
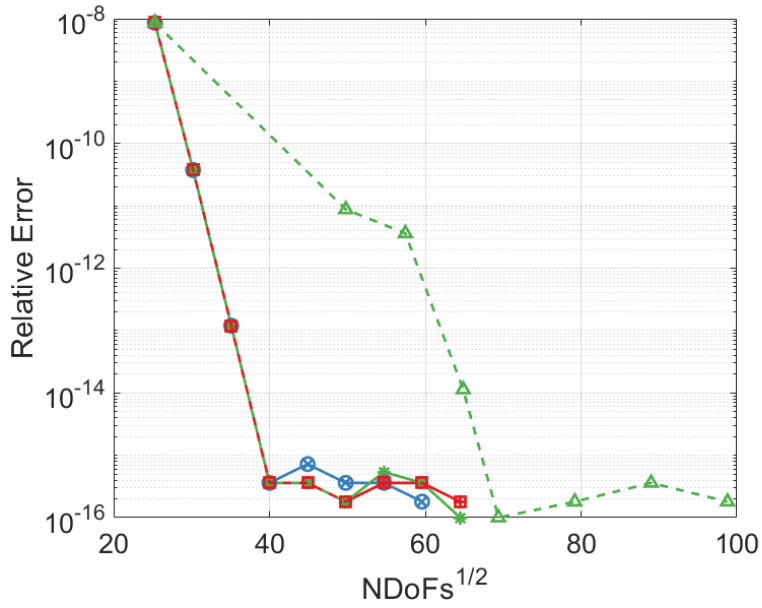


**Figure 3.8:** The first converged discretizations for the non-smooth eigenpairs. (a) The 2nd eigenpair. (b) The 5th eigenpair. (c) The 9th eigenpair.



(a)



(b)

**Figure 3.9:** Convergence of the eigenvalues of the smooth eigenfunctions with respect to the number of degrees of freedom. (a) Double logarithmic representation. (b) log-square-root representation.

Unsurprisingly, given the simplicity of the eigenfunctions depicted in Fig. 3.4(a)-(b), the E-AMR and S-AMR approaches perform identically for the 3rd and 4th eigenpairs, as depicted in Fig. 3.9, since both successfully detect the global smoothness and only  $p$ -refine each iteration. Note that for this case, the horizontal axis in Fig.3.9(b) is scaled with  $\text{NDoFs}^{1/2}$  as the solutions are globally smooth and therefore  $\kappa = 1/2$  in (3.22).

In contrast, the 7th eigenpair, which, like the 3rd and 4th eigenpairs, has a globally smooth eigenfunction, causes difficulty for the S-AMR strategy due to the rapid variations present in the mode, as shown in Fig. 3.4(c). E-AMR, on the other hand, once again drives only  $p$ -refinements each iteration for this eigenpair.

While the E-AMR yields exponential convergence and, most importantly, only conducts  $p$ -refinement (the ideal choice for the problem), estimating the smoothness from the standard forward solution as in S-AMR results in ineffectual  $h$ -refinements and fewer  $p$ -refinements in the early iterations, limiting the performance.

As the discretizations produced by E-AMR only require global  $p$ -refinement of the starting discretization (Fig. 3.1) at each iteration, and no  $h$ -refinements are performed to attain maximal accuracy, an illustration is omitted for the smooth eigenfunction class. For each of the three eigenpairs in this class, convergence within machine precision for the eigenvalue computed using E-AMR to the reference value occurs for a uniform expansion order of  $p = 7$  throughout the discretization.

Overall, the proposed adaption mechanism facilitates rapid convergence of the eigenvalue QoIs. By estimating the smoothness of the higher-order, enriched solution, as in the E-AMR approach, exponential convergence was achieved across all examples tested. S-AMR, on the other hand, by estimating the smoothness of the lower-order forward solution, yielded acceptable, though less efficient, results for lower-order modes and demonstrated inconsistencies for the higher-order modes. As the enriched solution is available from the computation of the DWR, E-AMR provides a significant enhancement of discretization quality without incurring substantial additional computational expenses in the refinement process.

Finally, in Table I we summarize the computed eigenvalues to expand upon existing benchmarks. The benchmark values were extracted from the E-AMR refinement process and each eigenvalue has an estimate of the number of accurate digits (i.e., the digits which are invariant under further refinements), as well as the previous best accuracy from available benchmarks (if applicable).

**Table 3.1:** Benchmark Eigenvalues Computed With E-AMR.

Eigenvalue	Digits	Previous Digits [86]
1.47562182397	12	12
3.5340313667880	14	12
$\pi^2$	-	-
$\pi^2$	-	-
11.389479397947	14	12
12.5723873200	12	N/A
$2\pi^2$	-	N/A
21.4247335393	12	N/A
23.344371957137	14	N/A

### 3.4 Conclusion

We have demonstrated the capability to adaptively refine from coarse initial discretizations to highly accurate eigenvalue computations through a combination of goal-orientated error estimation, intelligent refinement selection, and smoothness indication.

We applied the proposed approach to the first nine eigenpairs of a challenging waveguide model, including three singular, three non-smooth, and three smooth eigenfunctions. The E-AMR procedure, which utilizes the smoothness of the enriched solution available through the goal-oriented error estimation step, achieved exponential convergence with respect to the number of degrees of freedom, permitting rapid refinement even for eigenpairs with singular eigenfunctions. In contrast,

estimation of the smoothness of the standard forward solution in the S-AMR approach resulted in a large reduction in efficiency across all examples. Moreover, while achieving exponential convergence for lower-order modes, for the higher-order modes, S-AMR overestimated the need for  $h$ -refinement, resulting in reduced convergence rates.

In addition to confirming and improving the results of previous numerical benchmarks, we expanded the current set of benchmarks with higher-order modes for more challenging test cases. Furthermore, the extensions to higher-order modes illustrate the importance of including rapid (yet smooth) variation in the testing and design of  $hp$ -refinement algorithms.

Future works will study alternative approaches to the  $hp$ -decision to reduce sensitivity to the choice of the smoothness tolerance and, most importantly, to facilitate efficient applications with arbitrarily shaped cells.

## Chapter 4

# Adjoint Sensitivity Analysis for Uncertain Material Parameters in Frequency Domain 3-D FEM

### 4.1 Introduction

With traditional uncertainty propagation and gradient approximation techniques, analysis of variation among many parameters involves substantial computation times. Direct evaluation of gradients, for example, presents significant challenges to computational efficiency and feasibility, especially for high dimensional parameter spaces. Likewise, classical Monte Carlo (MC) methods are unsuitable for problems with many unknowns (e.g., complex geometries or high frequency), requiring many solutions of the forward problem.

Through the solution of a dual (or adjoint) problem, however, gradient approximation can be greatly expedited. The adjoint approach links the forward problem to the quantity of interest (QoI), permitting efficient analysis of changes in QoIs due to perturbations in model parameters, including estimation of the local sensitivity of the output QoI to random variation. Leveraging the adjoint information, the higher-order parameter sampling (HOPS) technique enables a highly efficient method to generate accurate gradients and updated QoIs, relying only on the original forward solve and its corresponding adjoint solution [29, 87–89]. Avoiding the need to directly evaluate gradients with respect to each parameter, this updated approach therefore yields vast improvements in computational efficiency. For uncertain parameters, e.g., describing the spatial heterogeneity of material properties in a scatterer, HOPS drastically reduces the computation time required to quantify uncertainties, achieving the accuracy of lengthy MC simulations with just a handful of solves. Since most practical problems require optimization and analysis of many parameters, this adjoint informed approach yields significant computational efficiency improvements over traditional methods.

In computational electromagnetics (CEM), adjoint analysis has been studied primarily for optimization in finite-difference time-domain (FDTD) methods, as in [31–36, 90–95], rather than the simultaneous sensitivity and uncertainty quantification for the frequency domain finite element method (FEM) as in this work.

Adjoint analysis in CEM has also been successfully applied to inverse problems [96, 97]. The paper [98], in particular, leverages empirical interpolation methods assisted by duality for model reduction to expedite the analysis of uncertain conductivity in low frequency electromagnetics. Earlier works have also demonstrated the advantage of adjoint analysis for goal-oriented refinement, such as in [26, 99, 100].

Overall, however, adjoint analysis has remained relatively uncommon in CEM, while in other fields like computational fluid dynamics, such methods have seen significant research and development, such as for error estimation [28, 30, 57, 101–104]. Additionally, previous work outside CEM has shown the viability of adjoint analysis for improving the analysis of unlikely events [105], dimensionality reduction [106], and accelerating optimization [107].

For determining the impact of uncertainty, traditional gradient estimation techniques have been applied to radar cross-section measurements for rough surfaces [108]. The use of automatic differentiation for studying small perturbations has also provided an efficient means to analyze parameter uncertainty in CEM [109].

Aside from standard MC methods as in [110–112] for rough surfaces, much of the remaining existing work in CEM regarding uncertainty quantification and uncertain parameters relies on solving stochastic partial differential equations (PDEs), typically using finite difference methods, such as for low-dimensional material parameter uncertainty [113, 114] or geometric variation [115]. Notably, polynomial chaos expansion (PCE) methods were applied in FDTD for analyzing variation in the scattered electric field for a dielectric sphere scatterer with an uncertain relative permittivity and radius [116].

In FEM, similar stochastic PDE methods were applied to analyze surface roughness effects in 2-D for scattered field quantities [117], and transmission coefficient variation due to material

uncertainty [118, 119]. While highly efficient for low-dimensional uncertainty, these stochastic methods, in addition to requiring significant modifications to a deterministic solver, are unsuitable for moderate and high dimensional uncertainty. Typically, variants of the stochastic spectral Galerkin approach (including intrusive PCE) require sophisticated preconditioners and computationally intensive model reduction to render the problem tractable [120]. Our approach, however, requires only the solution of deterministic PDEs, with the uncertainty introduced externally to the core solver, and naturally excels for high dimensional uncertainty.

On the other hand, nonintrusive uncertainty quantification methods for FEM, such as those based on stochastic collocation, seek to address the computational difficulties of solving stochastic PDEs. Stochastic collocation, which enables computing the coefficients for nonintrusive PCE, inherits a significant limitation in the dimension of the uncertainty due to the rapid growth in collocation points, particularly with standard tensor-product evaluations; however, sparse grid sampling (e.g., Smolyak sparse grids) alleviates, but does not eliminate, this difficulty [121, 122]. In [123], for example, nonintrusive PCE assisted by an adaptive Smolyak sparse grid algorithm provided a significant reduction in the computational load for analyzing dosimetry with uncertain tissue material parameters in 2-D FEM. A similar approach for 3-D FEM combined with basis reduction was applied for dosimetry applications in [124]. Moreover, Smolyak sparse grids and PCE were applied to construct stochastic impedance matrices for accurate analysis of composite cylindrical scatterers with geometric uncertainty in 2-D FEM [125]. Recently, a stochastic testing method with Smolyak sparse grids for nonintrusive PCE was studied for analysis of uniform waveguide dispersion with uncertain material parameters [126]. However, the approach in [126] requires Gaussian random variables, whereas our approach has no such limitation. Additionally, stochastic collocation techniques were applied to a variety of problems in FEM, as well as the method of moments (MoM) and hybrid methods, for low dimensional geometric and material uncertainty [127].

In contrast to these methods, our approach provides a distinct emphasis on the effect of uncertainty on the scattering QoI computed from the finite element solution. As an analog to goal-oriented

error estimation and adaptive refinement, in which we address the particular regions contributing most significantly to the QoI, the proposed approach emphasizes the effect of uncertainty on the QoI specifically, permitting a substantial enhancement of efficiency, even when compared to sparse grid techniques, while retaining the convenience of other nonintrusive methods.

Recently, adjoint analysis applied to 1-D FEM demonstrated accurate QoI response estimation using the adjoint solution for univariate and deterministic scattering problems for dielectric slabs [27]. This work, in contrast, extends the findings of [2, 128–131] to 3-D FEM uncertainty quantification and outcome prediction, and provides an efficient and effective methodology for propagating uncertainty in the solution of PDEs in CEM, with application to high dimensional parameter spaces.

Lastly, we provide derivations and explicit constructions for accelerating the analysis of uncertain parameters for a customizable and practical scattered electric field QoI through adjoint sensitivity and HOPS, showing vast improvements over traditional MC methods.

The rest of this paper is organized as follows. Section II outlines the formulation of the adjoint problem and develops the HOPS methodology for 3-D FEM. Section III provides numerical examples, illustrating rapid HOPS QoI prediction and probability density estimation for low- to high-dimensional parameter spaces in scattering problems. The examples demonstrate extremely significant computational savings for QoI estimation compared to the MC method with nearly identical accuracy.

## 4.2 The Adjoint: Derivations and Estimators

### 4.2.1 The Adjoint Problem

We first summarize the components of the standard forward problem, referred to as the double-curl wave equation:

$$\nabla \times \mu_r^{-1} \nabla \times \mathbf{E}^{sc} - k_0^2 \varepsilon_r \mathbf{E}^{sc} = -\nabla \times \mu_r^{-1} \nabla \times \mathbf{E}^{inc} + k_0^2 \varepsilon_r \mathbf{E}^{inc}, \quad (4.1)$$

with  $\mu_r$  and  $\varepsilon_r$  representing the relative permeability and permittivity tensors, respectively, and  $k_0$  denoting the free space wave number, and which we denote as

$$\mathcal{L}\mathbf{E}^{sc} = \mathbf{G}. \quad (4.2)$$

The domain is truncated by introducing an air layer and a perfectly matched layer (PML) [132], where the entire domain is surrounded by perfect electrical conductor (PEC). The solution is found using the double higher-order FEM [133–135]; however, the procedure is unchanged for low-order methods.

The adjoint operator  $\mathcal{L}^*$  is defined by the Lagrange identity [29]:

$$\langle \mathcal{L}\mathbf{u}, \mathbf{v} \rangle = \langle \mathbf{u}, \mathcal{L}^*\mathbf{v} \rangle, \quad (4.3)$$

where  $\langle \cdot, \cdot \rangle$  denotes the standard  $L^2$  inner-product. As in [2], the adjoint operator satisfies

$$\mathcal{L}^*\mathbf{v} = \nabla \times (\mu_r^{-1})^* \nabla \times \mathbf{v} - k_0^2 \varepsilon_r^* \mathbf{v}. \quad (4.4)$$

The adjoint operator therefore has the form of the forward operator, with the complex conjugate or conjugate transpose (in the case of tensor materials) of the model parameters.

Analogously to choosing different excitations for the forward problem, we select a suitable adjoint problem to relate the forward problem to a specific QoI. We therefore consider an arbitrary linear (or linearized) functional  $J$  of the forward solution  $\mathbf{E}^{sc}$  of  $\mathcal{L}\mathbf{E}^{sc} = \mathbf{G}$ , such that for all  $\mathbf{E}^{sc}$  the QoI is

$$J[\mathbf{E}^{sc}] = \langle \mathbf{E}^{sc}, \mathbf{p} \rangle, \quad (4.5)$$

where the Riesz representation theorem [136] guarantees the existence of  $\mathbf{p}$ , and (4.5) determines the choice for the adjoint excitation:

$$\mathcal{L}^*\mathbf{v} = \mathbf{p}. \quad (4.6)$$

Solving for additional QoIs simply requires solving the adjoint problem with new right-hand sides. Conveniently, the Galerkin approximate adjoint solution does not require an explicit form for  $\mathbf{p}$ . Rather, only the ability to evaluate (4.5) is necessary [2].

For a practical choice of a QoI, we examine scattered electric field quantities as in [2]. Starting from the Kirchhoff integral and isolating the  $\mathbf{w}$ -component of the electric field to produce a scalar QoI, we have the following functional of the finite element solution,

$$J[\mathbf{E}^{sc}] = \oint_S \mathbf{w} \cdot [\hat{\mathbf{n}} \times (\nabla \times \mathbf{E}^{sc}) + jk_0(\hat{\mathbf{n}} \times \mathbf{E}^{sc} \times \mathbf{i}_r)] e^{jk_0 \mathbf{i}_r \cdot \mathbf{r}'} dS. \quad (4.7)$$

### 4.2.2 Handling Parameter Uncertainty with HOPS

Consider, for example, a model problem with ideal parameters (i.e., a perfectly smooth surface, exact conductivity and permittivity, etc.). For this reference problem, we would like to understand the impact of variations in the construction and the constituent parameters on the output QoI. Classically, the estimation of uncertain effects applies the MC method, in which each sample of the uncertain parameters incurs the additional cost of solving the perturbed forward problem. While MC simulations are simple to implement and can produce accurate results, the computation time demanded by the method is simply not sustainable for a moderate number of samples or for problems with many unknowns.

In the presence of parameter uncertainty, however, we can also exploit the utility of the adjoint solution to expedite sensitivity analysis, rapidly generating approximate gradient information for any number of uncertain parameters which perturb a deterministic PDE. HOPS requires just the solutions to the adjoint and forward problems at the deterministic references to generate gradient information for any number of uncertain parameters which perturb the construction of the model. This enables efficient generation of sensitivity information for many parameters, especially compared to classical gradient approximation approaches (e.g., first-order finite difference) which require numerous solutions of the forward problem.

By leveraging the adjoint solution with HOPS, we can construct an accurate QoI response from a small set of deterministic reference solutions, thereby addressing the efficiency problem which hampers the utility of traditional approaches. Random samples of parameters are propagated

through the piecewise-linear response built using HOPS, avoiding full model solves. Additionally, considering that the adjoint solution might already be available from adaptive mesh refinement, HOPS provides significant potential for computational savings in uncertainty quantification.

To derive the form of the HOPS estimate, we proceed analogously to [29, 87]:

We begin with the deterministic reference forward problem (4.2)

$$\mathcal{L}\mathbf{E}^{ref} = \mathbf{G}, \quad (4.8)$$

and the corresponding reference adjoint problem,

$$\mathcal{L}^*\mathbf{v} = \mathbf{p}. \quad (4.9)$$

Perturbing some component  $\kappa$  of the reference problem with the random variable  $\eta$  produces the adjusted equation

$$\tilde{\mathcal{L}}\tilde{\mathbf{E}}^{sc} = \tilde{\mathbf{G}}, \quad (4.10)$$

noting that

$$\tilde{\mathcal{L}} = \mathcal{L} + \delta_{\eta-\kappa}\mathcal{L}, \quad (4.11)$$

$$\tilde{\mathbf{G}} = \mathbf{G} + \delta_{\eta-\kappa}\mathbf{G}, \quad (4.12)$$

and

$$\tilde{\mathbf{E}}^{sc} = \mathbf{E}^{ref} + \delta_{\eta-\kappa}\mathbf{E}^{ref}, \quad (4.13)$$

where  $\delta_{\eta-\kappa}$  signifies the effects of the perturbation.

To reveal the dependence of the perturbed QoI on the reference QoI, we first expand (4.10) through substitution of (4.11) and (4.12) and take the inner-product with the adjoint solution  $\mathbf{v}$ , which shows:

$$\langle \tilde{\mathcal{L}}\tilde{\mathbf{E}}^{sc}, \mathbf{v} \rangle + \langle \delta_{\eta-\kappa}\mathcal{L}\tilde{\mathbf{E}}^{sc}, \mathbf{v} \rangle = \langle \mathbf{G}, \mathbf{v} \rangle + \langle \delta_{\eta-\kappa}\mathbf{G}, \mathbf{v} \rangle. \quad (4.14)$$

Applying the Lagrange identity to the first terms on the left- and right-hand sides and rearranging, we have

$$\langle \tilde{\mathbf{E}}^{sc}, \mathbf{p} \rangle = \langle \mathbf{E}^{ref}, \mathbf{p} \rangle + \langle \delta_{\eta-\kappa} \mathbf{G} - \delta_{\eta-\kappa} \mathcal{L} \tilde{\mathbf{E}}^{sc}, \mathbf{v} \rangle. \quad (4.15)$$

Under the assumption that the perturbations are relatively small (i.e.,  $\tilde{\mathbf{E}}^{sc} \approx \mathbf{E}^{ref}$ ),

$$\langle \tilde{\mathbf{E}}^{sc}, \mathbf{p} \rangle \approx \langle \mathbf{E}^{ref}, \mathbf{p} \rangle + \langle \delta_{\eta-\kappa} \mathbf{G} - \delta_{\eta-\kappa} \mathcal{L} \mathbf{E}^{ref}, \mathbf{v} \rangle. \quad (4.16)$$

Finally, applying the definition of the QoI, we have

$$J[\tilde{\mathbf{E}}^{sc}] \approx J[\mathbf{E}^{ref}] + \langle \delta_{\eta-\kappa} \mathbf{G} - \delta_{\eta-\kappa} \mathcal{L} \mathbf{E}^{ref}, \mathbf{v} \rangle, \quad (4.17)$$

which describes how, with the reference QoI and adjoint solution, we can compute an updated QoI for the perturbed problem.

For a specific realization of a HOPS-based estimate for an updated QoI, let  $\kappa$  denote the reference relative permittivity, and  $\eta$  the perturbed relative permittivity of a scatterer. To build the estimate (4.17), we have

$$D_{\varepsilon_r} \mathbf{G} = k_0^2 \mathbf{E}^{inc}, \quad (4.18)$$

and

$$D_{\varepsilon_r} \mathcal{L} \mathbf{E}^{ref} = -k_0^2 \mathbf{E}^{ref}. \quad (4.19)$$

Hence, we approximate the QoI for the perturbed model by

$$J[\tilde{\mathbf{E}}^{sc}] \approx J[\mathbf{E}^{ref}] + k_0^2 \langle (\mathbf{E}^{inc} + \mathbf{E}^{ref})(\eta - \kappa), \mathbf{v} \rangle, \quad (4.20)$$

where  $\eta$  and  $\kappa$  denote, respectively, the perturbed and reference permittivities of the scatterer.

Substituting in the approximate Galerkin solution to the deterministic reference forward problem  $\mathbf{E}^{ref} = \sum_i \alpha_i \mathbf{f}_i$  and the reference adjoint solution  $\mathbf{v} = \sum_j \beta_j \mathbf{f}_j$  and expressing the inner-product in integral form, (4.20) becomes

$$J[\tilde{\mathbf{E}}^{sc}] \approx J[\mathbf{E}^{ref}] + k_0^2 \sum_i \sum_j \alpha_i \beta_j^* \int_{\Omega} (\eta - \kappa) \mathbf{f}_i \cdot \mathbf{f}_j d\Omega + k_0^2 \sum_j \beta_j^* \int_{\Omega} (\eta - \kappa) \mathbf{E}^{inc} \cdot \mathbf{f}_j d\Omega. \quad (4.21)$$

We may analyze multiple parameters varied simultaneously, in which case  $D_{\varepsilon_r} \mathbf{G}$  and  $D_{\varepsilon_r} \mathcal{L} \mathbf{E}^{ref}$  are matrix quantities, and  $(\eta - \kappa)$  is vector valued (with dimensions corresponding to the dimension of the parameter space). Such a treatment is relevant for varying material parameters independently throughout the volume, for instance if the permittivity of each element in the discretization is described by a random variable.

For example, we consider the 2-dimensional case where the perturbation is complex valued. Hence,

$$\boldsymbol{\eta} = \begin{bmatrix} \eta_r \\ \eta_r' \end{bmatrix}, \quad (4.22)$$

and likewise for  $\boldsymbol{\kappa}$ . The derivative matrix corresponding to the subtraction of (4.18) and (4.19) is then

$$\mathbf{D} = \begin{bmatrix} k_0^2 \mathbf{E}^{inc} + k_0^2 \mathbf{E}^{ref} & j k_0^2 \mathbf{E}^{inc} + j k_0^2 \mathbf{E}^{ref} \end{bmatrix}. \quad (4.23)$$

As a result, the updated form of (4.20) is

$$\langle \tilde{\mathbf{E}}^{sc}, \mathbf{p} \rangle \approx \langle \mathbf{E}^{ref}, \mathbf{p} \rangle + k_0^2 \langle \mathbf{D}(\boldsymbol{\eta} - \boldsymbol{\kappa}), \mathbf{v} \rangle, \quad (4.24)$$

which is equivalent to simply treating  $\eta$  and  $\kappa$  as complex valued in the 1-dimensional parameter space estimate.

In addition to improved accuracy in general, for highly sensitive QoIs, or for large variance in the perturbed parameter, it is preferable to sample at multiple reference points. We can accomplish this by sampling at a uniform set of grid points or, for example, we can probabilistically tune the HOPS approximation efficiently with  $k$ -means clustering. In either case, samples of the perturbed parameter are associated with a reference point by proximity and the updated QoI is approximated as in (4.17).

### 4.3 Numerical Results

As discussed in Section II, the connection of the adjoint solution to the sensitivity of the QoI permits the effective estimation of changes in the QoI to parameters in the model. In each of the following numerical examples, we consider monostatic scattering from a sphere. While simple geometrically, the spherical scatterer, nevertheless, allows exploration of the prototypical problems in UQ. We note, however, several practical considerations for application to more complex problems and geometries. Chief in the value of the HOPS approach, not all parametric uncertainty drives equivalent effect in the QoI. In the case of multilinear dependence of the QoI on the uncertain parameters, the response may be constructed precisely for high dimensional uncertainty by a single HOPS point. Likewise, when sources of uncertainty induce limited effect in the QoI, significant resources may be saved without harm to the accuracy of the estimated probability densities. In the case of surface roughness, for example, the QoI may be insensitive to variation in a large portion of the surface, simplifying the computational procedure drastically. However, depending on the specific geometry and the scattering angle, a small degree of uncertainty may drive large variation in the QoI; in such cases, additional computational resources must be allocated to compensate, resulting in a denser distribution of HOPS points. Finally, the HOPS approach facilitates increasing computational effort where uncertainty dictates the largest change in the QoI. In the following examples, we illustrate the performance of the method for uniform sampling and probabilistically tuned sampling. In addition, the approach is conducive to adaptivity, which, in the case highly sensitive QoIs, simplifies the selection of HOPS points.

Consider a spherical scatterer with uncertain material parameters. We first impose that the conductivity of the entire sphere—considered as the imaginary component of the complex relative permittivity  $\varepsilon_d$ —is a random variable which varies according to some distribution  $\pi(x)$  with a known mean  $\nu$  and standard deviation  $\sigma$ . Therefore, according to the principle of maximum entropy, we let  $\pi$  denote a Gaussian distribution; however, any other distribution can be substituted (or treated simultaneously).

Furthermore, as the conductivity is a random variable, the solution itself is a random vector, and hence the QoI is a random variable. We therefore conduct a MC simulation of  $N$  samples to generate an approximate probability distribution which describes the behavior of the QoI.

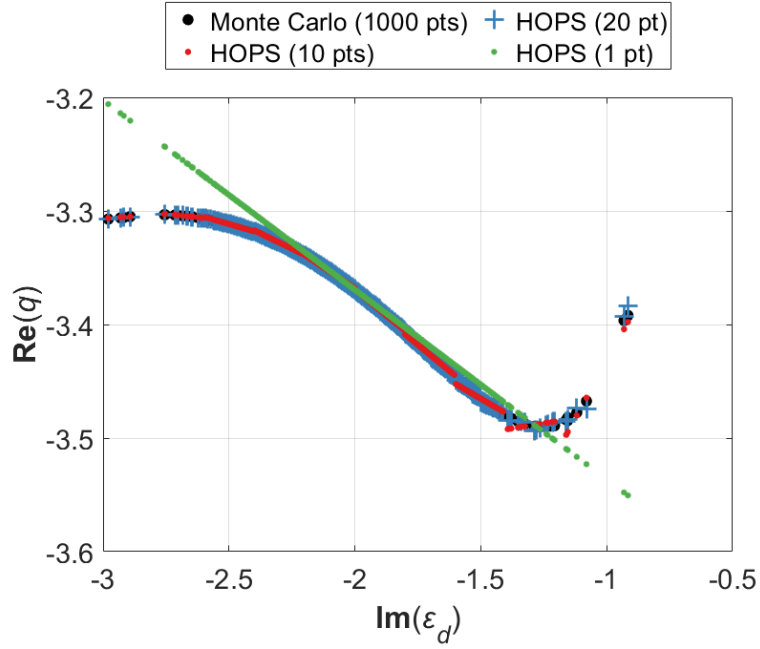
In each of the  $N$  runs, the imaginary component of the sphere's relative permittivity is drawn from  $\pi$ , and—after solving the forward problem on this discretization—the QoI from (4.7) is computed and stored, which we denote as  $q$ . For comparison, the results are demonstrated for three levels of HOPS resolution, with one, ten, and twenty HOPS reference points. Compared to [5], the numerical examples herein were performed with greater precision.

For a specific test case, let  $\pi$  be a Gaussian distribution of mean  $\nu = -2.0$ , and standard deviation  $\sigma = 1/3$ . The real component of the relative permittivity of the sphere is fixed at 6.0. For simplicity, the HOPS points were chosen uniformly within three standard deviations of the mean for the multi-point simulations, while the mean was selected for the single-point HOPS simulation.

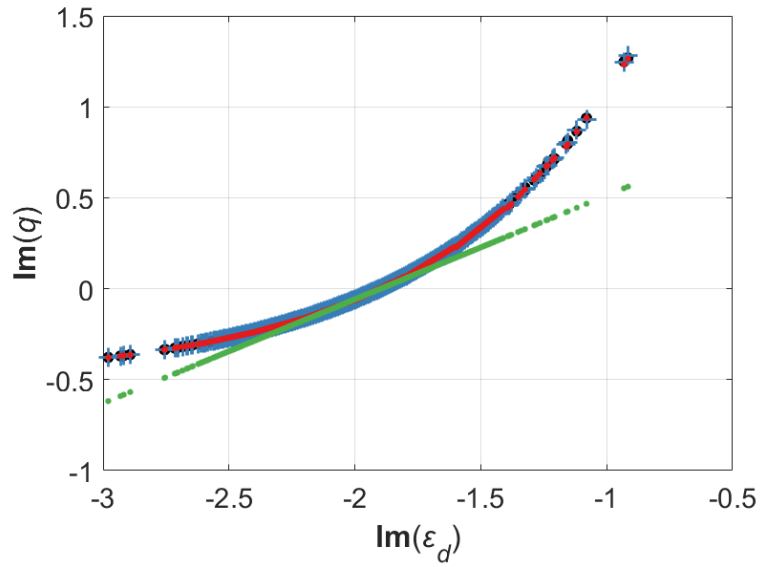
As seen in Fig. 4.1, the adjoint-based method provides an accurate approximation of the QoI behavior and replication of the MC sampling. While the pure linear approximation about a single reference point diverges from the MC simulation near the extrema of the sample domain, the ten- and twenty-point HOPS simulations successfully capture the QoI response over the entire range.

We now apply HOPS to estimate the QoI probability densities using Gaussian kernel density estimation (GKDE) with bandwidths chosen according to Silverman's heuristic [137], as seen in Fig. 4.2, with the real and imaginary components extracted separately (i.e., as two individual sub-QoIs) to streamline analyzing the convergence behavior. It should be noted, however, that the real and imaginary components are not strictly independent as the full, complex-valued QoI follows a joint distribution of two real random variables (one for the real component and one for the imaginary). Considering this treatment, the probability densities associated with variation in the conductivity for the two sub-QoIs are represented with acceptable accuracy by a single reference point. By ten or twenty reference points, however, the agreement with the 1000-point MC simulation is near-perfect.

We now quantify the performance of the three HOPS approximations by comparing the mean, variance, and total variation (TV) distance between the HOPS and MC densities. The TV distance,



(a)



(b)

**Figure 4.1:** Sampled real and imaginary monostatic scattering QoI responses for random variation in the imaginary component of the relative permittivity of the dielectric sphere. (a) Real component of the QoI. (b) Imaginary component of the QoI.

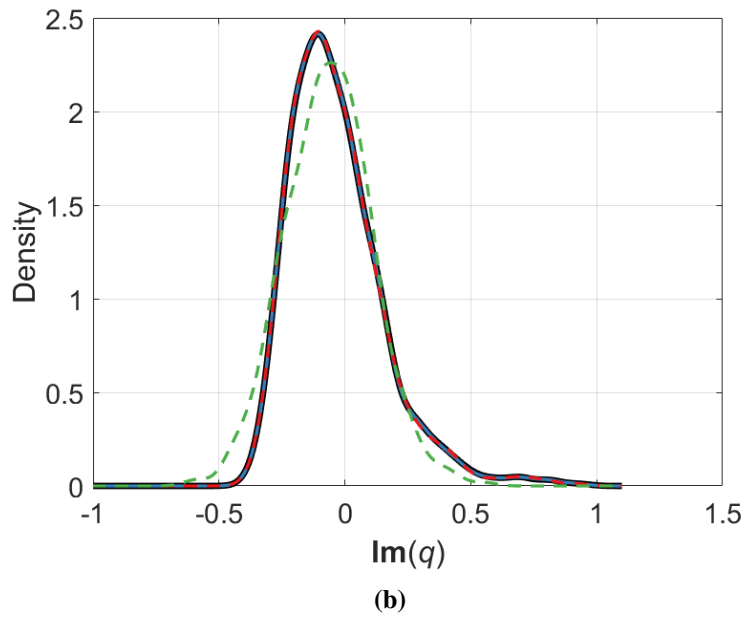
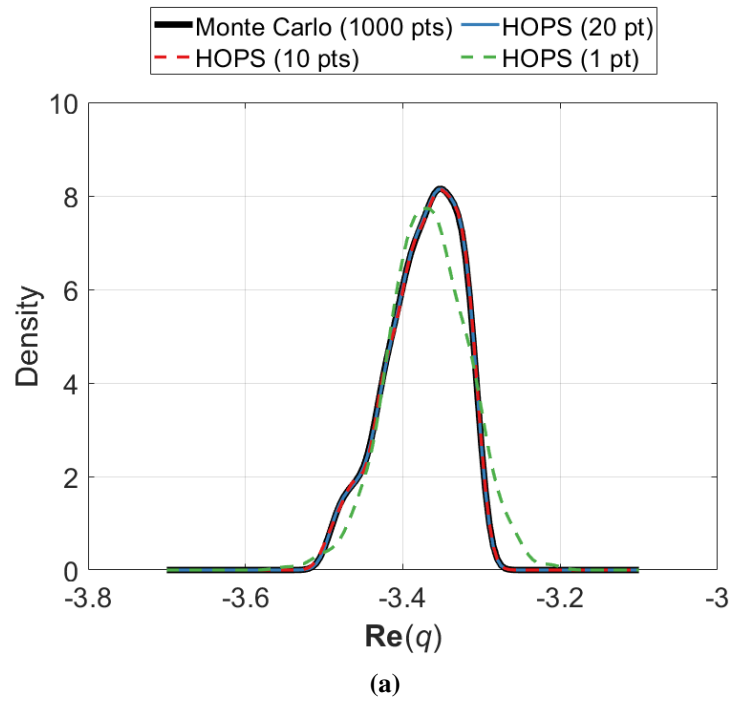


**Figure 4.2:** Approximate real and imaginary monostatic scattering QoI probability densities due to random variation in the imaginary component of the relative permittivity of the dielectric sphere. (a) Probability density for the real component of the QoI. (b) Probability density for the imaginary component of the QoI.

which is related to the  $L^1$  norm, provides a measure of the similarity of two probability distributions, where a value of zero indicates perfect agreement. As seen in Table 4.1, HOPS converges to the 1000-point MC simulation by ten reference points, producing an almost identical mean and variance for both the real and imaginary components. Lastly, the TV distances indicate extremely strong agreement with the MC densities for the two higher resolution approximations.

**Table 4.1:** Quantitative comparison of HOPS and Monte Carlo for the real and imaginary QoI probability densities in Fig. 4.2.

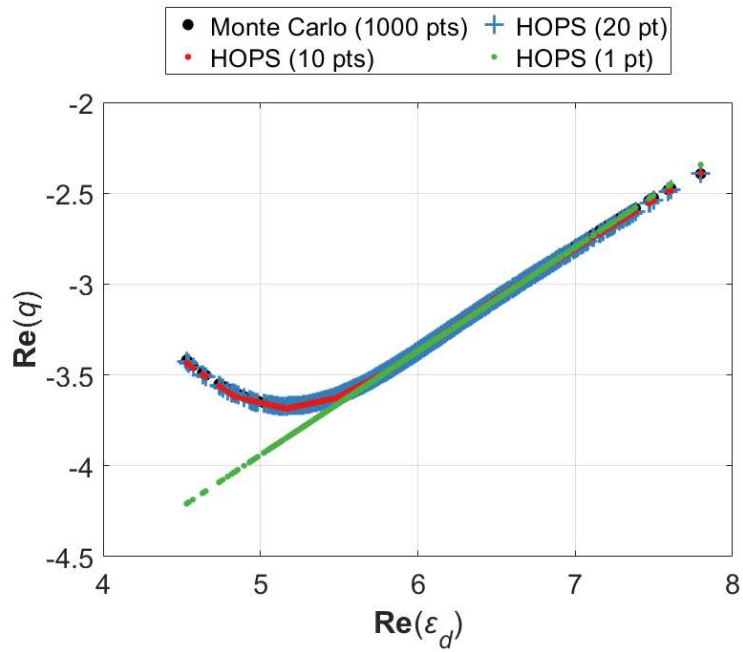
(a) Real QoI Density				
	1 pt	10 pts	20 pts	MC
Mean	-3.36780771	-3.37410172	-3.37407407	-3.37421665
Variance	0.00272574	0.00224150	0.00220986	0.00221224
TV	0.20391318	0.01276973	0.00458447	

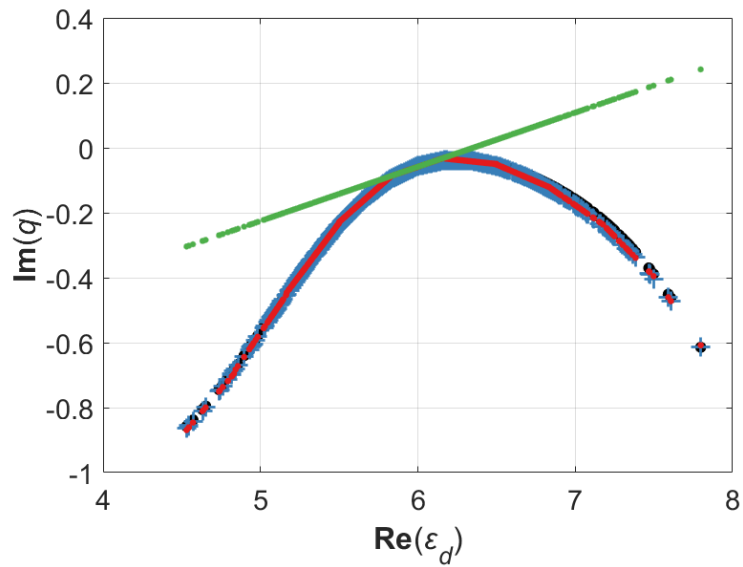
(b) Imaginary QoI Density				
	1 pt	10 pts	20 pts	MC
Mean	-0.06429527	-0.03129427	-0.03026978	-0.02974337
Variance	0.03192723	0.04030004	0.04056085	0.04068723
TV	0.18801598	0.01218528	0.00351265	

To further validate the effectiveness of the HOPS methodology, we repeat an identical procedure for random variation in the real component of the relative permittivity. In contrast to the variation in the conductivity, random variation in this component of the relative permittivity induces a more complicated QoI response. Specifically, in this case the real component of the relative permittivity is described by a normal random variable of mean  $\nu = 6.0$  with a standard deviation  $\sigma = \sqrt{3}/3$ , and the imaginary component is fixed at  $-2.0$ . As before, the HOPS reference points are chosen uniformly within three standard deviations of the mean.

For the first level of accuracy, as seen in Figs. 4.3 and 4.4, a single HOPS reference cannot adequately replicate the QoI response. Due to its more linear response, however, the real component of the QoI is much more reasonably modeled by the single HOPS point.



(a)



(b)

**Figure 4.3:** Sampled real and imaginary monostatic scattering QoI responses for random variation in the real component of the relative permittivity of the dielectric sphere. (a) Real component of the QoI. (b) Imaginary component of the QoI.

With ten reference points, and even more so with twenty reference points, the HOPS QoI response very closely matches that of the very computationally expensive MC simulation. As seen especially clearly in Fig. 4.3, the multi-point HOPS simulations very accurately capture the non-linear response of the QoI over the entire sample region.

**Table 4.2:** Quantitative comparison of HOPS and Monte Carlo for the real and imaginary QoI probability densities in Fig. 4.4.

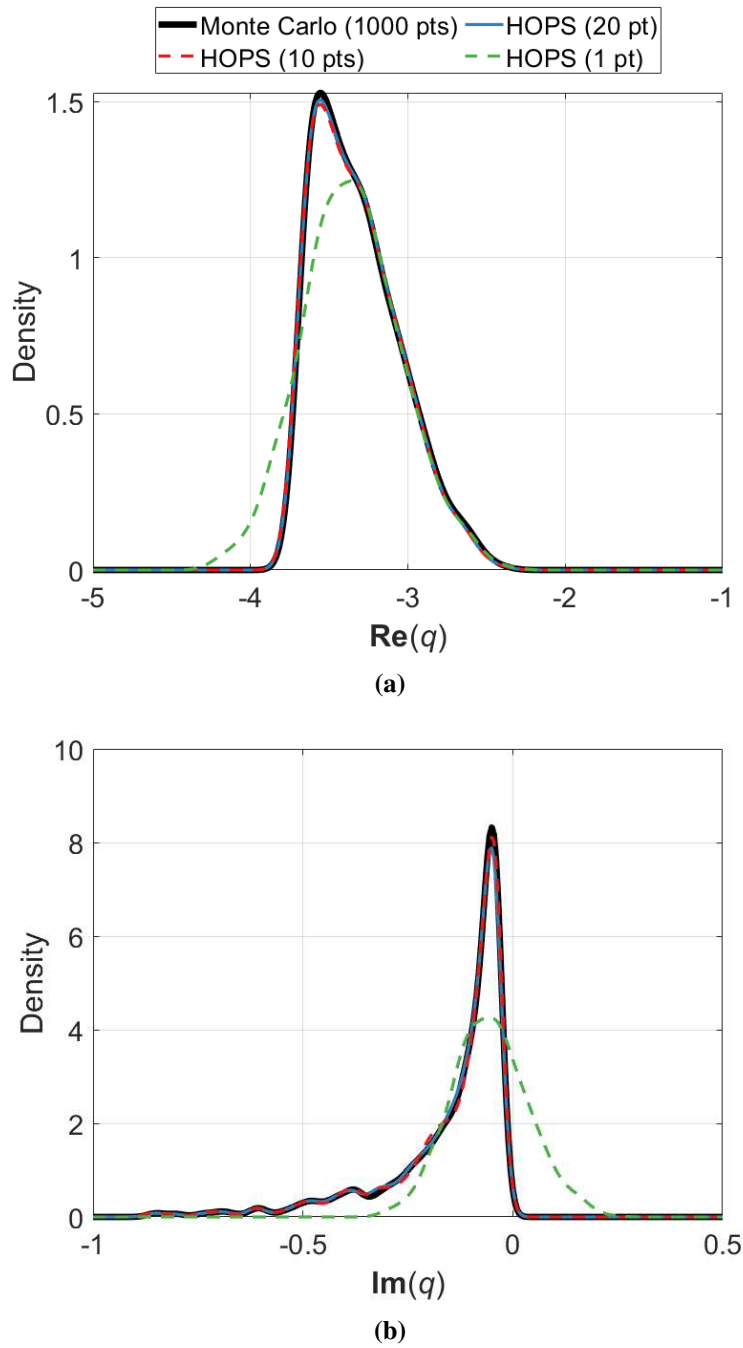
(a) Real QoI Density				
	1 pt	10 pt	20 pt	MC
Mean	-3.35643835	-3.32473341	-3.32361857	-3.31969585
Variance	0.10483824	0.07707825	0.07649920	0.07785312
TV	0.20138302	0.02398625	0.01722823	

(b) Imaginary QoI Density				
	1 pt	10 pts	20 pts	MC
Mean	-0.05484124	-0.14907843	-0.15105419	-0.14822206
Variance	0.00895042	0.02262963	0.02248283	0.02221925
TV	0.67549079	0.04367983	0.03785603	

Moreover, the approximate densities for the real and imaginary components of the QoI demonstrate extremely close agreement with the MC simulation, as seen in Fig. 4.4 and Table 4.2. In contrast to the variation in the imaginary component of the permittivity, in this case the twenty-point HOPS approximation provides a substantial boost in accuracy. While the ten- and twenty-point approximations provide close agreement with the mean and variance of the MC simulation, the twenty-point approximation produces improved TV distances for the real and imaginary components.

As discussed in Section II, however, the adjoint approach excels when analyzing multiple parameters, and therefore many gradients at each reference. As a simple extension of the previous results, we demonstrate the combination of the two previous examples by assuming random variation of the real and imaginary components of the relative permittivity of the dielectric sphere. The real



**Figure 4.4:** Approximate real and imaginary QoI probability densities due to random variation in the real component of the relative permittivity. (a) Probability density for the real component of the QoI. (b) Probability density for the imaginary component of the QoI.

and imaginary components are described by separate random variables such that  $\text{Re}(\varepsilon_d)$  is Gaussian with a mean of 2.56 and a standard deviation of 0.2, and  $\text{Im}(\varepsilon_d)$  is pulled from a half-normal distribution of mean 0 and standard deviation 0.1.

In this case, the references are determined by  $k$ -means clustering of the set of sampled material parameters, which provides another simple and effective HOPS selection scheme. In contrast to PCE and similar methods, we can leverage the parameter distribution to easily emphasize regions of the QoI response deemed statistically important by the probability distribution imposed on it. As such, selecting reference points by  $k$ -means clustering enables an efficient probabilistic tuning of the HOPS approximation, particularly for high dimensional uncertainty. We repeat this procedure, as before, for three levels of resolution, with one, ten, and twenty references.

To illustrate the QoI reconstruction behavior for a two-dimensional parameter space, the approximate QoI responses are shown for the ten-point HOPS simulation in Fig. 4.5. Note that each estimate is associated with a single reference point as determined by Euclidean distance. This allocation of HOPS points is illustrated further in Fig. 4.6, showing how each sample point is assigned to a given reference point. The approximations, which are linear in both dimensions, demonstrate accurate replication of the QoI response generated through a 1000-point MC simulation. As implied by the QoI response in Fig. 4.5, the single-point HOPS simulation fails to capture the behavior of the problem to random variation of the dielectric, and therefore fails to match the probability density of the QoI in Fig. 4.7. However, using ten reference points, the HOPS density closely matches the MC density, with the twenty-point HOPS simulation providing even more accuracy in the response. The results in Table 4.3 further characterize the performance of the HOPS approximations.

As a final demonstration, to further illustrate the advantage of the QoI-emphasis inherent to the HOPS approach, we consider a much higher dimensional example, in which every element of the spherical scatterer body is uncertain. This example corresponds to a 64-dimensional parameter space, where the material parameters of each element are purely real and independent and identically distributed such that  $\varepsilon_{d_i} \sim N(2.56, 0.07^2)$  for the  $i$ th element.

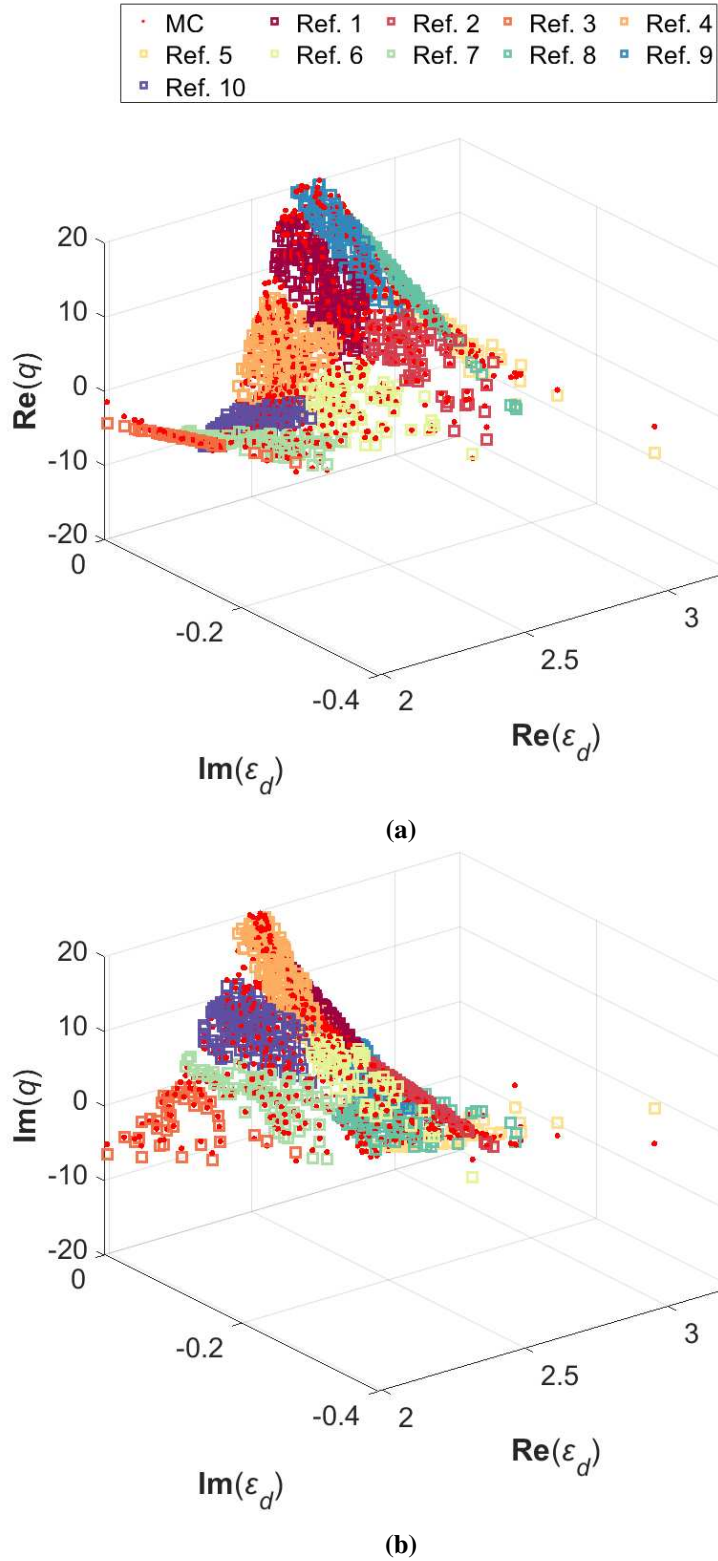


**Figure 4.5:** Approximate real and imaginary monostatic scattering QoI responses due to simultaneous random variation in the real and imaginary components of the relative permittivity of the dielectric sphere for a HOPS simulation with ten reference points. (a) Real component of the QoI. (b) Imaginary component of the QoI.

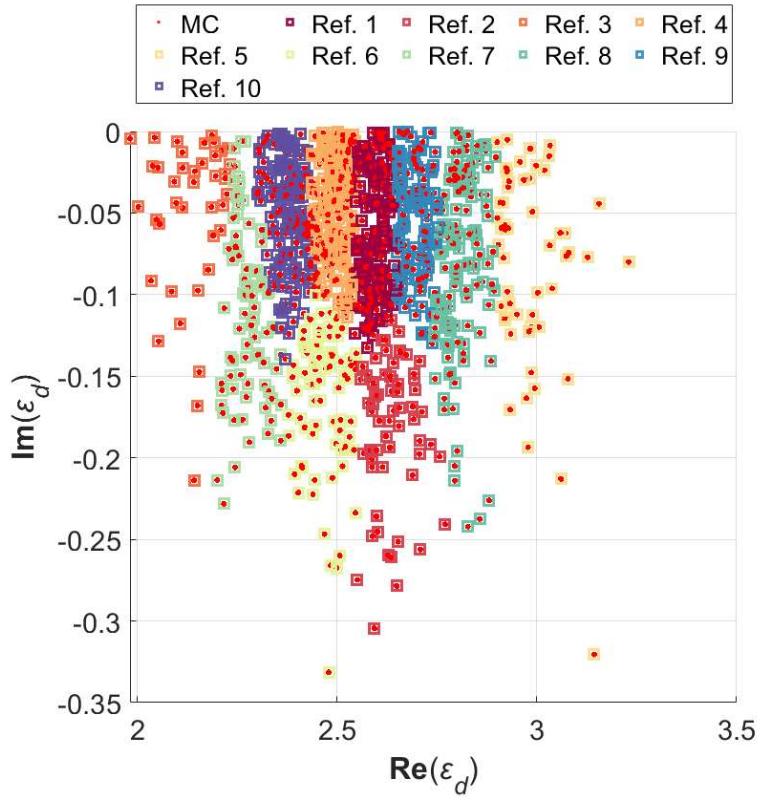


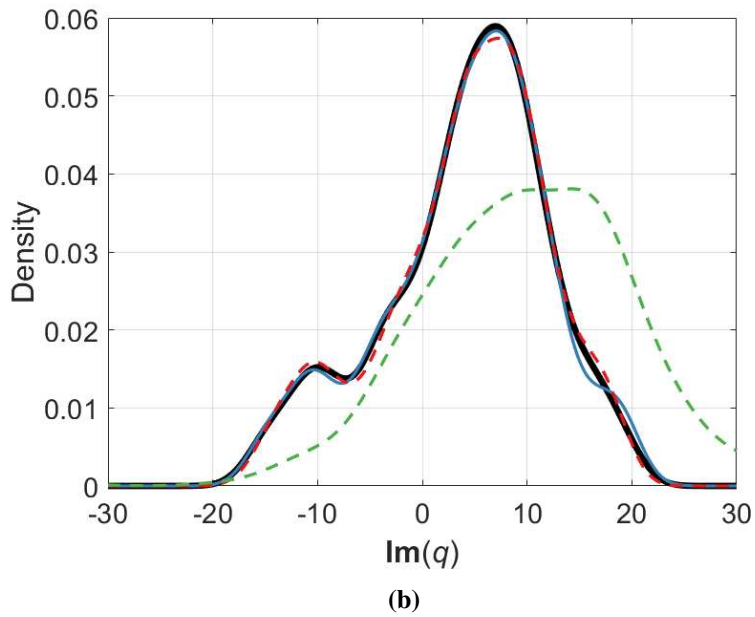
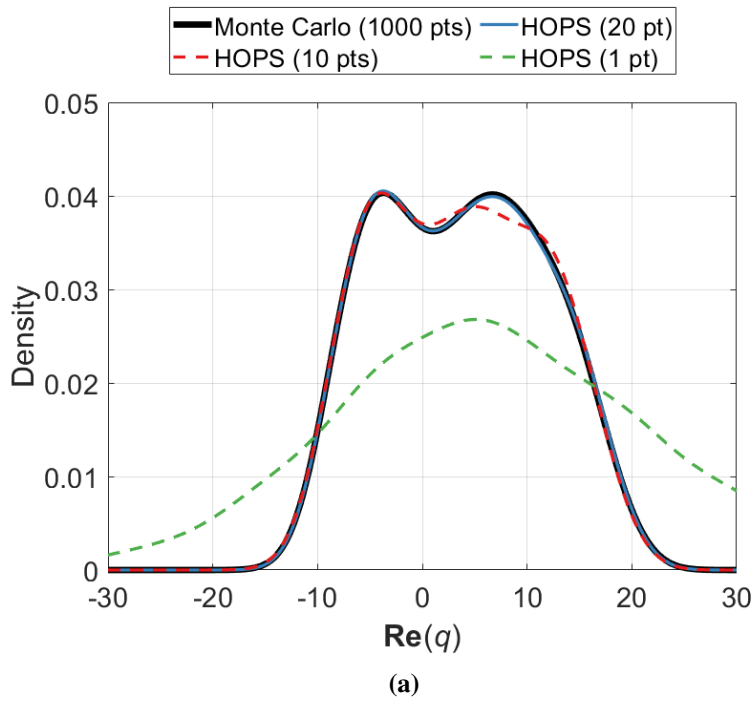
**Figure 4.6:** Illustration of the clustering of the HOPS points based on  $k$ -means probabilistic tuning.

**Table 4.3:** Quantitative comparison of HOPS and Monte Carlo for the real and imaginary QoI probability densities in Fig. 4.7.

(a) Real QoI Density				
	1 pt	10 pts	20 pts	MC
Mean	6.58809661	3.55730226	3.65209536	3.64495793
Variance	233.79786869	65.49914507	65.49652720	65.37250943
TV	0.61771136	0.02376743	0.00624561	

(b) Imaginary QoI Density				
	1 pt	10 pts	20 pts	MC
Mean	9.95630077	4.13943868	4.08910492	4.07601222
Variance	99.42392714	65.31487120	67.01658893	65.89625572
TV	0.57929508	0.03201564	0.02867375	



**Figure 4.7:** Approximate real and imaginary monostatic scattering QoI probability densities due to simultaneous random variation in the real and imaginary components of the relative permittivity of the dielectric sphere. (a) Probability density for the real component of the QoI. (b) Probability density for the imaginary component of the QoI.

We continue the approach in the previous examples, with a 1000-point MC simulation providing the benchmark for the HOPS based approximation. As seen in Fig. 4.8, given the relatively small variance of  $\varepsilon_{d_i}$  and the approximately multilinear local relationship between the uncertain parameters and the QoI, the probability density is closely replicated by a single HOPS point. The HOPS approximation yielded TV distances of 0.07886044 and 0.12823617 with respect to the real and imaginary MC densities. While the previous examples illustrate the potential for high accuracy, this example fully demonstrates the significant computation time reduction that HOPS facilitates. A standard gradient estimation strategy to predict the distribution of the QoI under uncertainty as in this example would require 65 solves of the forward problem, whereas the HOPS simulation requires only one solution to the forward problem and one solution to the adjoint problem.

Overall, when analyzing the computational performance of HOPS compared to the MC simulations, we see a significant reduction in the computational cost. In the case of the MC simulations with 1000 samples, as the finite element discretizations have the same degrees of freedom for each approach, the single-point HOPS simulation yields an improvement in computation time by a factor of 500. Likewise, the ten- and twenty-point HOPS simulations reduce the computational cost by a factor of 50 and 20, respectively. Furthermore, as the HOPS reconstruction matches the full QoI response rapidly with increasing resolution, larger performance increases may be found when studying larger equivalent MC simulations. Finally, while the examples demonstrated apply uniform sampling and probabilistically tuned sampling, adaptive HOPS may yield additional performance increases and simplify application of the method to arbitrary uncertainty quantification problems in CEM.

## 4.4 Conclusion

We have demonstrated the advantage of adjoint-based local sensitivity analysis for expediting uncertain quantification in 3-D frequency domain CEM. Through application of the adjoint solution, the HOPS methodology in CEM facilitates rapid and accurate prediction of variation in practical quantities of interest in the presence of uncertainty and randomness in scattering models.

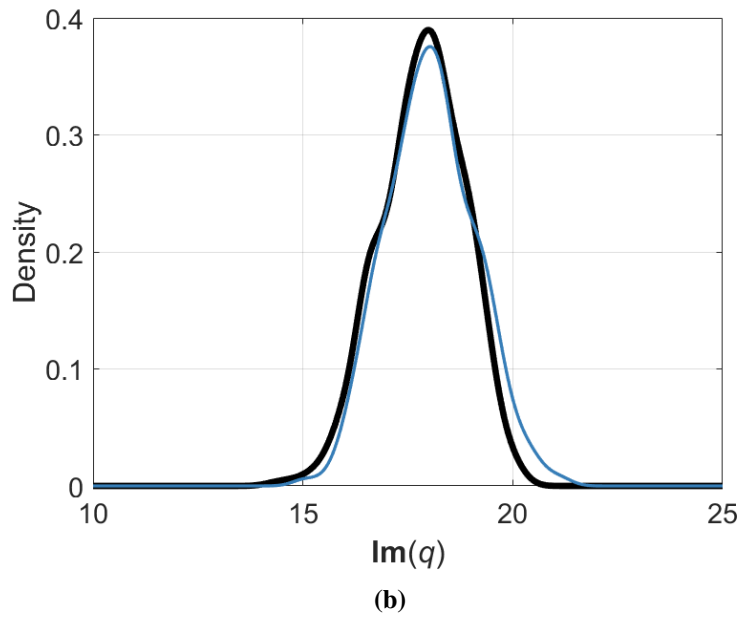
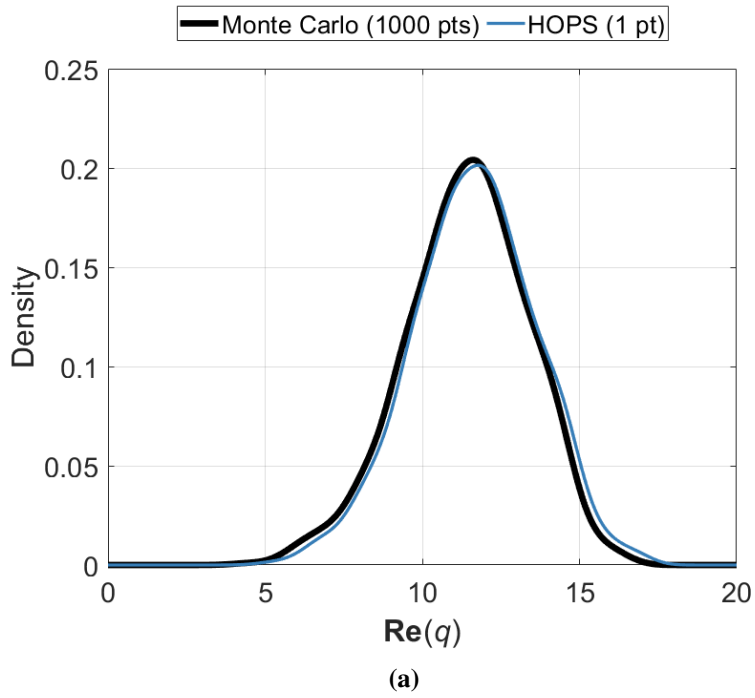


**Figure 4.8:** Approximate real and imaginary monostatic scattering QoI probability densities due to random variation in the relative permittivity of each element of the dielectric sphere. (a) Probability density for the real component of the QoI. (b) Probability density for the imaginary component of the QoI.

For outcome prediction of uncertain parameters, we contributed explicit constructions for evaluating random variation in the material parameters of a scatterer. And, finally, we showed how leveraging the adjoint solution and HOPS can replicate extremely computationally expensive Monte Carlo simulations at a small fraction of the cost and with similar accuracy, mandating just a handful of HOPS reference points for extremely close agreement.

For one-dimensional parameter spaces, the adjoint-based approach matches the efficiency of traditional methods, and in such cases where the original discretization is constructed through adjoint-based adaptive refinement, the readily available adjoint significantly boosts the effective performance of the HOPS method.

We further demonstrated application to higher dimensional parameter spaces, including a 2-dimensional problem, and a 64-dimensional problem with independent material uncertainty throughout the scatterer. In these cases, the independence of the computational complexity from the number of parameters results in substantial decreases in computation time while maintaining high accuracy.

We note several drawbacks of the proposed method in its current form for uncertainty quantification. Firstly, when analyzing the effect of uncertainty on multiple quantities of interest, each QoI requires its own adjoint solution. Of course, when leveraging direct solvers, the added cost of solving multiple right-hand-sides for the adjoint problem may be significantly reduced. Secondly, while the HOPS methodology is extremely versatile and accurate results may be achieved efficiently even with uniform sampling, optimizing the selection of HOPS points requires either *a priori* knowledge or adaptivity. For broad applicability in analyzing uncertainty in CEM, we consider augmenting the proposed approach with adaptivity as the next key extension needed.

Adjoint-based methodologies, overall, provide significant value and potential to CEM applications, enabling the ability to accurately and efficiently refine models and eliminate discretization error fully automatically, while also significantly expediting the analysis of problems containing extensive random variation and uncertainty. Future works will investigate automating sampling for

improved efficiency and accuracy for high dimensional parameter spaces and highly sensitive QoI responses.

# Chapter 5

## A Refinement-by-Superposition *hp*-Method for $H(\text{curl})$ - and $H(\text{div})$ -Conforming Discretizations

### 5.1 Introduction

Geometric discretization by quadrilaterals and hexahedra, while significantly more accurate with respect to degrees of freedom (DoFs) than modeling with triangles or tetrahedra [138], presents significant challenge to fully dynamic mesh adaptivity. In refinement with triangles and tetrahedra, local adaptivity directives propagate to a small set of neighboring elements, enabling the insertion of new DoFs without modification to the entire element structure. Similar refinement approaches with quadrilateral and hexahedral cells, however, would dictate global refinement, thereby destroying the utility of  $h$ -adaptivity. Inserting transition elements also poses significant challenge to the approximation quality, particularly for vectorial shape functions, which rapidly degrades as the unit vectors lose linear independence in the physical domain. Finally, application of a discontinuous Galerkin method, while evading this problem, among its other difficulties, generally requires more DoFs for the same level of accuracy.

As shown in [58–61], when the solution satisfies certain regularity conditions,  $p$ -refinement enables exponential convergence; when such conditions are not satisfied, however, the benefit of  $p$ -refinement is heavily degraded, reduced instead to algebraic convergence as in the case of pure  $h$ -refinement. Pure  $p$ -refinement, while effective in certain situations (e.g., [68]), is therefore insufficient in general, and as such, a combined approach with both  $h$ - and  $p$ -adaptivity is necessary to achieve exponential convergence for solutions with singularities or non-smooth behavior, motivating the need for more advanced and versatile approaches to  $h$ -refinement.

Previous works in CEM, for example, have demonstrated the potential of  $hp$ -adaptivity through hybrid meshes, e.g., in [139]. Most typically, however, to address the  $hp$ -adaptivity limitations

the insertion of constrained-nodes, which—in contrast to true DoFs—are constrained to enforce continuity conditions with neighboring elements, is performed. Such approaches in CEM have shown significant performance increases and exponential convergence in the presence of singular solutions [13, 22, 23, 70–72], but at the cost of high implementation complexity, impeding wide-scale adoption. Furthermore, such methods are usually limited in implementation to 1-irregular meshes (i.e., only one hanging node per edge), which, while not a severe limitation in practice, prevents arbitrary local refinement steps. Open-source libraries—such as deal.II [4]—have significantly simplified the implementation of  $hp$ -refinement codes, yet in some cases it might be inconvenient or undesirable to utilize third-party finite element method (FEM) libraries.

As such, we opt to extend the refinement-by-superposition (RBS) approach introduced in [140–142] for hierarchical basis functions, which demonstrated exponential convergence for scalar problems with  $C^0$  finite elements, to  $H(\text{curl})$ - and  $H(\text{div})$ -conforming finite elements. Additional studies with  $C^0$  finite elements and the RBS  $hp$ -method with adaptivity in [143] further motivate extensions of the method to CEM.

While the proposed approach significantly simplifies the implementation of  $hp$ -refinement infrastructure for applications in CEM, in contrast to more traditional refine-by-replacement (RBR) strategies, the proposed approach decreases the sparsity of the system matrices under both  $h$ - and  $p$ -refinements, whereas RBR only reduces sparsity under  $p$ -refinements. The proposed approach is therefore less suitable for application to very large problems with vast differences in scales. For applications of the approach to boundary element method (BEM) problems, e.g., surface integral equation (SIE) problems in CEM discretized by the method of moments (MoM), such considerations do not apply given the global nature of the Green’s function, but would instead concern the increase in integration time due to the overlap of refinement layers.

The remainder of this paper is organized as follows. Section II details the construction of the RBS  $hp$ -method, covering the enforcement of the required continuity conditions (tangential or normal continuity) and ensuring linear independence after the insertion of descendant refinement layers. Section III examines application to an  $H(\text{curl})$ -conforming discretization of the Maxwell

eigenvalue problem. We examine a challenging eigenpair with a singular eigenfunction as studied in [3]. The presented approach yields exponential convergence of the eigenvalue with respect to the number of degrees of freedom (NDoFs), which, along with the ease of implementation, illustrates the practical value for applications in CEM.

## 5.2 Refinement-by-Superposition: Description and Construction

With an underlying hierarchical  $H(\text{curl})$ - or  $H(\text{div})$ -conforming basis, such as introduced in [144], exponential convergence may be achieved with suitable refinements by a collection of overlay meshes. This RBS approach yields the desired discretization by imposing homogeneous Dirichlet boundary conditions on the boundaries of the inserted descendant cells (i.e., the collection of overlay meshes) [140–142]. Continuity requirements, therefore, may be easily enforced for arbitrary levels of refinements (i.e.,  $n$ -irregular meshes) and heterogeneity in the chosen orders of the hierarchical basis throughout the mesh. This enables an algorithmically straightforward and low-cost method to add  $hp$ -refinement capabilities for  $H(\text{curl})$ - and  $H(\text{div})$ -conforming discretizations by enforcing, respectively, tangential and normal continuity.

We approach the description explicitly from a 2-D perspective; however, the process generalizes trivially to 3-D. First, we classify each shape function in the following manner. In the case of an  $H(\text{curl})$ -conforming discretization, we assign each shape function according to the properties of the non-zero tangential components at the boundary of the cell. These shape functions are classified into three categories: the node-functions, i.e., those functions with non-zero tangential components at only one node; the edge-functions, i.e., those functions with non-zero tangential components along one and only one edge; and the cell-functions, i.e., those functions which have no non-zero tangential components on the boundary. The existence of node-functions is only necessary when in 2-D, the axial component (i.e., perpendicular to the 2-D plane of the geometry) of the solution is non-zero, as in the examples in [68]. The same classification strategy, albeit according to the non-zero normal components at the boundary, is applied for seeking solutions in  $H(\text{div})$ . Naturally,

the difficulty in inserting unknowns rests in the treatment of the edge-functions (and potentially the node-functions), while the cell-functions, which introduce no DoFs influencing the boundary, may be inserted or excised without non-local considerations.

Given some starting mesh, which, without loss of generality, we assume to be regular, refinement directives are then executed. Furthermore, while we focus on isotropic refinement, the superposition-based approach supports anisotropy in  $p$ -refinement directives trivially and, with modification, to anisotropic  $h$ -refinements [145]. For example, for a single  $h$ -refinement step applied to one cell in 2-D, four new child cells are inserted one refinement layer above the parent cell according to the constraint of isotropic refinement only. Note that geometrically, the child cells lie in the same physical space as the parent; rather, the designation of “above” is purely conceptual.

We have two simultaneous considerations in the process: continuity and linear independence. Continuity must be enforced due to potential non-uniformity in the polynomial degree of the basis on neighboring cells and the existence (or lack thereof) of child cells on the various refinement levels. Linear independence, on the other hand, is guaranteed by the proper delegation of DoFs between the refinement layers descended from the origin cell. DoFs must be deactivated on the parent cells and activated on the child cells, depending on the refinement levels of the cell and its neighbors.

The refinement and coarsening directives are applied for both cases through the assignment of the DoFs to the geometrical structures as mentioned above (the cells, the edges, the nodes, and, in 3-D, the faces).

### **5.2.1 Enforcing Continuity Requirements**

The activation and deactivation of the DoFs on the boundaries of the cells follows a unified procedure based on [140–142]. For each layer in the discretization, from the origin layer to the highest refinement layer, DoFs are assigned to each of the geometrical elements according to the continuity requirements desired, in this case, tangential continuity for seeking a solution in

$H(\text{curl})$  and normal continuity for  $H(\text{div})$ . Each cell, edge, node (when necessary in 2-D), and face (exclusively in 3-D) collects a list of DoFs, both active and inactive.

As the DoFs are accumulated, each one is matched as necessary with the associated shape functions on neighboring cells according to the vectorial direction and multi-index of the associated shape function. As opposed to the boundary-functions (i.e., node, face, and edge), the cell-functions automatically satisfy continuity requirements and therefore no special considerations are necessary except for those related to ensuring linear independence. The boundary-function DoFs are marked as active according to the existence of neighbors in the refinement level and the expansion order of those cells. Both restrictions are handled seamlessly and without distinction as the overall process amounts to traversing the geometrical entities in the discretization, which are assigned their maximal sets of associated DoFs, and activating only the DoFs according to the above compatibility conditions.

We summarize the procedure for activating DoFs based on the continuity requirements as follows:

1. For each cell, edge, node, and face in each refinement layer, collect the associated DoFs
  - (a) For  $H(\text{curl})$ , associate the DoFs based on the non-zero tangential components
  - (b) For  $H(\text{div})$ , associate the DoFs based on the non-zero normal components
2. Iterate through each refinement layer and each edge, node, and face
  - (a) If a suitable refinement neighbor exists, match the shape functions associated with the adjacent cells, activating only the fully matched DoFs and deactivating the rest

### **5.2.2 Eliminating Linear Dependence of the Hierarchical Refinements**

For ensuring linear independence between overlapping shape functions, we prioritize the highest feasible refinement level possible. For example, the cell-functions, which by definition satisfy the continuity requirements automatically, require deactivation on the parent cell and activation of the

DoFs on the child cells. Unlike the handling of the edge- and node-functions, this transfer occurs without any queries to the discretization other than checking if the descendant cells exist.

Now, for the edge- and node-functions, additional care is necessary. In this case, the preference to delegate DoFs to the child cells is constrained by the refinement state of one or more neighbors of the cell. In other words, in 2-D, if a parent cell shares an edge with another refined parent cell, the DoFs on the parent edge may be transferred to the corresponding edges on the child refinement layer. Likewise, the deactivation of a node-function on the parent refinement layers requires that the corresponding node is surrounded by refined cells. In other words, as in [140–142], active geometrical components may not “overlap” with respect to the refinement layers.

We summarize the activation and deactivation of DoFs as follows:

1. On an  $h$ -refinement step, deactivate cell-functions on the parent cell and activate the cell-function DoFs on the child cell.
2. If a geometrical component (a node, edge, or face) on the descendant layer is active (i.e., it has associated active DoFs), deactivate the corresponding component on the parent layer

According to this procedure, a parent cell sufficiently surrounded by refined cells may be entirely deactivated to ensure linear independence and maximize the resolution of the approximation. In such cases, the sparsity of the resulting system is enhanced.

### 5.2.3 Summary of the Overall Approach

Illustrated in Fig. 5.1, the entire procedure, from enforcing the continuity requirements to ensuring linear independence, requires only the straightforward rules as summarized in the preceding subsections. Similarly to the descriptions of the RBS process in 1-D in [140–142], Fig. 5.1(a) summarizes the procedure for a 1-D domain, including the transfer of DoFs associated with lower refinement levels to the descendant layers and the ability to choose the expansion order  $p$  arbitrarily. Note that in 1-D, we have only the linear class of boundary-functions, i.e., at the boundary between two cells (across all the refinement levels), only one active boundary-DoF exists. The hierarchical

basis functions illustrated in Fig. 5.1(a) and those used in the Numerical Results Section are based on the maximally-orthogonalized basis functions [144].

In 2-D (and 3-D), however, many active DoFs exist on the cell boundaries as a result of employing higher order boundary-functions. Depicted in Fig. 5.1(b), we demonstrate a similar refinement model as in the 1-D case. Unlike in the 1-D case, the depicted refinement in 2-D results in the enforcement of the domain boundary conditions propagating to the higher refinement levels when available. Furthermore, in this case, many of the parent cells retain a large number of DoFs assigned to the boundary due to the higher order boundary-functions. In Fig. 5.1(b), such occurrences are denoted by the cells with solid boundaries and transparent interiors, in addition to the matching designations related to the active geometrical components as seen in Fig. 5.1(a).

Finally, for each cell located on a new refinement layer, an additional mapping is introduced, resulting in a succession of mapping operations. Note, however, that regardless of the curvature of the origin cell, all other mappings from the reference cell to the child cell have constant Jacobian determinants, and may be handled with ease during integration.

### 5.3 Numerical Results

We now demonstrate the suitability of the RBS  $hp$ -refinement methodology by solving the following Maxwell eigenvalue problem (in variational form):

Find  $U = \{\mathbf{u}_{hp}, \lambda_{hp}\} \in B_{hp} \times \mathbb{R}$  such that

$$a(\mathbf{u}_{hp}, \phi_{hp}) = \lambda_{hp} m(\mathbf{u}_{hp}, \phi_{hp}) \quad \forall \phi_{hp} \in B_{hp}, \quad (5.1)$$

for a finite dimensional subspace  $B_{hp} \subset H(\text{curl}; \Omega)$ , where  $m(\mathbf{u}_{hp}, \phi_{hp}) = \langle \mathbf{u}_{hp}, \phi_{hp} \rangle$ , and  $a(\mathbf{u}_{hp}, \phi_{hp}) = \langle \nabla_t \times \mathbf{u}_{hp}, \nabla_t \times \phi_{hp} \rangle$ . We further assert that the domain  $\Omega \subset \mathbb{R}^2$  is terminated by the Dirichlet boundary condition  $\mathbf{n} \times \mathbf{u}_{hp} = 0$  on  $\partial\Omega$ . Finally,  $\mathbf{u}_{hp}$  is purely transversal.

While not exclusively applicable to eigenvalue problems with singularities, we study the approach for a 2-D cross-section of an L-shaped waveguide, shown in Fig. 5.2(a), which features

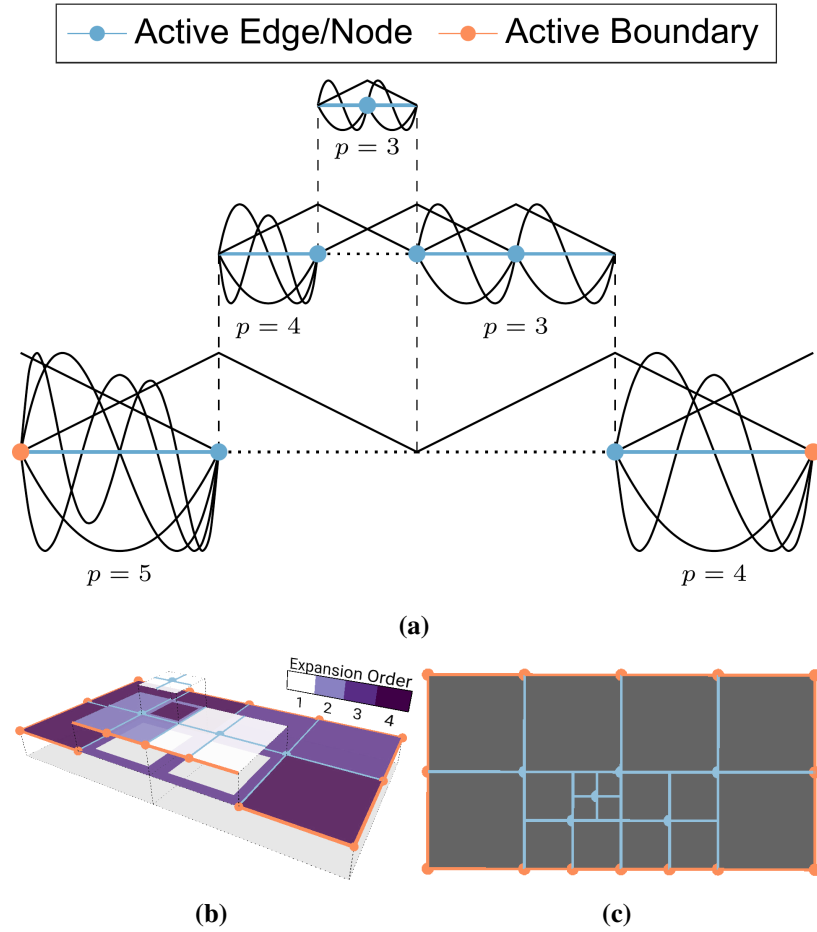


**Figure 5.1:** The RBS  $hp$ -refinement activation and deactivation procedure. (a) The depiction of the process in 1-D. (b) The depiction of the process in 2-D. (c) An overhead perspective of the distribution of  $h$ -refinements applied in the 2-D example.

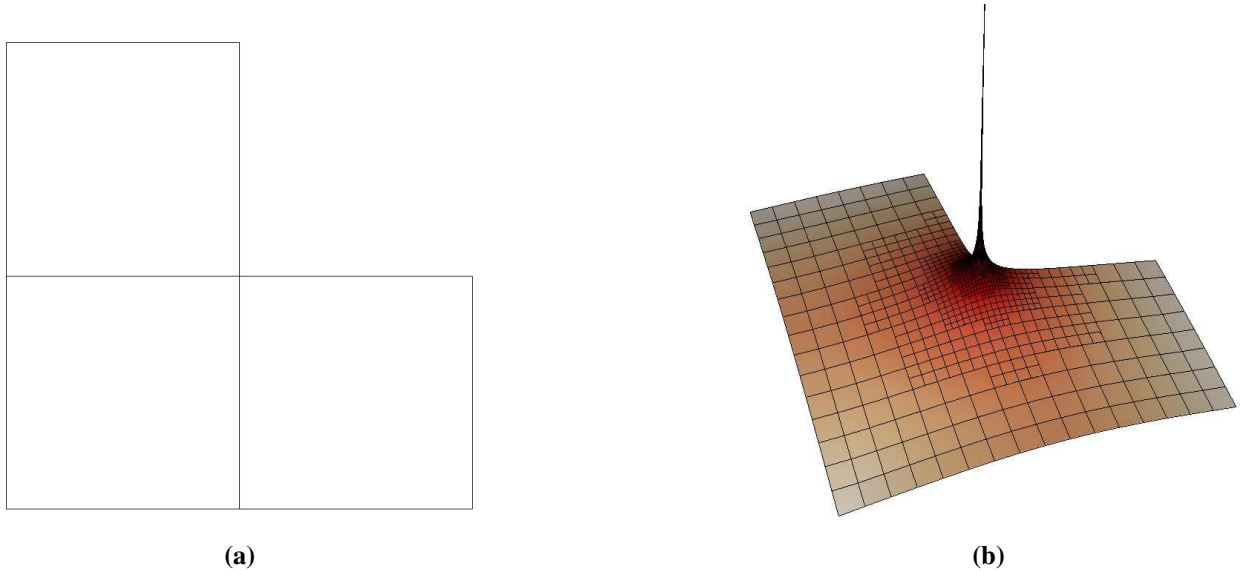


**Figure 5.2:** The model and problem under study. (a) The initial discretization for the L-shaped domain, composed of three unit squares. (b) The field magnitude of the first eigenfunction, illustrating the singularity at the reentrant corner.

many singular eigenfunctions, to demonstrate the capability to achieve exponential convergence in the presence of solution irregularity. We focus our analysis on the convergence of the smallest eigenvalue to an accurate numerical computation [3] of the benchmark problem originally proposed by [83]. The eigenfunction associated with this eigenvalue exhibits a singularity in the field at the reentrant corner, as seen in Fig. 5.2(b).

Following the procedure outlined in Section II, the initial discretization is successively refined about the reentrant corner. New refinement layers are inserted in groups with  $p = 1$  and the expansion orders of each pre-existing cell are increased by one each iteration, resulting in an emphasis on  $h$ -refinements closer to the reentrant corner and an emphasis on  $p$ -refinements away from the reentrant corner. We note that this illustrative *a priori* refinement strategy is neither optimal nor adaptive. Adaptive strategies, such as in [3], may be applied in place of the illustrative refinement approach presented in this manuscript. A collection of discretizations with  $h$ -refinements targeting the reentrant corner (from  $L = 0$  to  $L = 8$  refinement levels) and global (i.e., uniform) increments in  $p$  serves as the comparison approach.

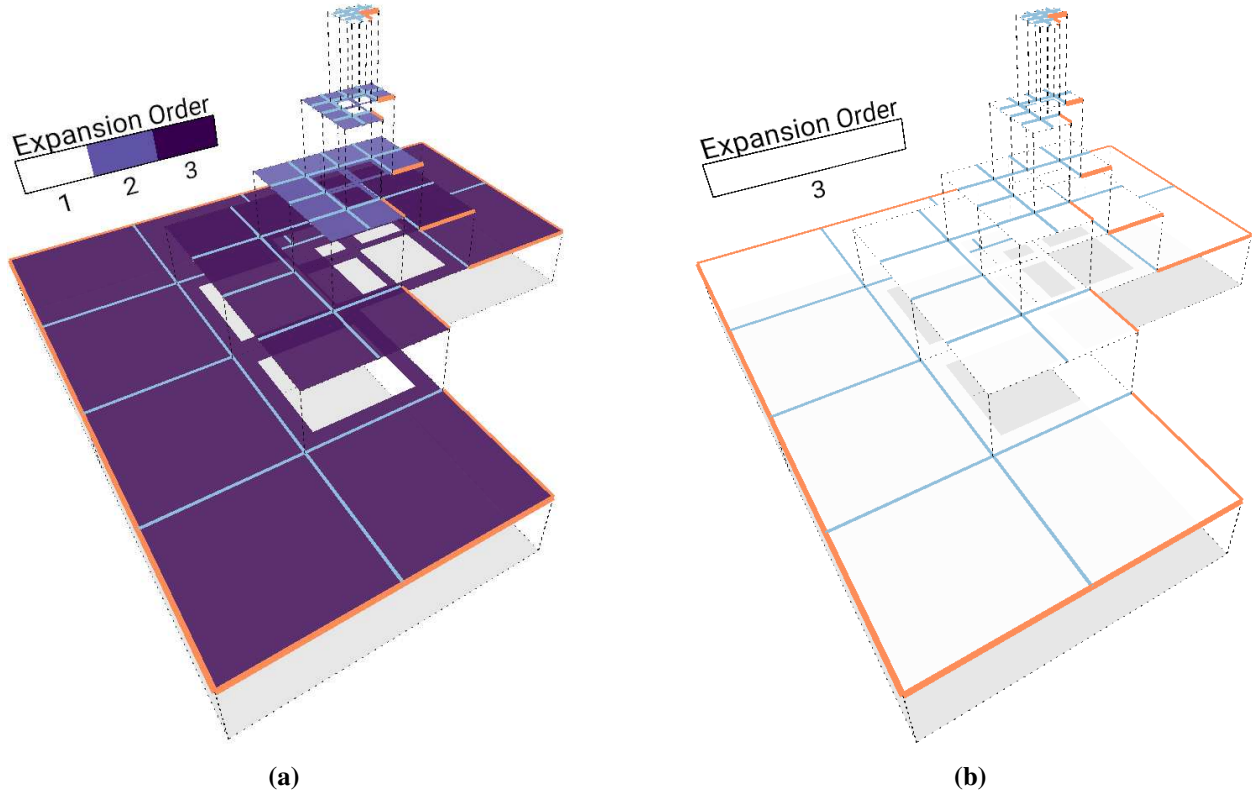
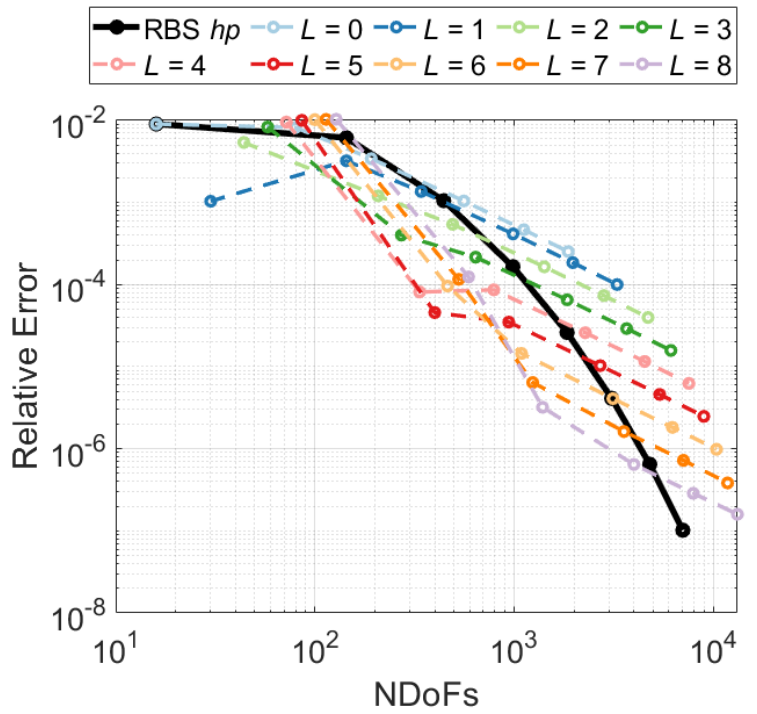


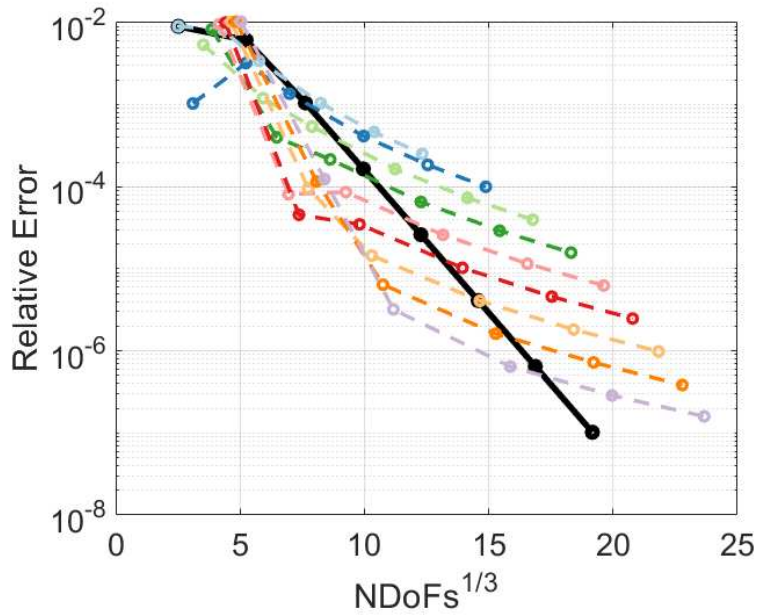
**Figure 5.3:** Example discretizations for the RBS  $hp$ -method and the selectively  $h$ -refined comparison method with uniform  $p$ . (a) The RBS  $hp$ -method discretization with maximum and minimum expansion orders of three and one, respectively. (b) The RBS  $h$ -method with a uniform expansion order of three. The two discretizations have  $L = 5$  refinement levels.

Example discretizations from each approach with five refinement layers are illustrated in Fig. 5.3. Fig. 5.3(a) depicts the progression from third-order field expansion to first-order while undergoing simultaneous  $h$ -refinements and Fig. 5.3(b) features the same level of  $h$ -refinement with homogeneous third-order field expansion.

Fig. 5.4 shows the convergence results for the first eigenvalue with the two approaches to refinement. RBS  $hp$ -refinement achieves exponential convergence while the successively  $p$ -refined discretizations at various levels of  $h$ -refinement ( $L = 0$  to  $L = 8$ ) provide only algebraic convergence. The linear trend with respect to  $\text{NDoFs}^{1/3}$  as in Fig. 5.4(b) indicates the strong consistency of the exponential convergence.



(a)



(b)

**Figure 5.4:** Convergence of the first eigenvalue for the RBS  $hp$ -method and the comparison approach with  $h$ -refinement levels from  $L = 0$  to  $L = 8$  and increasing uniform expansion orders. (a) Double logarithmic representation. (b) log-cube-root representation.

## 5.4 Conclusion

We have demonstrated the capability to achieve exponential convergence through an RBS  $hp$ -method in CEM. At the cost of reducing sparsity in FEM applications, the significant reduction in implementation complexity facilitates straightforward adoption of  $hp$ -refinement techniques with arbitrary levels of refinement.

When applied to the computation of the eigenvalue associated with a singular eigenfunction for  $H(\text{curl})$ -conforming elements, the method delivers perfect exponential convergence while enforcing the tangential continuity requirements by construction rather than through constraint equations. Finally, the entire procedure directly applies to enforcement of normal continuity when  $H(\text{div})$ -conforming elements are required and also extends to 3-D applications easily.

# Conclusion

This dissertation presented the development of several strategies to enhance the utility of numerical methods in applied mathematics, with a particular focus on CEM. Driven by the simultaneous needs for simulations of high-quality, high-efficiency, and high-confidence (including by assessing effects due to uncertainties), we pursued a collection of advancements in leveraging goal-oriented error estimates and goal-oriented uncertainty quantification. Given the expanding desire and requirement for high-fidelity numerical simulations of systems governed by realistic PDEs or IEs, the dictation of intelligent, mixed-order refinement instructions can yield rapid improvements in applicability and accuracy without overwhelming computational resources and exceeding time constraints. We proposed refinement methodologies based on error prediction to tailor discretizations for user-defined goal functionals, which, in addition to the provision of true error estimates (as opposed to just indicators), deliver exponential rates of convergence even in the presence of singular solutions. Moreover, by reusing the underlying computations in the error estimation, we demonstrated how uncertainty quantification may be performed for scattering problems in CEM with significant computation time advantages by reducing the need for expensive, full model solves. Finally, to support the objectives and developments of the dissertation, we presented an alternative paradigm to conducting local refinements, both spatially (i.e.,  $h$ -refinements) and in terms of function spaces (i.e.,  $p$ -refinements), that permits exponential convergence and arbitrary levels of refinements with lightweight implementation requirements.

In Chapter 2, we introduced a comprehensive approach to guiding adaptive mesh refinements for SIE problems. While less studied in many areas than analogous FEM-based methods, BEM or MoM discretizations can provide significant computational advantages. By focusing on the EFIE and the popular PMCHWT formulation of the EFIE-MFIE, we proposed an adaptive refinement mechanism enhanced by true error estimates to rapidly refine discretizations of SIE problems, including those of extremely poor initial quality. We emphasized customizable and practical scattering QoIs (including a linearized RCS QoI) in our study, producing discretizations that closely match desired QoI relative

errors. Furthermore, by introducing a refinement scheme based on error prediction, the dependence of the number of iterations on the desired accuracy may be significantly reduced. As such, the proposed method accelerates refinement procedures for poor initial discretizations, even when targeting extremely high accuracy. A second consequence of the approach, our method encourages equilibrated error contribution estimates, reducing the variation in error contribution estimates throughout the mesh, and therefore develops discretizations of higher efficiency and quality. Finally, the furnishing of true error estimates, as opposed to simple error or refinement indicators alone, facilitates greater confidence in the accuracy of simulation results and, overall, reduces the need for expert-user intervention.

In Chapter 3, we proposed an error prediction and optimization refinement approach to guide coarse initial discretizations to high accuracy. As an excellent benchmark problem and model, we studied the Maxwell eigenvalue problem for a challenging waveguide that supports eigenfunctions of varying regularity, from smooth to singular. Once again relying on goal-oriented error estimation and automated selection of refinement instructions, we performed  $hp$ -refinement for a collection of nine eigenpairs, targeting the accuracy of the eigenvalue in each eigenpair. We proposed a pair of objective functions for conducting refinement and coarsening optimally at each iteration and with consideration for differing local basis function orders. A second goal of this work, we confirmed and improved the results of previous numerical reference values and introduced new ones with the hope of supporting future developments and comparisons in adaptive  $hp$ -refinement research. Overall, we demonstrated that exploiting the enriched solution employed in computing the DWR expression for smoothness estimation yields significantly improved convergence behavior with respect to increasing the number of degrees of freedom. This advantage was particularly important for higher-order modes, which were missing from previous benchmarks, where smoothness estimation of the standard forward solution overestimated the need for  $h$ -refinement and therefore reduced per DoF efficiency.

In Chapter 4, we demonstrated how the adjoint solution, a key element to the adaptive error control methods proposed in the preceding chapters, may be reused for uncertainty quantification

applications in CEM. According to the HOPS methodology, local sensitivity information, namely gradients of the QoI with respect to the uncertain parameters, may be readily computed and applied to construct surrogate responses. For parameter spaces of a single dimension, the approach maintains the efficiency of traditional forward sensitivity analysis methods, with the added benefit that the adjoint solution may be available in advance due to a preceding refinement step. For higher dimensional parameter spaces, however, the adjoint approach delivers significant computational advantages, requiring only the solutions to the forward problem and the adjoint problem, regardless of the number of varying parameters (as opposed to an additional solve for each parameter). The surrogate models generated via HOPS circumvent the need to conduct full model solves for each sample of the random parameters as required with traditional Monte Carlo simulations, avoiding the significant computational expense and converting a problem largely of statistical error (the number of samples that can be computed under a time constraint) to deterministic error (how closely the surrogate matches the response surface of the QoI). With a focus on scattering QoIs, we studied FEM discretizations of the curl-curl wave equation assuming random variation in the material parameters of a spherical scatterer. To illustrate the predictive capabilities of the approach for scattering QoIs and various levels of uncertainty, we examined low- to high-dimensional parameter spaces. In each case, the disconnection of the gradient computation from the number of uncertain parameters yielded significant increases in the computational efficiency while still providing high accuracy. Moreover, we illustrated how a degree of probabilistic tuning may be conveniently inserted in the HOPS procedure through  $k$ -means clustering. Overall, the HOPS approach is highly adaptable and versatile for UQ applications in CEM and beyond. With the continually growing need for effective and efficient UQ methods, adjoint-based approaches may continue to yield significant opportunities for theoretical and algorithmic advances.

In Chapter 5, we introduced an alternative approach to conducting  $hp$ -refinements in CEM. By conducting refinements through superposition as opposed to replacement,  $hp$ -refinements may be executed with ease. This framework, furthermore, supports arbitrary levels of refinements automatically, which contrasts the 1-irregularity requirements imposed by typical refinement-by-

replacement implementations due to the high implementation complexity. Most importantly, the proposed approach also supports exponential rates of convergence with respect to the number of degrees of freedom in CEM, including for the refinement of eigenvalue QoIs associated with singular eigenfunctions. While the numerical demonstrations focused on  $H(\text{curl})$ -conforming elements, the approach applies immediately to  $H(\text{div})$ -conforming elements where normal continuity is required in place of tangential continuity. In addition to straightforward extensions to 3-D problems, the method shows significant promise for applications in the MoM and BEM for refining and representing discretizations of SIE problems. Finally, the reduced implementation cost required to support  $hp$ -refinements provided by the method encourages the incorporation of state-of-the-art techniques in adaptive error control in existing CEM projects and practical applications.

## References

- [1] J. J. Harmon and B. M. Notaroš, “Accelerated adaptive error control and refinement for SIE scattering problems,” *IEEE Transactions on Antennas and Propagation*, 2022, In Press.
- [2] J. J. Harmon, C. Key, D. Estep, T. Butler, and B. M. Notaroš, “Adjoint-based accelerated adaptive refinement in frequency domain 3-D finite element method scattering problems,” *IEEE Transactions on Antennas and Propagation*, vol. 69, no. 2, pp. 940–949, 2021.
- [3] J. J. Harmon and B. M. Notaroš, “Adaptive hp-refinement for 2-D Maxwell eigenvalue problems: Method and benchmarks,” *IEEE Transactions on Antennas and Propagation*, 2022, In Press.
- [4] D. Arndt, W. Bangerth, B. Blais, T. C. Clevenger, M. Fehling, A. V. Grayver, T. Heister, L. Heltai, M. Kronbichler, M. Maier, P. Munch, J.-P. Pelteret, R. Rastak, I. Thomas, B. Turcksin, Z. Wang, and D. Wells, “The deal.II library, version 9.2,” *Journal of Numerical Mathematics*, vol. 28, no. 3, pp. 131–146, 2020. [Online]. Available: <https://dealii.org/deal92-preprint.pdf>
- [5] J. J. Harmon, C. Key, D. Estep, T. Butler, and B. M. Notaroš, “Adjoint sensitivity analysis for uncertain material parameters in frequency-domain 3-d FEM,” *IEEE Transactions on Antennas and Propagation*, vol. 69, no. 10, pp. 6669–6679, 2021.
- [6] J. Harmon, J. Corrado, and B. Notaros, “A Refinement-by-Superposition hp-Method for  $H(\text{curl})$ - and  $H(\text{div})$ -Conforming Discretizations,” *TechRxiv*, 6 2021. [Online]. Available: [https://www.techrxiv.org/articles/preprint/A\\_Refinement-by-Superposition\\_hp-Method\\_for\\_H\\_curl\\_-\\_and\\_H\\_div\\_-Conforming\\_Discretizations/14807895](https://www.techrxiv.org/articles/preprint/A_Refinement-by-Superposition_hp-Method_for_H_curl_-_and_H_div_-Conforming_Discretizations/14807895)
- [7] J. Corrado, J. J. Harmon, and B. M. Notaroš, “A refinement-by-superposition approach to fully anisotropic hp-refinement for improved efficiency in cem,” 2021. [Online]. Avail-

- able: [https://www.techrxiv.org/articles/preprint/A\\_Refinement-by-Superposition\\_Approach\\_to\\_Fully\\_Anisotropic\\_hp-Refinement\\_for\\_Improved\\_Efficiency\\_in\\_CEM/16695163/1](https://www.techrxiv.org/articles/preprint/A_Refinement-by-Superposition_Approach_to_Fully_Anisotropic_hp-Refinement_for_Improved_Efficiency_in_CEM/16695163/1)
- [8] J. Corrado, J. Harmon, B. Notaros, and M. M. Ilić, “FEM\_2D: A Rust Package for 2D Finite Element Method Computations with Extensive Support for hp-refinement,” *TechRxiv*, 5 2022. [Online]. Available: [https://www.techrxiv.org/articles/preprint/FEM\\_2D\\_A\\_Rust\\_Package\\_for\\_2D\\_Finite\\_Element\\_Method\\_Computations\\_with\\_Extensive\\_Support\\_for\\_hp-refinement/19166339](https://www.techrxiv.org/articles/preprint/FEM_2D_A_Rust_Package_for_2D_Finite_Element_Method_Computations_with_Extensive_Support_for_hp-refinement/19166339)
- [9] J. Corrado, J. Harmon, and B. Notaros, “An Adaptive Anisotropic hp-Refinement Algorithm for the 2D Maxwell Eigenvalue Problem,” *TechRxiv*, 4 2022. [Online]. Available: [https://www.techrxiv.org/articles/preprint/An\\_Adaptive\\_Anisotropic\\_hp-Refinement\\_Algorithm\\_for\\_the\\_2D\\_Maxwell\\_Eigenvalue\\_Problem/19636770](https://www.techrxiv.org/articles/preprint/An_Adaptive_Anisotropic_hp-Refinement_Algorithm_for_the_2D_Maxwell_Eigenvalue_Problem/19636770)
- [10] M. Djordjevic and B. M. Notaros, “Double higher order method of moments for surface integral equation modeling of metallic and dielectric antennas and scatterers,” *IEEE Transactions on Antennas and Propagation*, vol. 52, no. 8, pp. 2118–2129, Aug 2004.
- [11] B. M. Kolundzija and A. Djordjevic, *Electromagnetic Modeling of Composite Metallic and Dielectric Structures*. Norwood: Artech House, 2002.
- [12] B. M. Kolundzija, “Electromagnetic modeling of composite metallic and dielectric structures,” *IEEE Transactions on Microwave Theory and Techniques*, vol. 47, no. 7, pp. 1021–1032, 1999.
- [13] L. F. Demkowicz, “Fully automatic hp-adaptivity for Maxwell’s equations,” *Computer Methods in Applied Mechanics and Engineering*, vol. 194, no. 2, pp. 605–624, 2005.
- [14] D. Pardo and L. F. Demkowicz, “Integration of hp-adaptivity and a two-grid solver for elliptic problems,” *Computer Methods in Applied Mechanics and Engineering*, vol. 195, no. 7, pp. 674–710, 2006.

- [15] L. Demkowicz, *Computing with hp Finite Elements I. One- and Two-Dimensional Elliptic and Maxwell Problems*. Chapman & Hall/CRC Press, Taylor and Francis, 2007.
- [16] M. M. Botha and D. B. Davidson, “An explicit a posteriori error indicator for electromagnetic, finite element-boundary integral analysis,” *IEEE Transactions on Antennas and Propagation*, vol. 53, no. 11, pp. 3717–3725, Nov 2005.
- [17] L. E. García-Castillo, D. Pardo, I. Gómez-Revuelto, and L. F. Demkowicz, “A two-dimensional self-adaptive hp finite element method for the characterization of waveguide discontinuities. Part I: Energy-norm based automatic hp-adaptivity,” *Computer Methods in Applied Mechanics and Engineering*, vol. 196, no. 49, pp. 4823–4852, 2007.
- [18] I. Gomez-Revuelto, L. E. Garcia-Castillo, S. Llorente-Romano, and D. Pardo, “A three-dimensional self-adaptive hp finite element method for the characterization of waveguide discontinuities,” *Computer Methods in Applied Mechanics and Engineering*, vol. 249-252, pp. 62–74, 2012.
- [19] S. M. Schnepf, “Error-driven dynamical hp-meshes with the discontinuous galerkin method for three-dimensional wave propagation problems,” *Journal of Computational and Applied Mathematics*, vol. 270, pp. 353–368, 2014.
- [20] P. Monk and E. Süli, “The adaptive computation of far-field patterns by a posteriori error estimation of linear functionals,” *SIAM Journal on Numerical Analysis*, vol. 36, no. 1, pp. 251–274, 1998.
- [21] P. Monk, “A posteriori error indicators for Maxwell’s equations,” *Journal of Computational and Applied Mathematics*, vol. 100, no. 2, pp. 173–190, 1998.
- [22] L. E. G. Castillo, D. Pardo, and L. F. Demkowicz, “Fully automatic hp adaptivity for electromagnetics, application to the analysis of H-plane and E-plane rectangular waveguide discontinuities,” in *2007 IEEE/MTT-S International Microwave Symposium*, 2007, pp. 285–288.

- [23] L. E. Garcia-Castillo, D. Pardo, and L. F. Demkowicz, “Energy-norm-based and goal-oriented automatic  $hp$  adaptivity for electromagnetics: Application to waveguide discontinuities,” *IEEE Transactions on Microwave Theory and Techniques*, vol. 56, no. 12, pp. 3039–3049, 2008.
- [24] D. Pardo, L. E. García-Castillo, L. F. Demkowicz, and C. Torres-Verdín, “A two-dimensional self-adaptive  $hp$  finite element method for the characterization of waveguide discontinuities. Part II: Goal-oriented  $hp$ -adaptivity,” *Computer Methods in Applied Mechanics and Engineering*, vol. 196, no. 49, pp. 4811–4822, 2007.
- [25] D. Pardo, L. Demkowicz, C. Torres-Verdín, and M. Paszynski, “A self-adaptive goal-oriented  $hp$ -finite element method with electromagnetic applications. Part II: Electrodynamics,” *Computer Methods in Applied Mechanics and Engineering*, vol. 196, no. 37, pp. 3585–3597, 2007.
- [26] A. Zdunek and W. Rachowicz, “A goal-oriented  $hp$ -adaptive finite element approach to radar scattering problems,” *Computer Methods in Applied Mechanics and Engineering*, vol. 194, no. 2, pp. 657–674, 2005.
- [27] C. Key, A. P. Smull, D. Estep, T. Butler, and B. M. Notaroš, “A posteriori error estimation and adaptive discretization refinement using adjoint methods in CEM: A study with a 1-d higher order fem scattering example,” *IEEE Transactions on Antennas and Propagation*, vol. 68, no. 5, pp. 3791–3806, 2020.
- [28] W. Bangerth and R. Rannacher, *Adaptive Finite Element Methods for Differential Equations*. Birkhauser Basel, 2003.
- [29] G. I. Marchuk, *Adjoint Equations and Analysis of Complex Systems*. Netherlands: Netherlands: Kluwer Academic Publishers, 1995.

- [30] D. Estep, M. Holst, and D. Mikulencak, "Accounting for stability: A posteriori error estimates based on residuals and variational analysis," *Communications in Numerical Methods in Engineering*, vol. 18, no. 7, pp. 15–30, 11 2001.
- [31] M. H. Bakr and N. K. Nikolova, "An adjoint variable method for time domain TLM with fixed structured grids," in *IEEE MTT-S International Microwave Symposium Digest, 2003*, vol. 2, June 2003, pp. 1121–1124 vol.2.
- [32] N. K. Nikolova, H. W. Tam, and M. H. Bakr, "Sensitivity analysis with the FDTD method on structured grids," *IEEE Transactions on Microwave Theory and Techniques*, vol. 52, no. 4, pp. 1207–1216, April 2004.
- [33] S. M. Ali, N. K. Nikolova, and M. H. Bakr, "Central adjoint variable method for sensitivity analysis with structured grid electromagnetic solvers," *IEEE Transactions on Magnetics*, vol. 40, no. 4, pp. 1969–1971, July 2004.
- [34] Y. Zhang, M. H. Negm, and M. H. Bakr, "An adjoint variable method for wideband second-order sensitivity analysis through FDTD," *IEEE Transactions on Antennas and Propagation*, vol. 64, no. 2, pp. 675–686, 2016.
- [35] M. H. Bakr, *Nonlinear Optimization in Electrical Engineering with Applications in MATLAB*. IET, September 2013.
- [36] S. Koziel and A. Bekasiewicz, "Fast EM-driven size reduction of antenna structures by means of adjoint sensitivities and trust regions," *IEEE Antennas and Wireless Propagation Letters*, vol. 14, pp. 1681–1684, 2015.
- [37] E. Ubeda and J. M. Rius, "Novel monopolar MFIE MoM-discretization for the scattering analysis of small objects," *IEEE Transactions on Antennas and Propagation*, vol. 54, no. 1, pp. 50–57, 2006.

- [38] E. Ubeda, J. M. Rius, and A. Heldring, “Nonconforming discretization of the electric-field integral equation for closed perfectly conducting objects,” *IEEE Transactions on Antennas and Propagation*, vol. 62, no. 8, pp. 4171–4186, 2014.
- [39] M. M. Bibby and A. F. Peterson, “On the use of overdetermined systems in the adaptive numerical solution of integral equations,” *IEEE Transactions on Antennas and Propagation*, vol. 53, no. 7, pp. 2267–2273, 2005.
- [40] U. Saeed and A. F. Peterson, “Explicit local error estimators for electromagnetic integral equations,” *IEEE Transactions on Antennas and Propagation*, vol. 63, no. 3, pp. 1159–1163, 2015.
- [41] S. K. Kim and A. F. Peterson, “Evaluation of local error estimators for the RWG-based EFIE,” *IEEE Transactions on Antennas and Propagation*, vol. 66, no. 2, pp. 819–826, 2018.
- [42] ———, “Adaptive h-refinement for the RWG-based EFIE,” *IEEE Journal on Multiscale and Multiphysics Computational Techniques*, vol. 3, pp. 58–65, 2018.
- [43] S. K. Kim, “Error estimation and adaptive refinement technique in the method of moments,” Ph.D. dissertation, Georgia Institute of Technology, 2017.
- [44] J. A. Tobon Vasquez, Z. Peng, J. F. Lee, G. Vecchi, and F. Vipiana, “Automatic localized non-conformal mesh refinement for surface integral equations,” *IEEE Transactions on Antennas and Propagation*, vol. 68, no. 2, pp. 967–975, 2020.
- [45] P. I. Cilliers and M. M. Botha, “Goal-oriented error estimation for the method of moments to compute antenna impedance,” *IEEE Antennas and Wireless Propagation Letters*, vol. 19, no. 6, pp. 997–1001, 2020.
- [46] A. Poggio and E. Miller, “Integral equation solutions of three-dimensional scattering problems,” in *Computer Techniques for Electromagnetics*, ser. International Series of Monographs in Electrical Engineering. Pergamon, 1973, pp. 159–264.

- [47] Y. Chang and R. Harrington, "A surface formulation for characteristic modes of material bodies," *IEEE Transactions on Antennas and Propagation*, vol. 25, no. 6, pp. 789–795, 1977.
- [48] T. Wu and L. L. Tsai, "Scattering from arbitrarily-shaped lossy dielectric bodies of revolution," *Radio Science*, vol. 12, no. 5, pp. 709–718, 1977.
- [49] A. Peterson, D. Wilton, and R. Jorgenson, "Variational nature of galerkin and non-galerkin moment method solutions," *IEEE Transactions on Antennas and Propagation*, vol. 44, no. 4, pp. 500–503, 1996.
- [50] K. Chen, "Error equidistribution and mesh adaptation," *SIAM Journal on Scientific Computing*, vol. 15, no. 4, pp. 798–818, 1994.
- [51] A. Bepalov and N. Heuer, "Natural hp-BEM for the electric field integral equation with singular solutions," 2010.
- [52] P. Houston, B. Senior, and E. Süli, "Sobolev regularity estimation for hp-adaptive finite element methods," *Numerical Mathematics and Advanced Applications*, pp. 619–644, 2003.
- [53] I. Babuška and M. Suri, "The p and h-p versions of the finite element method, basic principles and properties," *SIAM Review*, vol. 36, no. 4, pp. 578–632, 1994.
- [54] B. Guo and I. Babuška, "The h-p version of the finite element method," *Computational Mechanics*, vol. 1, no. 1, pp. 21–41, 1986.
- [55] W. Dörfler, "A convergent adaptive algorithm for Poisson's equation," *SIAM Journal on Numerical Analysis*, vol. 33, no. 3, pp. 1106–1124, 1996.
- [56] A. Woo, H. Wang, M. Schuh, and M. Sanders, "EM programmer's notebook-benchmark radar targets for the validation of computational electromagnetics programs," *IEEE Antennas and Propagation Magazine*, vol. 35, no. 1, pp. 84–89, 1993.
- [57] K. Eriksson, D. Estep, P. Hansbo, and C. Johnson, "Introduction to adaptive methods for differential equations," *Acta Numerica*, vol. 4, p. 105–158, 1995.

- [58] I. Babuška and M. R. Dorr, “Error estimates for the combined h and p versions of the finite element method,” *Numerische Mathematik*, vol. 37, pp. 257–277, 06 1981.
- [59] W. Gui and I. Babuška, “The h, p and h-p versions of the finite element method in 1 dimension, Part I.” *Numerische Mathematik*, vol. 49, no. 6, pp. 577–612, Nov 1986.
- [60] W. Gui and I. Babuška, “The h, p and h-p versions of the finite element method in 1 dimension, Part II.” *Numerische Mathematik*, vol. 49, no. 6, pp. 613–657, Nov 1986.
- [61] W. Gui and I. Babuška, “The h, p and h-p versions of the finite element method in 1 dimension, Part III.” *Numerische Mathematik*, vol. 49, no. 6, pp. 659–683, Nov 1986.
- [62] I. Babuška and E. Rank, “An expert-system-like feedback approach in the hp-version of the finite element method,” *Finite Elements in Analysis and Design*, vol. 3, no. 2, pp. 127–147, 1987.
- [63] W. Bangerth and O. Kayser-Herold, “Data structures and requirements for hp finite element software,” *ACM Trans. Math. Softw.*, vol. 36, no. 1, Mar. 2009.
- [64] D. Arndt, W. Bangerth, D. Davydov, T. Heister, L. Heltai, M. Kronbichler, M. Maier, J.-P. Pelteret, B. Turcksin, and D. Wells, “The deal.II finite element library: Design, features, and insights,” *Computers & Mathematics with Applications*, vol. 81, pp. 407–422, 2021. [Online]. Available: <https://arxiv.org/abs/1910.13247>
- [65] F. Kikuchi, “On a discrete compactness property for the Nedelec finite elements,” *J. Fac. Sci. Univ. Tokyo, Sect. IA. Math.*, vol. 36, pp. 479–490, 1989.
- [66] D. Boffi, M. Costabel, M. Dauge, L. F. Demkowicz, and R. Hiptmair, “Discrete compactness for the p-version of discrete differential forms,” *SIAM Journal on Numerical Analysis*, vol. 49, no. 1, pp. 135–158, 2011.

- [67] D. Boffi, M. Costabel, M. Dauge, and L. F. Demkowicz, “Discrete compactness for the hp version of rectangular edge finite elements,” *SIAM Journal on Numerical Analysis*, vol. 44, no. 3, pp. 979–1004, 2006.
- [68] M. M. Ilic, A. Z. Ilic, and B. M. Notaros, “Efficient large-domain 2-d fem solution of arbitrary waveguides using p-refinement on generalized quadrilaterals,” *IEEE Transactions on Microwave Theory and Techniques*, vol. 53, no. 4, pp. 1377–1383, April 2005.
- [69] D. Boffi and L. Gastaldi, “Adaptive finite element method for the Maxwell eigenvalue problem,” *SIAM Journal on Numerical Analysis*, vol. 57, 04 2018.
- [70] J. Coyle and P. Ledger, “Evidence of exponential convergence in the computation of Maxwell eigenvalues,” *Computer Methods in Applied Mechanics and Engineering*, vol. 194, pp. 587–604, 02 2005.
- [71] M. Ainsworth, J. Coyle, P. D. Ledger, and K. Morgan, “Computing Maxwell eigenvalues by using higher order edge elements in three dimensions,” *IEEE Transactions on Magnetics*, vol. 39, no. 5, pp. 2149–2153, 2003.
- [72] M. Bürg, “Convergence of an automatic hp-adaptive finite element strategy for Maxwell’s equations,” *Applied Numerical Mathematics*, vol. 72, pp. 188–204, 10 2013.
- [73] C. Mavriplis, “Adaptive mesh strategies for the spectral element method,” *Computer Methods in Applied Mechanics and Engineering*, vol. 116, no. 1, pp. 77–86, 1994.
- [74] M. Fehling, “Algorithms for massively parallel generic hp-adaptive finite element methods,” Ph.D. dissertation, Univ. Wuppertal, 2020.
- [75] P. Arbenz, R. Geus, and S. Adam, “Solving Maxwell eigenvalue problems for accelerating cavities,” *Phys. Rev. ST Accel. Beams*, pp. 1–10, 2001.

- [76] L. Vardapetyan, L. F. Demkowicz, and D. P. Neikirk, “hp-vector finite element method for eigenmode analysis of waveguides,” *Computer Methods in Applied Mechanics and Engineering*, vol. 192, pp. 185–201, 01 2003.
- [77] V. Heuveline and R. Rannacher, “A posteriori error control for finite element approximations of elliptic eigenvalue problems,” *J. Adv. Comp. Math*, vol. 15, pp. 107–138, 2001.
- [78] L. E. García-Castillo, D. Pardo, I. Gómez-Revuelto, and L. F. Demkowicz, “A two-dimensional self-adaptive hp finite element method for the characterization of waveguide discontinuities. Part I: Energy-norm based automatic hp-adaptivity,” *Computer Methods in Applied Mechanics and Engineering*, vol. 196, no. 49, pp. 4823–4852, 2007.
- [79] T. Richter, “Parallel multigrid method for adaptive finite elements with application to 3d flow problems,” Ph.D. dissertation, University of Heidelberg, 2005.
- [80] W. Rachowicz, “An anisotropic h-type mesh-refinement strategy,” *Computer Methods in Applied Mechanics and Engineering*, vol. 109, no. 1, pp. 169–181, 1993.
- [81] T. Eibner and J. M. Melenk, “An adaptive strategy for hp-FEM based on testing for analyticity,” *Comput Mesh*, vol. 39, no. 39, pp. 575–595, 2007.
- [82] W. Bangerth, C. Burstedde, T. Heister, and M. Kronbichler, “Algorithms and data structures for massively parallel generic adaptive finite element codes,” *ACM Trans. Math. Softw.*, vol. 38, no. 2, pp. 1–28, 2012.
- [83] M. Dauge, “Benchmark computations for maxwell equations for the approximation of highly singular solutions,” <https://perso.univ-rennes1.fr/monique.dauge/benchmax.html>, 2004.
- [84] J. C. Nédélec, “Mixed finite elements in  $\mathbb{R}^3$ ,” *Numerische Mathematik*, vol. 35, pp. 315–341, 1980.
- [85] H. Childs, E. Brugger, B. Whitlock, J. Meredith, S. Ahern, D. Pugmire, K. Biagas, M. Miller, C. Harrison, G. H. Weber, H. Krishnan, T. Fogal, A. Sanderson, C. Garth, E. W. Bethel,

- D. Camp, O. Rübel, M. Durant, J. M. Favre, and P. Navrátil, “VisIt: An End-User Tool For Visualizing and Analyzing Very Large Data,” in *High Performance Visualization—Enabling Extreme-Scale Scientific Insight*, Oct 2012, pp. 357–372.
- [86] M. Duruflé, “Benchmark computations for maxwell equations for the approximation of highly singular solutions,” <https://www.math.u-bordeaux.fr/~durufle/eigenvalue.php>, 2006.
- [87] D. Estep and D. Neckels, “Fast and reliable methods for determining the evolution of uncertain parameters in differential equations,” *J. Comput. Phys.*, vol. 213, no. 2, pp. 530–556, Apr. 2006.
- [88] D. Estep and D. Neckels, “Fast methods for determining the evolution of uncertain parameters in reaction-diffusion equations,” *Computer Methods in Applied Mechanics and Engineering*, vol. 196, pp. 3967–3979, 08 2007.
- [89] D. Neckels, “Variational methods for uncertainty quantification,” Ph.D. dissertation, Department of Mathematics, Colorado State University, Fort Collins, CO, 2005.
- [90] M. Swillam, M. Bakr, N. Nikolova, and X. Li, “Adjoint sensitivity analysis of dielectric discontinuities using FDTD,” *Electromagnetics*, vol. 27, 03 2007.
- [91] M. H. Bakr and N. K. Nikolova, “An adjoint variable method for time-domain transmission-line modeling with fixed structured grids,” *IEEE Transactions on Microwave Theory and Techniques*, vol. 52, no. 2, pp. 554–559, Feb 2004.
- [92] M. M. T. Maghrabi, M. H. Bakr, and S. Kumar, “Linear adjoint sensitivity analysis of the time-dependent schrödinger equation,” in *2019 International Applied Computational Electromagnetics Society Symposium (ACES)*, April 2019, pp. 1–2.
- [93] P. Garcia and J. P. Webb, “Optimization of planar devices by the finite element method,” *IEEE Transactions on Microwave Theory and Techniques*, vol. 38, no. 1, pp. 48–53, Jan 1990.

- [94] M. M. T. Maghrabi, M. H. Bakr, S. Kumar, A. Elsherbeni, and V. Demir, “FDTD-based adjoint sensitivity analysis of high frequency nonlinear structures,” *IEEE Transactions on Antennas and Propagation*, pp. 1–1, 2020.
- [95] Y. Zhang, O. S. Ahmed, and M. H. Bakr, “Wideband FDTD-based adjoint sensitivity analysis of dispersive electromagnetic structures,” *IEEE Transactions on Microwave Theory and Techniques*, vol. 62, no. 5, pp. 1122–1134, 2014.
- [96] O. Pankratov and A. Kuvshinov, “Inverse medium scattering for three-dimensional time harmonic Maxwell equations,” *Inverse Problems*, vol. 20, no. 2, pp. 1–7, 2004.
- [97] ———, “Applied mathematics in em studies with special emphasis on an uncertainty quantification and 3-d integral equation modelling,” *Surveys in Geophysics*, vol. 37, pp. 1295–1334, 2015.
- [98] D. Kamilis and N. Polydorides, “Uncertainty quantification for low-frequency, time-harmonic Maxwell equations with stochastic conductivity models,” *SIAM/ASA Journal on Uncertainty Quantification*, vol. 6, no. 4, pp. 1295–1334, 2018.
- [99] P. Ingelstrom and A. Bondeson, “Goal-oriented error estimation and h-adaptivity for Maxwell’s equations,” *Computer Methods in Applied Mechanics and Engineering*, vol. 192, pp. 2597–2616, 06 2003.
- [100] I. Gomez-Revuelto, L. Garcia-Castillo, and M. Palma, “Goal-oriented self-adaptive hp-strategies for finite element analysis of electromagnetic scattering and radiation problems,” *Progress In Electromagnetics Research*, vol. 125, pp. 459–482, 01 2012.
- [101] D. Estep, M. Larson, and W. RD, “Estimating the error of numerical solutions of systems of reaction–diffusion equations,” *Memoirs of the American Mathematical Society*, vol. 696, 07 2000.
- [102] R. Becker and R. Rannacher, “A feed-back approach to error control in finite element methods: Basic analysis and examples,” *East-West J. Numer. Math*, vol. 4, pp. 237–264, 1996.

- [103] R. Hartmann and P. Houston, “Adaptive discontinuous galerkin finite element methods for the compressible euler equations,” *Journal of Computational Physics*, vol. 183, no. 2, pp. 508–532, 2002.
- [104] R. Becker, “Mesh adaptation for stationary flow control,” *Journal of Mathematical Fluid Mechanics*, pp. 317–341, 11 2001.
- [105] Q. Wang, “Uncertainty quantification for unsteady fluid flow using adjoint-based approaches,” Ph.D. dissertation, Stanford University, 2009.
- [106] A. K. Alekseev, I. M. Navon, and M. E. Zelentsov, “The estimation of functional uncertainty using polynomial chaos and adjoint equations,” *International Journal for Numerical Methods in Fluids*, vol. 67, no. 3, pp. 328–341, 2011.
- [107] K. Maute, M. Nikbay, and C. Farhat, “Sensitivity analysis and design optimization of three-dimensional non-linear aeroelastic systems by the adjoint method,” *International Journal for Numerical Methods in Engineering*, vol. 56, no. 6, pp. 911–933, 2003.
- [108] K. C. Wang, Z. He, D. Z. Ding, and R. S. Chen, “Uncertainty scattering analysis of 3-D objects with varying shape based on method of moments,” *IEEE Transactions on Antennas and Propagation*, vol. 67, no. 4, pp. 2835–2840, 2019.
- [109] M. S. Gilbert and F. L. Teixeira, “A small-perturbation automatic-differentiation method for determining uncertainty in computational electromagnetics,” *IEEE Transactions on Antennas and Propagation*, vol. 60, no. 11, pp. 5305–5314, 2012.
- [110] R. L. Wagner, Jiming Song, and W. C. Chew, “Monte carlo simulation of electromagnetic scattering from two-dimensional random rough surfaces,” *IEEE Transactions on Antennas and Propagation*, vol. 45, no. 2, pp. 235–245, 1997.
- [111] Qin Li, Hou Chan, and Leung Tsang, “Monte carlo simulations of wave scattering from lossy dielectric random rough surfaces using the physics-based two-grid method and the

- canonical-grid method,” *IEEE Transactions on Antennas and Propagation*, vol. 47, no. 4, pp. 752–763, 1999.
- [112] N. Garcia and E. Stoll, “Monte carlo calculation for electromagnetic-wave scattering from random rough surfaces,” *Phys. Rev. Lett.*, vol. 52, pp. 1798–1801, 1984.
- [113] S. M. Smith and C. Furse, “Stochastic FDTD for analysis of statistical variation in electromagnetic fields,” *IEEE Transactions on Antennas and Propagation*, vol. 60, no. 7, pp. 3343–3350, 2012.
- [114] K. Masumnia-Bisheh, K. Forooraghi, and M. Ghaffari-Miab, “Electromagnetic uncertainty analysis using stochastic FDFD method,” *IEEE Transactions on Antennas and Propagation*, vol. 67, no. 5, pp. 3268–3277, 2019.
- [115] A. C. M. Austin and C. D. Sarris, “Efficient analysis of geometrical uncertainty in the fdtd method using polynomial chaos with application to microwave circuits,” *IEEE Transactions on Microwave Theory and Techniques*, vol. 61, no. 12, pp. 4293–4301, 2013.
- [116] R. S. Edwards, A. C. Marvin, and S. J. Porter, “Uncertainty analyses in the finite-difference time-domain method,” *IEEE Transactions on Electromagnetic Compatibility*, vol. 52, no. 1, pp. 155–163, 2010.
- [117] U. K. Khankhoje and S. Padhy, “Stochastic solutions to rough surface scattering using the finite element method,” *IEEE Transactions on Antennas and Propagation*, vol. 65, no. 8, pp. 4170–4180, 2017.
- [118] G. J. K. Tomy and K. J. Vinoy, “A fast polynomial chaos expansion for uncertainty quantification in stochastic electromagnetic problems,” *IEEE Antennas and Wireless Propagation Letters*, vol. 18, no. 10, pp. 2120–2124, 2019.
- [119] —, “Neumann-expansion-based fem for uncertainty quantification of permittivity variations,” *IEEE Antennas and Wireless Propagation Letters*, vol. 19, no. 4, pp. 561–565, 2020.

- [120] A. Kundu, S. Adhikari, and M. Friswell, “Transient response analysis of randomly parametrized finite element systems based on approximate balanced reduction,” *Computer Methods in Applied Mechanics and Engineering*, vol. 285, pp. 542–570, 2015.
- [121] J. Son and Y. Du, “Comparison of intrusive and nonintrusive polynomial chaos expansion based approaches for high dimensional parametric uncertainty quantification and propagation,” *Computers & Chemical Engineering*, vol. 134, no. 39, p. 106685, 2020.
- [122] M. Eldred, “Recent advances in non-intrusive polynomial chaos and stochastic collocation methods for uncertainty analysis and design,” in *50th AIAA/ASME/ASCE/AHS/ASC Structures, Structural Dynamics, and Materials Conference*, 05 2009, pp. 1–37.
- [123] D. Voyer, F. Musy, L. Nicolas, and R. Perrussel, “Comparison of methods for modeling uncertainties in a 2D hyperthermia problem,” *Progress In Electromagnetics Research B*, vol. 11, 2009.
- [124] M. A. Drissaoui, S. Lanteri, P. Leveque, F. Musy, L. Nicolas, R. Perrussel, and D. Voyer, “A stochastic collocation method combined with a reduced basis method to compute uncertainties in numerical dosimetry,” *IEEE Transactions on Magnetics*, vol. 48, no. 2, pp. 563–566, 2012.
- [125] J. Ochoa and A. Cangellaris, “Macro-modeling of electromagnetic domains exhibiting geometric and material uncertainty,” *Applied Computational Electromagnetics Society Journal*, vol. 27, pp. 80–87, 2012.
- [126] M. Gossye, G. Gordebeke, K. Y. Kapusuz, D. V. Ginste, , and H. Rogier, “Uncertainty quantification of waveguide dispersion using sparse grid stochastic testing,” *IEEE Transactions on Microwave Theory and Techniques*, vol. 68, no. 7, pp. 2485–2494, 2020.
- [127] D. Poljak, S. Šesnić, M. Cvetković, S. Lallechere, and K. El Khamlichi Drissi, “On some applications of stochastic collocation method in computational electromagnetics: Applications in ground penetrating radar, bioelectromagnetics, grounding systems and buried lines,”

- in *2016 24th International Conference on Software, Telecommunications and Computer Networks (SoftCOM)*, 2016, pp. 1–5.
- [128] J. Harmon and B. M. Notaroš, “The dual weighted residual and error estimation in double higher-order FEM,” in *2019 IEEE International Symposium on Antennas and Propagation and USNC-URSI Radio Science Meeting*, July 2019, pp. 771–772.
- [129] J. Harmon, C. Key, B. M. Notaroš, D. Estep, and T. Butler, “Adjoint-based uncertainty quantification in frequency-domain double higher-order FEM,” in *2019 International Applied Computational Electromagnetics Society Symposium (ACES)*, April 2019, pp. 1–2.
- [130] B. M. Notaroš, J. Harmon, C. Key, D. Estep, and T. Butler, “Error estimation and uncertainty quantification based on adjoint methods in computational electromagnetics,” in *2019 IEEE International Symposium on Antennas and Propagation and USNC-URSI Radio Science Meeting*, July 2019, pp. 221–222.
- [131] B. M. Notaroš, S. B. Manić, C. Key, J. Harmon, and D. Estep, “Overview of some advances in higher order frequency-domain CEM techniques,” in *2019 International Conference on Electromagnetics in Advanced Applications (ICEAA)*, Sep. 2019, pp. 1330–1333.
- [132] A. P. Smull, A. B. Manić, S. B. Manić, and B. M. Notaroš, “Anisotropic locally conformal perfectly matched layer for higher order curvilinear finite-element modeling,” *IEEE Transactions on Antennas and Propagation*, vol. 65, no. 12, pp. 7157–7165, Dec 2017.
- [133] M. M. Ilic and B. M. Notaros, “Higher order hierarchical curved hexahedral vector finite elements for electromagnetic modeling,” *IEEE Transactions on Microwave Theory and Techniques*, vol. 51, no. 3, pp. 1026–1033, March 2003.
- [134] —, “Higher order large-domain hierarchical fem technique for electromagnetic modeling using legendre basis functions on generalized hexahedra,” *Electromagnetics*, vol. 26, pp. 517–529, 10 2006.

- [135] B. M. Notaros, “Higher order frequency-domain computational electromagnetics,” *IEEE Transactions on Antennas and Propagation*, vol. 56, no. 8, pp. 2251–2276, Aug 2008.
- [136] P. D. Lax, *Functional Analysis*. New York, NY, USA: Wiley, 2002.
- [137] B. W. Silverman, *Density Estimation for Statistics and Data Analysis*. Boca Raton, FL, USA: Chapman & Hall/CRC, 1986.
- [138] J. Chang, M. S. Fabien, M. G. Knepley, and R. T. Mills, “Comparative study of finite element methods using the time-accuracy-size (TAS) spectrum analysis,” *SIAM Journal on Scientific Computing*, vol. 40, no. 6, pp. C779–C802, 2018.
- [139] S. Zaglmayr, “High order finite element methods for electromagnetic field computation,” Ph.D. dissertation, Institute for Numerical Mathematics, Johannes Kepler University Linz, Linz, Austria, 2006.
- [140] N. Zander, T. Bog, S. Kollmannsberger, D. Schillinger, and E. Rank, “Multi-level hp-adaptivity: High-order mesh adaptivity without the difficulties of constraining hanging nodes,” *Computational Mechanics*, vol. 55, no. 3, p. 499–517, 2015.
- [141] N. Zander, T. Bog, M. Elhaddad, F. F. S. Kollmannsberger, and E. Rank, “The multi-level hp-method for three-dimensional problems: Dynamically changing high-order mesh refinement with arbitrary hanging nodes,” *Computer Methods in Applied Mechanics and Engineering*, vol. 310, p. 252–277, 2016.
- [142] N. Zander, “High order finite element methods for electromagnetic field computation,” Ph.D. dissertation, Computational Engineering, Technische Universität München, München, Germany, 2016.
- [143] V. Darrigrand, D. Pardo, T. Chaumont-Frelet, I. Gómez-Revuelto, and L. E. Garcia-Castillo, “A painless automatic hp-adaptive strategy for elliptic problems,” *Finite Elements in Analysis and Design*, vol. 178, p. 103424, 2020.

- [144] M. M. Kostić and B. M. Kolundžija, “Maximally orthogonalized higher order bases over generalized wires, quadrilaterals, and hexahedra,” *IEEE Transactions on Antennas and Propagation*, vol. 61, no. 6, pp. 3135–3148, June 2013.
- [145] P. Di Stolfo, A. Schröder, N. Zander, and S. Kollmannsberger, “An easy treatment of hanging nodes in hp-finite elements,” *Finite Elements in Analysis and Design*, vol. 121, pp. 101–117, 2016.

# Appendix A

## Publications of the Candidate

### A.1 Journal Papers

1. J. J. Harmon and B. M. Notaroš, “Accelerated Adaptive Error Control and Refinement for SIE Scattering Problems,” *IEEE Transactions on Antennas and Propagation*, 2022, In Press, doi: 10.1109/TAP.2022.3177424.
2. J. J. Harmon and B. M. Notaroš, “Adaptive hp-Refinement for 2-D Maxwell Eigenvalue Problems: Method and Benchmarks,” *IEEE Transactions on Antennas and Propagation*, vol. 70, no. 6, pp. 4663-4673, June 2022, doi: 10.1109/TAP.2022.3145473.
3. J. Corrado, J. J. Harmon, and B. M. Notaroš, “An Adaptive Anisotropic hp-Refinement Algorithm for the 2D Maxwell Eigenvalue Problem,” *TechRxiv*, Apr. 2022, doi:10.36227/techrxiv.19636770.v1.
4. J. Corrado, J. J. Harmon, B. M. Notaroš, and M. M. Ilić, “FEM\_2D: A Rust Package for 2D Finite Element Method Computations with Extensive Support for hp-refinement,” *TechRxiv*, Feb. 2022, doi:10.36227/techrxiv.19166339.v2.
5. J. Corrado, J. J. Harmon, and B. M. Notaroš, “A Refinement-by-Superposition Approach to Fully Anisotropic hp-Refinement for Improved Efficiency in CEM,” *TechRxiv*, Oct. 2021, doi: 10.36227/techrxiv.16695163.v1.
6. J. J. Harmon, J. Corrado, and B. M. Notaroš, “A Refinement-by-Superposition hp-Method for H(curl)- and H(div)-Conforming Discretizations,” *TechRxiv*, Jun. 2021, doi: 10.36227/techrxiv.14807895.v1.

7. C. Key, J. J. Harmon, and B. M. Notaroš, “Correlations in a posteriori Error Trends for the Finite Element Method in the Presence of Changing Material Parameters,” *IEEE Antennas and Wireless Propagation Letters*, doi: 10.1109/LAWP.2021.3116167.
8. J. J. Harmon, C. Key, D. Estep, T. Butler, and B. M. Notaroš, “Adjoint Sensitivity Analysis for Uncertain Material Parameters in Frequency-Domain 3-D FEM,” *IEEE Transactions on Antennas and Propagation*, vol. 69, no. 10, pp. 6669-6679, Oct. 2021, doi: 10.1109/TAP.2021.3070059.
9. S. Kasdorf, B. Troksa, C. Key, J. J. Harmon, and B. M. Notaroš, “Advancing Accuracy of Shooting and Bouncing Rays Method for Ray-Tracing Propagation Modeling Based on Novel Approaches to Ray Cone Angle Calculation,” *IEEE Transactions on Antennas and Propagation*, vol. 69, no. 8, pp. 4808-4815, Aug. 2021, doi: 10.1109/TAP.2021.3060051.
10. J. J. Harmon, C. Key, D. Estep, T. Butler, and B. M. Notaroš, “Adjoint-Based Accelerated Adaptive Refinement in Frequency Domain 3-D Finite Element Method Scattering Problems,” *IEEE Transactions on Antennas and Propagation*, vol. 69, no. 2, pp. 940-949, Feb. 2021, doi: 10.1109/TAP.2020.3016162.
11. C. Key, J. J. Harmon, and B. M. Notaroš, “Discrete Surface Ricci Flow for General Surface Meshing in Computational Electromagnetics Using Iterative Adaptive Refinement,” *IEEE Transactions on Antennas and Propagation*, vol. 69, no. 1, pp. 332-346, Jan. 2021, doi: 10.1109/TAP.2020.3008657.

## **A.2 Peer-Reviewed Conference Papers and Abstracts**

1. J. J. Harmon, J. Corrado, and B. M. Notaroš, “On the Maxwell Eigenvalue Problem and Exponential Convergence Through Adaptive Error Control in the Presence of Singularities,” Proceedings of the 2022 USNC-URSI National Radio Science Meeting, January 4-8, 2022, Boulder, Colorado.

2. J. Corrado, J. J. Harmon, and B. M. Notaroš, "Efficiency Benefits of Anisotropic hp-Refinements for CEM," Proceedings of the 2022 USNC-URSI National Radio Science Meeting, January 4-8, 2022, Boulder, Colorado.
3. J. J. Harmon and B. M. Notaroš, "Adaptive Refinement for Scattered Field Quantities of Interest for the Coupled EFIE-MFIE," Proceedings of the 2021 IEEE International Symposium on Antennas and Propagation and USNC-URSI Radio Science Meeting (APS/URSI), December 4–10, 2021, Online Conference, pp. 205– 206.
4. J. J. Harmon and B. M. Notaroš, "Advances in Error Estimation and Uncertainty Quantification for Numerical Methods in CEM," Proceedings of the 2021 International Applied Computational Electromagnetics Society (ACES) Symposium – ACES2021, August 1–5, 2021, Online Conference.
5. J. J. Harmon and B. M. Notaroš, "Enhancing Adaptive Mesh Refinement Efficiency: Adjoint-Based Error Estimation and Targeted Refinement in 3-D FEM," Proceedings of the 2021 USNC-URSI National Radio Science Meeting, January 4-9, 2021, Boulder, Colorado, Online Conference.
6. S. Kasdorf, B. Troksa, J. J. Harmon, C. Key, and B. M. Notaroš, "Shooting-Bouncing-Rays Technique to Model Mine Tunnels: Theory and Accuracy Validation," invited paper, Special Session "Advances in Frequency-Domain CEM Techniques and Applications," Proceedings of the 2020 International Applied Computational Electromagnetics Society (ACES) Symposium – ACES2020, July 27–31, 2020, Online Conference.
7. S. Kasdorf, B. Troksa, J. J. Harmon, C. Key, and B. M. Notaroš, "Shooting-Bouncing-Rays Technique to Model Mine Tunnels: Algorithm Acceleration," invited paper, Special Session "High Performance Computing in Electromagnetics," Proceedings of the 2020 International Applied Computational Electromagnetics Society (ACES) Symposium – ACES2020, July 27–31, 2020, Online Conference.

8. B. M. Notaroš, J. J. Harmon, and C. Key, “Generalized Automatic Surface Reconstruction for CEM Simulations,” invited paper, Special Session “Numerical Methods in Electromagnetics,” Proceedings of the 21st International Conference on Electromagnetics in Advanced Applications – ICEAA 2019, September 9- 13, 2019, Granada, Spain, pp. 1334–1335.
9. B. M. Notaroš, S. B. Manic, C. Key, J. J. Harmon, and D. Estep, “Overview of Some Advances in Higher Order Frequency-Domain CEM Techniques,” invited paper, Special Session “Advances in Frequency-Domain CEM Techniques and Applications,” Proceedings of the 21st International Conference on Electromagnetics in Advanced Applications – ICEAA 2019, September 9-13, 2019, Granada, Spain, pp. 1330–1333.
10. B. M. Notaroš, J. J. Harmon, C. Key, D. Estep, and T. Butler, “Error Estimation and Uncertainty Quantification Based on Adjoint Methods in Computational Electromagnetics,” invited paper, Special Session “Applications of Machine/Deep Learning and Uncertainty Quantification Techniques in Computational Electromagnetics,” Proceedings of the 2019 IEEE International Symposium on Antennas and Propagation, July 7–12, 2019, Atlanta, GA, USA, pp. 221–222.
11. J. J. Harmon, C. Key, S. B. Manic, and B. M. Notaros, “Construction and Application of Geometrically Optimal Curvilinear Surface Elements for Double Higher-Order MoM-SIE Modeling,” Proceedings of the 2019 USNCURSI National Radio Science Meeting (Joint with IEEE AP-S Symposium), July 7–12, 2019, Atlanta, GA, USA.
12. J. J. Harmon and B. M. Notaroš, “The Dual Weighted Residual and Error Estimation in Double Higher-Order FEM,” Proceedings of the 2019 IEEE International Symposium on Antennas and Propagation, July 7–12, 2019, Atlanta, GA, USA, pp. 771–772.
13. J. J. Harmon, C. Key, B. M. Notaros, D. Estep, and T. Butler, “Adjoint-Based Uncertainty Quantification in Frequency-Domain Double Higher-Order FEM,” Proceedings of the 2019 International Applied Computational Electromagnetics Society (ACES) Symposium – ACES2019, April 15–19, 2019, Miami, Florida, USA.

14. J. J. Harmon, C. Key, and B. M. Notaroš, “Geometrically Conformal Quadrilateral Surface-Reconstruction for MoM-SIE Simulations,” invited paper, Special Session “Advances in Curved Patch Modeling,” Proceedings of the 2019 International Applied Computational Electromagnetics Society (ACES) Symposium – ACES2019, April 15–19, 2019, Miami, Florida, USA.
15. J. J. Harmon, C. Key, B. Troksa, T. Butler, D. Estep, and B. M. Notaroš, “Adjoint-based A Posteriori Error Estimation and its Applications in CEM: DHO FEM Techniques and 3D Scattering Problems,” Proceedings of the 2019 USNC-URSI National Radio Science Meeting, January 9-12, 2019, Boulder, Colorado.